Analytical and Experimental Study of Axisymmetric Truncated Plug Nozzle Flow Fields

Thomas J. Mueller, Wayne P. Sule,
Arthur E. Fanning, Thomas V. Giel and
Fred L. Galanga

Final Report UNDAS TN-601-FR-10
September, 1972

Prepared under Contract No. NAS 8-25601 by
UNIVERSITY OF NOTRE DAME
NOTRE DAME, INDIANA

for
NATIONAL AERONAUTICS AND SPACE ADMINISTRATION

UNIVERSITY OF NOTRE DAME, NOTRE DAME, INDIANA 46556

Department of Aerospace and Mechanical Engineering

ANALYTICAL AND EXPERIMENTAL STUDY OF AXISYMMETRIC TRUNCATED PLUG NOZZLE FLOW FIELDS

Thomas J. Mueller, Wayne P. Sule,
Arthur E. Fanning, Thomas V. Giel and
Fred L. Galanga

Final Report UNDAS TN-601-FR-10

September, 1972

Prepared under Contract No. NAS 8-25601 by

UNIVERSITY OF NOTRE DAME
NOTRE DAME, INDIANA

for

NATIONAL AERONAUTICS AND SPACE ADMINISTRATION

FOREWARD

The work reported herein was performed by the Department of Aerospace and Mechanical Engineering, University of Notre Dame, for the George C. Marshall Space Flight Center, National Aeronautics and Space Administration, Marshall Space Flight Center, Alabama, 35812, under Contract NAS 8-25601. The technical direction was provided by Klaus W. Gross of the Propulsion and Vehicle Engineering Laboratory. Additional support necessary to bring this work to a meaningful conclusion was supplied by the University of Notre Dame. This research was performed between February, 1970, and August 31, 1972.

The authors would like to acknowledge the efforts of R. J. Matz, R. C. Bauer, S. Wehofer and C. E. Peters of ARO, Inc., Tullahoma, Tenn., for their helpful comments throughout this investigation.

ABSTRACT

Results of an experimental and analytical investigation of the flow field and base pressure of internal-external-expansion truncated plug nozzles are presented. Experimental results for two axisymmetric, conical plug-cylindrical shroud, truncated plug nozzles are presented for both "open" and "closed" wake operations. These results include extensive optical and pressure data covering nozzle flow field and base pressure characteristics, diffuser effects, lip shock strength, Mach disc behaviour, and the recompression and reverse flow regions. Transonic experiments for a special planar transonic section are also presented. An extension of the analytical method of Hall and Mueller to include the internal shock wave from the shroud exit is presented for "closed wake" operation. Results of this analysis include effects on the flow field and base pressure of ambient pressure ratio, nozzle geometry, and the ratio of specific heats. Static thrust is presented as a function of ambient pressure ratio and nozzle geometry. A new transonic solution method is also presented.

A comparison of analytical and experimental results showed that the calculated base pressure results were greatly improved by the inclusion of the internal shock wave in the overall solution. The results of the transonic calculations indicated that for nozzles with circular arc throat regions, the sonic line was a flat parabola.

TABLE OF CONTENTS

LIST OF SYMBOLS

A	Area
a	Term in Van der Waal's Equation (Appendix I)
B	Expression defined by Equation 2
b	Term in Van der Waal's Equation (Appendix I)
C	Crocco number; variable defined by Equation (I34)
c	Velocity of sound
C_f	Thrust Coefficient defined as (Thrust-Drag)/Ideal Thrust
C_T	Thrust Coefficient defined as Thrust/$(P_{01}A_{nt})$
D	Diameter
F	Variable defined by Equations (I37a) and (I37b); Force
f	An arbitrary function
h	Plank's constant
I_1, I_2, J_1, J_2	Integrals defined by Equations 3-6
i	$\sqrt{-1}$
k	Boltzmann's constant
K	Variables defined by Equations (I35) and (27)
L	Plug or Shroud length from throat; diffuser length
M	Mach number
$\tilde{M}$	Momentum
$\dot{m}$	Mass flow rate
P	Pressure
R	Radius
$\mathscr{R}$	Gas Constant
R'	Compressible divergence factor
R_e	Reynolds number

r	Radius
$\tilde{s}$	Entropy
T	Temperature; Thrust
u	Velocity in x or $\dot{X}$ direction
V	Velocity
v	Specific volume
W	Complex number
X,Y	Co-ordinates of the reference (inviscid) co-ordinate system
$\dot{X}$	Axial co-ordinate with origin at plug base
$\ddot{X}$	Axial co-ordinate with origin at nozzle throat
$\tilde{X}$	Axial co-ordinate with origin at shroud exit
x,y,z	Co-ordinates of the intrinsic (viscous) co-ordinate system; co-ordinates of Planar transonic nozzle PLTR1
Z	Complex number
α	Plug angle
β	Base temperature ratio ($=T_{01}/T_b$); shock wave angle.
γ	Ratio of specific heats
Δ	Increment
ϵ	Lip shock strength
η,ξ	Bipolar co-ordinates; distances along left-running and right-running characteristics, respectively
η	Dimensionless co-ordinate ($=\sigma y/x$)
θ	Streamline angle, characteristic temperature of molecular vibration
μ	Mach angle
ν	Prandtl-Meyer turn angle; characteristic frequency of molecular vibration
ρ	Density

σ	Jet spread parameter
Φ	Velocity potential
ϕ	Velocity ratio ($=u/u_a$)

Subscripts

1,2,3,4	Stations for the basic flow model
a	Conditions in the external stream adjacent to the mixing region; refers to ambient conditions
at	Atmospheric conditions
b	Conditions at the base of the plug
BL	Boundary layer
cell	Diffuser Cell Region
$\mathfrak{C}$	Centerline
cp	Constant pressure boundary
d	Streamline whose kinetic energy is just sufficient to enter the recompression region, diffuser
ex	Exit conditions
inc	Incompressible value
j	Condition along the jet boundary separating streamline
m	Coordinate shift in the mixing theory due to the momentum integral
md	Mach disc
max	Refers to a maximum value
ne	Nozzle exit
nt	Nozzle throat
o	Stagnation conditions
01	Nozzle stagnation conditions
R	Condition along the R-streamline

r	Conditions at recompression
sh	Shroud
st	Second throat
spc	Sideplate centerline
w	Wake
wl	Wall

Superscripts

—	Average value
T	Transformed

LIST OF FIGURES

INTRODUCTION

GENERAL REMARKS

Rocket and air-breathing propulsion systems for future space and atmospheric operations will require exhaust nozzles that perform efficiently over a wide range of ambient conditions. Improved nozzle efficiency can substantially reduce operating costs and increase the overall vehicle payload. At present, the converging-diverging (C-D) nozzle is used almost exclusively in rocket and jet propulsion systems. There are two major reasons for the predominance of C-D nozzles in current propulsion applications. The first is the early date at which the nozzle was introduced (1884). As a result, many years have been spent on subsequent refinement and development, which has transformed the original idea into a reliable workhorse of the propulsion industry. The second reason for C-D nozzle prevalence is that the flow field within the nozzle is relatively uncomplicated, and therefore lends itself to the necessary optimization calculations for overall mission trajectories. Also, C-D nozzles achieve a very high efficiency at their design point (the point at which the nozzle exit pressure is equal to the ambient pressure).

Despite the positive features of C-D nozzles, this configuration has some serious disadvantages. Often the size and weight of the nozzle limits the payload of the vehicle. As stated earlier, these nozzles operate at peak efficiency only when the nozzle exit pressure is equal to the ambient pressure. In this respect, it would be desirable to have relatively low area ratios at sea level conditions to avoid large overexpansion penalties, while high area ratio nozzles are attractive for reducing underexpansion losses at high altitude. For example, with cold air at a chamber pressure of 600 pounds per square inch absolute, a C-D nozzle of area ratio 25 would attain only about 80% of ideal thrust at sea level, while a C-D nozzle of area ratio 8 under the same conditions will produce about 95% of ideal thrust (Ref. 1). However, since the nozzle area ratio is fixed (variable area C-D nozzles usually require heavy mechanical actuators) C-D nozzles are commonly designed with area ratios that are optimized to give the highest time-averaged specific impulse. Also, the nozzles generally have low area ratios to prevent separation at low altitudes, and are therefore underexpanded at high altitudes.

Recent analyses and tests (Refs. 1, 2, and 3) have demonstrated that a group of nozzles referred to as altitude compensating nozzles are partially able to overcome the off-design performance losses inherent in C-D nozzles. The truncated plug (T-P) and aerospike nozzles are representative members of this group which have the additional advantage of reduced size and weight. The presence of a viscous separated wake and free expansion surfaces within the nozzle flow field, as shown in Fig. 1, enables this type of nozzle to adjust to ambient conditions, and thereby reduces overexpansion losses at low altitudes and minimizes underexpansion losses at high altitudes.

DESCRIPTION OF PROBLEM

At low values of chamber to ambient pressure ratio (Fig. 1a), the separated flow region is "open" (i.e., sensitive to ambient conditions), and unsteady in nature. Due to the relatively high ambient pressure, the external boundary is inclined toward the nozzle axis. The combined effects of the "open wake" and the position of the external boundary result in a low overall nozzle area ratio during low altitude operation. As the chamber to ambient pressure ratio increases, the jet mixing region (shear layer between nozzle exhaust flow and separated flow region) moves toward the nozzle axis and the external boundary moves away from the nozzle axis. This produces a continuously increasing effective nozzle area ratio as the vehicle altitude increases. During the "open wake" regime of operation, the base pressure is essentially equal to the ambient pressure.

At some point in the trajectory, when the chamber to ambient pressure ratio has increased sufficiently, the wake "closes" (Fig. 1b) and the separated base region is no longer sensitive to ambient conditions. However, recent data (Ref. 4) indicate that the near wake can still be influenced by disturbances originating downstream of the critical point on the wake axis. The structure of the nozzle flow field (including the base pressure) for "closed wake" operation is of particular interest, since this represents design operating conditions. Also, for most nozzles of practical interest, the wake would be "closed" for the major portion of the mission. Nozzle area ratio adjustment still occurs during "closed wake" operation, since the external boundary continues to move away from the nozzle axis as the ambient pressure decreases. This continual adjustment of area ratio with altitude is the reason for the designation, altitude compensating nozzle. The aerodynamic compensation provides the mechanism by which these nozzles can maintain near optimum efficiency over a wide range of operating conditions.

The plug nozzle configuration shown in Fig. 1 possesses one serious drawback which, fortunately, can be remedied. Although the nozzle demonstrates excellent performance in quiescent air, it has serious performance losses at low values of chamber to ambient pressure ratio when an external stream is present (Refs. 5, 6, 7, and 8). The external flow effects can be explained with the aid of Fig. 1. In this configuration, the internal flow passage is designated such that the minimum area is at the shroud exit, and the entire expansion takes place externally. Turning the flow parallel to the plug at the exit (necessary for an isentropic expansion) requires a boattailed nozzle shroud. The boattail angle increases with nozzle design Mach number. The presence of the boattail has no effect on quiescent operation, since the flow expands to the ambient pressure regardless of the shroud geometry. With an external stream, however, the boattail plays a major role in the overall nozzle performance. In general, the external flow will separate from the boattail, establishing a low pressure region which results in large boattail drag. In addition, the pressure in this separated region is below ambient, which causes the external boundary to overexpand, destroying

the altitude compensating characteristic of the nozzle. The combined effect of the boattail drag and the overexpansion on the thrust minus drag is shown graphically in Fig. 2. This severe performance deficit would be unacceptable for most T-P nozzle applications. The problem is solved with the use of a straight cylindrical shroud, which minimizes the boattail as shown in Fig. 3. With the geometry shown in Fig. 3, the flow initially expands internally, and then continues to expand externally when the shroud exit is reached. The nozzle is therefore designated the internal-external-expansion truncated plug nozzle. It has been shown through experimental investigations (Refs. 1, 6, and 7) that this configuration retains the altitude compensation characteristics of the all-external-expansion nozzles, while greatly improving performance at low altitudes.

In Fig. 4, the thrust coefficient for a typical internal-external-expansion T-P nozzle is compared with both a high and low area ratio C-D nozzle. These data are for a typical boost trajectory (Ref. 1), with burnout at 167,200 feet. The results clearly demonstrate the altitude compensation capability of T-P nozzles and their superiority over fixed geometry C-D nozzles. The T-P nozzle satisfies the major requirement for advanced propulsion systems with the thrust coefficient being near optimum for the entire range of operating conditions, as shown in Fig. 4. This type of nozzle also provides the advantage of reduced length, since it is possible to truncate the plug to less than 20% of the full length without serious performance losses (Refs. 9, 2, and 3).

In addition to the T-P nozzle advantages outlined above, this nozzle concept also has a wide range of applicability. It has demonstrated improved performance over conventional nozzles for both scramjet engines and supersonic aircraft engines (Refs. 1, 3, 5, 10, and 11), as well as for booster applications. Another advantage of plug type nozzles is that they are easily adapted to two-dimensional and non-axisymmetric configurations, which have been proposed for some future rocket and air-breathing propulsion systems (Refs. 12 and 13).

SCOPE OF PRESENT WORK

The principal objectives of this research were: 1. Describe the flow field, including lip shock strength and Mach disc formation, and base pressure characteristics of conical plug - cylindrical shroud truncated-plug nozzles (shown in Fig. 3) as affected by changes in ambient pressure ratio, plug length, and area ratio. 2. Develop analytical methods of determining the sonic line for plug nozzles. 3. Extend an existing method for calculating the flow field and base pressure to include the internal shock wave generated near the shroud exit for "closed wake" operation. 4. Compare the analytical results with the experimental data.

EXPERIMENTAL PHASE

To provide guidance for the formulation of the analytical flow model, a series of experiments were performed on various plug nozzles in the Nozzle Thrust Facility. These experiments also produced the experimental data used to verify the theoretical results. A description of the facility and an outline of the experimental procedure are presented below.

DESCRIPTION OF AXISYMMETRIC NOZZLE THRUST FACILITY

The University of Notre Dame Nozzle Thrust Facility (NTF) was designed to test conventional and unconventional nozzles with up to one square inch throat area and up to 100 lb_f (444.82 Newtons) thrust. It is a blowdown type apparatus exhausting to the atmosphere. The nozzle total pressure can be varied from 20 psi (137.89 kN/m^2) to 150 psi (1034.20 kN/m^2), allowing the testing of nozzles over a wide range of pressure ratios. The basic components of the system, shown in Fig. 5 and described in detail below, include: air compressor, storage tanks, pressure regulators, orifice flow meter, thrust stand assembly, and instrumentation.

The air compressor, manufactured by the Gardner-Denver Company, is a 10 HP (10.138 metric HP) unit which is capable of delivering 22 SCFM (0.623 SCmM) at 250 psig (1723.67 kN/m^2 gage). The air passes through an aftercooler and moisture separator. The compressor unit is also equipped with an oil vapor filter charged with activated alumina, and an air dryer charged with a silica gel desicant. The dryer which supplies air at a dew point between -20^oF (-28.888^oC) and -40^oF (-39.999^oC) requires approximately three hours of regeneration for each eight hours of operation. Regeneration is accomplished by heating the desicant to between 250^oF (121.111^oC) and 400^oF (204.444^oC) thereby driving the moisture from the silica gel. During regeneration a small amount of air is blown from the storage tanks through the dryer to purge the moisture from the unit.

The two 50 cu. ft. (1.415 m^3) storage tanks are ASME coded pressure vessels designed for 265 psia (1827.09 kN/m^2) at 450^oF (232.222^oC) maximum, and were hydrostatically tested as per ASME code, Section VIII. Into one end of each tank a 6-in. (15.240 cm) diameter schedule 40 pipe was inserted containing a 200 lb_m (90.718 kgm) thermal mass for temperature stabilization. The other end of each tank contains a 12 in. (30.480 cm) by 16 in. (40.640 cm.) standard ASME code manhole for required inspection. Included with each tank is a 265 psia (1827.09 kN/m^2) safety valve. The two tanks are manifolded together in parallel. The flow passes from the storage tanks through a gate valve to three two-inch pilot operated regulators, mounted in parallel which are used to regulate the nozzle total pressure during each run. Downstream of the regulators is an orifice flow meter permitting mass flow measurement.

The thrust stand arrangement for the Nozzle Thrust Facility is also shown in Fig. 5. This assembly rests on a steel plate which is welded

to one storage tank. It consists of a stilling chamber which has internal dimensions of 3 in. (7.620 cm) in diameter by approximately 15 in. (38.100 cm) in length. This stilling chamber is constructed from a solid block of aluminum. It includes one perforated plate and four number 30 mesh screens to straighten the flow before entering the nozzle test section, which is attached to the end of the chamber. Air enters the stilling chamber from both sides through rigidly mounted pipe, separated from the stilling chamber by flexible bellows. The bellows allow the stilling chamber to move axially for thrust measurement. Besides the bellows, the chamber is attached to the mounting plate by four aluminum bars utilizing eight flexture hinges. A load cell, rated at 100 lb_f (444.82 Newtons) nominal, is mounted rigidly to the thrust stand and connected to the stilling chamber by means of an aluminum relaxation flexture to minimize transmission of transverse loads. The load cell has been dead weight calibrated. The results show that hysteresis does not exceed ± 0.5%.

Instrumentation

The NTF is equipped with a complete set of instrumentation, including storage tank pressure, regulator preset pressure, and stilling chamber total pressure and temperature. The stilling chamber total pressure and temperature are measured downstream of the screens just before the nozzle entrance. Total temperature is measured with an iron constantan thermocouple. The pressure differential across the orifice flow meter is recorded with a Meriam well-type mercury manometer.

Twenty 60 in. (152.40 cm) Meriam reservoir-type mercury manometers were used to measure nozzle contour static pressure and nozzle total pressure profiles. Provisions can also be made to include pressure transducers into the various nozzle diffuser configurations. The facility has also been designed to include a schlieren and shadowgraph system for visual study of the external nozzle flow.

To measure the static pressure variation along the geometric center of the T-P nozzles a special sliding tube probe was constructed. This probe consisted of a slotted hypotube attached to the plug base and extending downstream 22 in. (55.88 cm). This hypotube is rigidly supported at the downstream end by an angle-iron frame. A second movable hypotube with a static pressure orifice was contained within the first. The static pressure orifice could therefore be translated along the geometric center of the nozzle by sliding the inner hypotube.

Axisymmetric Truncated Plug Nozzles

Two axisymmetric internal-external-expansion plug nozzles were designed for use with the NTF. These nozzles were designed for Mach numbers of 1.90 (ATP1) and 2.00 (ATP2) based on the overall area ratio, A_{ne}/A_{nt}. The plugs were conical in shape and converged toward the axis at an angle of 10^{o}. The geometry of the nozzles is shown in Figs. 6 and 7, and the plug lengths, etc., are included in Tables I and II.

All the plugs were instrumented with static pressure taps in the base. Other static pressure taps were located on the plug surface just upstream of the base corner and also at the shroud exit plane for all ATP2 plugs. Additional static pressure taps were located between the geometric throat and the shroud exit corner along the ATP1 shroud surface. The plugs were mounted to a webbed centerbody, which was contained in a buffer section. Tubing from the pressure taps in the plugs exited from the NTF through this buffer section. The shroud contours were cylindrical and extended a distance of 0.300 inches (0.762 cm), from the throat. The throat areas were 0.330 in^2 (2.129 cm^2) and 0.602 in^2 (3.884 cm^2) respectively. The minimum running time for the larger throat area at the maximum stagnation pressure was approximately thirty seconds without any loss in stagnation pressure.

Planar Transonic Nozzle Section

A plane two-dimensional converging-diverging nozzle, PLTR1, was constructed for the transonic experiments, as shown in Fig. 8. Circular arcs with radii of curvature of 5.05 inches (12.827 cm) were chosen for the wall contours. The wall contours and sideplates for the symmetric channel were machined in Reynold's Aluminum T33 tooling plate. The blocks containing the wall contours were mounted between the sideplates to fix the centers of curvature of the wall contours at 5.15 inches (13.081 cm) above and below the plane of symmetry, resulting in a gap at the geometric throat of 0.200 inches (0.508 cm). The internal distance between sideplates, or nozzle depth, was constant at 1.985 inches (5.042 cm). The throat area was 0.397 sq. inches (2.561 cm^2). The exit was located 1 inch (2.540 cm) downstream from the geometric throat, and the gap between wall contours at the exit was 0.400 inches (1.016 cm). The area ratio at the exit was calculated to be 2.00 with a corresponding one-dimensional design Mach number of 2.197. The wall contours were continued upstream of the throat a distance sufficient to produce the gap between contours of 1.15 inches (2.921 cm), necessary to connect with the two-dimensional transition piece of the NTF.

The nozzle was fitted with pressure taps along both the lower contour and one of the sideplates. The locations of the pressure taps on the lower contour, Group C, are given in Table III. The x-location is the distance from the geometric throat and the z-location is the distance from a plane equidistant from and parallel to each sideplate. The taps were staggered in the z-direction so as to minimize upstream disturbance. There were three groups of pressure taps on the sideplate. Group S, was located on the nozzle's plane of symmetry. Group T was located at the geometric throat and Group B was located at an inflow station on a circular arc, centered at the geometric throat, and having radius of 1 in. (2.540 cm). The locations of the pressure taps in each of these groups are given in Table IV. All x-locations are distance from the geometric throat, along the plane of symmetry and all y-locations are vertical displacements above or below this plane.

Axisymmetric Diffuser

A long second throat diffuser was designed and fabricated to mate with the axisymmetric T-P nozzle with A_{ne}/A_{nt} = 1.555 and L/L_{max} = 0.3785. The nozzle-diffuser combination including all pertinent dimensions is shown in Fig. 9. Since the state-of-the-art method for designing a diffuser for plug nozzles is still basically a trial and error method, the report of Taylor and Toline (Ref. 14) was used to help determine approximate dimensions and area ratios in order to construct a working diffuser model. The diffuser shown in Fig. 9 has a second throat area ratio, A_{st}/A_{ne} = 1.523, a duct area ratio, A_d/A_{ne} = 4.932, and a length of duct to duct diameter ratio of L_d/D_d = 0.694. This diffuser was fitted with 12 static pressure taps along its contour, the third tap was arbitrarily chosen as the cell pressure.

Experimental Procedure and Accuracy

Standard operating procedure for the NTF consisted of first presetting the desired nozzle total pressure with the regulator and then starting the nozzle flow. After allowing several seconds for the pressures in the system to stabilize, the data were recorded. The nozzle total pressure and temperature were read from standard gauges mounted on the NTF control panel. The static pressures were obtained from 60 in. (152.400 cm) well-type mercury manometers. After the pressure data were read, shadowgraph pictures of the nozzle flow field were taken. This was accomplished by turning off all room lights and exposing a sheet of Kodak Royal Pan film with a single flash from a strob light mounted behind a pinhole. The pressure data were reduced using standard techniques. Experimental data for the location of the shock waves and the constant pressure boundary were obtained from the shadowgraph photographs.

Basically, the experimental data consisted of static pressure and total pressure measurements and the determination of the shock wave and constant pressure boundary locations from shadowgraphs of the flow field. The mercury manometers used to record the base pressure and other static pressures had scale markings at intervals of 0.10 in. (0.254 cm). Therefore, the pressure could be read to within 0.025 in. (0.0635 cm). Since the smallest reading taken in the primary region of interest (i.e., the base region) was on the order of 3 in. (7.620 cm) of mercury, the maximum error was about 2%. The error involved in reading the total pressure was approximately 0.50%, and therefore the total maximum error in the base pressure ratio was less than 4.0%.

The internal shock wave, Mach disc, and constant pressure boundary locations were measured from shadowgraphs using a Wayne-George X-Y Coordinate Converter. This instrument is capable of measuring distances to within 0.0005 in. (0.00127 cm). With most measurements being on the order of 1 in. (2.54 cm) to 2 in. (5.08 cm), this accuracy would imply a very small percent error. However, neither the shock waves nor the constant pressure boundary appeared in the photographs as sharp, distinct lines. The constant pressure boundary showed up as a wider

band than the shock wave. Because of the uncertainty of locating the exact position of these surfaces within the bands on the pictures, the error in the constant pressure boundary location is around 5%, and the error in the shock wave location is on the order of 2.5%. The error in the Mach disc measurements is between 3% and 5%, being greater as the Mach disc moves upstream.

DISCUSSION OF EXPERIMENTAL RESULTS

The experimental results include a description of the base pressure and flow field characteristics of conical-plug cylindrical-shroud, truncated plug nozzles. A discussion of these characteristics as affected by changes in ambient pressure ratio, plug length, and area ratio is presented below.

Base Pressure Characteristics

The base pressure characteristics for the six nozzle configurations of ATP1 are shown in Fig. 10. These data indicate that during a large portion of the "open wake" operation, the base pressure is essentially equal to the ambient pressure for all the plug length ratios used. At a particular value of the overall pressure ratio (depending upon nozzle geometry) the wake "closes". Once "closed wake" operation has been reached, the base pressure remains constant with further decreases in P_{at}/P_{01}.

For the two longer plug lengths (L/L_{max} = 0.4290 and 0.4802) there is a deviation from the normal "open wake" operation. This appears as an apparent discontinuity in the base pressure ratio between the values of 0.20 and 0.40 in the overall pressure ratio. As P_{at}/P_{01} decreases toward the "jump", the base pressure decreases below ambient, as shown by the steepening slope of the data in this region. After the "jump", the same trend continues until the wake "closes". A possible explanation for this behavior was obtained from a series of shadowgraphs showing the development of the flow field (Ref. 15). At values of P_{at}/P_{01} above the "jump", the internal shock wave reflects from the plug surface and intersects the constant pressure boundary. The shock is then reflected as an expansion which, for these longer plug lengths, impinges on the plug surface upstream of the base. Apparently, this expansion accelerates the flow, which results in a reduced base pressure. Once the expansion has moved downstream of the plug base, the Mach number approaching the base would be lower, resulting in a higher base pressure. The base pressure after the "jump" is actually greater than ambient, since the shock wave intersecting the plug reduces the Mach number below the value it would have had in the absence of the shock.

Verification for this explanation is provided by noting the value of overall pressure ratio at which the "jump" in the data occurs. If the discontinuity in base pressure is caused by the reflected expansion moving off the plug, the phenomenon would be expected to occur at a lower value of P_{at}/P_{01} as the plug length is increased. This is because the

point of impingement of the expansion moves down the plug as the overall pressure ratio is decreased. For a longer plug, the expansion would reach the plug corner at a lower value of P_{at}/P_{01} than for a shorter plug. This trend is indeed observed in the base pressure data for the two longer plugs.

Fig. 11 shows the base pressure characteristics for the four nozzle configurations of ATP2. These base pressure characteristics are similar to those of ATP1 shown in Fig. 10. When the "open wake" base pressure is not equal to the ambient pressure it is lower than the ambient pressure. This occurs in the vicinity of wake closure and results from the intersection of an expansion with the free shear layer.

The variation of the "closed wake" base pressure with plug length ratio for both ATP1 and ATP2 is presented in Fig. 12. The base pressure ratio decreases with increasing plug length ratio for both nozzles. For the same plug length ratio, however, the base pressure for ATP2 is as much as 50% lower than the value for ATP1, (i.e., the "closed wake" base pressure ratio decreases with increasing area ratio).

Another very important trend to be found in the base pressure characteristics data is the variation in overall pressure ratio at which the wake "closes" as a function of plug length. This effect is plotted explicitly in Fig. 13. The value of P_{at}/P_{01} at wake "closure" decreases with increasing plug length and area ratio. This means that, in general, "closed wake" operation would be reached at lower altitudes for shorter plugs or lower area ratio nozzles. This result points to one of the reasons for using shorter plugs. The calculation of performance for a given mission is greatly facilitated if the base pressure is constant ("closed wake" condition) for the longest period possible. In addition, "open wake" operation could possibly lead to flow oscillations which might produce prohibitive vibrations. Fig. 13 indicates that shorter plug lengths increase the percentage of time at the "closed wake" condition.

Diffuser Effects

No diffuser starting problems were encountered over the range of upstream stagnation pressure available in the Notre Dame Nozzle Thrust Facility (NTF). The static pressure ratio along the diffuser wall is shown for four values of upstream stagnation pressure in Fig. 14. For the first five pressure taps from the left, the static pressure is nearly constant. This is usually called the cell region and the cell pressure was arbitrarily chosen as that indicated by the third tap (see Fig. 9). These pressure distributions are only slightly different for different values of P_{01}. It appears that the "constant pressure" boundary impinges on the inclined ramp leading to the second throat. In order to determine this impingement point more accurately, an oil and lampblack paste was smeared on the diffuser walls and the nozzle-diffuser was run. The impingement location obtained is shown in Fig. 14. For all of the total pressures shown here, the T-P nozzle wake was "closed". The base pressure ratio P_b/P_{01} was constant and equal to 0.102.

This base pressure was identical to those obtained for this nozzle without the diffuser present. Therefore, for "closed wake" operation this diffuser had no effect on nozzle performance.

External Flow Field Characteristics

The external flow fields for the nozzles ATP1 and ATP2 were investigated in detail. For each of the nozzle configurations, shadowgraphs of the flow fields were obtained for at least ten different overall pressure ratios. The values of P_{at}/P_{01} were selected so that the nozzles would be operating in the "closed wake" regime.

The shadowgraphs of the nozzle flow fields for ATP1 are presented in Figs. 15 through 20. (For the nozzle with a plug length ratio of 0.2184, the plug ends at the shroud exit as seen in Fig. 15 and represents a zero-length plug for the shroud geometry considered here.) Certain basic flow characteristics are common to all nozzle configurations. These include the external boundary emanating from the shroud exit, the expansion from the shroud exit, the strong internal shock originating in the vicinity of the shroud exit, the lip shock originating in the vicinity of the plug corner, and the recompression shock wave.

The movement of the internal shock with changes in the overall pressure ratio is also very distinct in the photographs. In the shadowgraph sequence for each plug length, the angle of the internal shock wave from the horizontal increases noticeably as the value of P_{at}/P_{01} is increased. This happens as the shock penetrates into the expansion fans from both the plug corner and the shroud exit, i.e., into lower Mach number regions. Also, as P_{at}/P_{01} increases, the external boundary moves toward the axis.

Lip Shock

The lip shock is of interest because of its possible effect on the base pressure and the near wake, both through interactions with the viscous shear layer as it separates, and through a pressure increase in the inviscid flow field. In all the shadowgraphs which have been made of the truncated plug nozzle flow fields, the lip shock is at most barely visible. It always curves away from the centerline penetrating deeper into the expansion regions, and often, in the photographs, it disappears. The lip shock has been extensively studied by Hama (Ref. 16). His results indicate that although the lip shock is usually strong, the lip shock strength is greatly reduced when the body surface upstream of the base is inclined toward the nozzle axis (as with plug nozzles). Flow along such an inclined surface will be expanding, consequently reducing the surface pressure before separation and thus reducing the amount of expansion which is possible around the plug corner. In the T-P nozzle the flow along the plug will expand even more as it intersects the expansion waves from the shroud exit corner. The amount of expansion possible is further reduced by an increase in the base pressure, known to occur behind such boattail bodies as the plug. Because the lip shock

strength depends on the amount of overexpansion, a reduction in the expansion (and thus the overexpansion) will reduce the lip shock strength. Care must be taken not to have too large a boattail angle because this would allow separation from the plug contour, negating all the advantages of a boattail plug and causing a strong separation shock there.

The lip shock is formed by interactions at the plug corner, or lip, similar to the interactions forming the internal shock. The inviscid flow fails to negotiate the plug corner, overexpanding to a pressure below the base pressure. The boundary layer overexpands along with the inviscid flow and the lip shock forms during separation to compress the flow back up to the base pressure. Fig. 21a illustrates these combined phenomenon. The greater the amount of expansion around the plug corner, the greater will be the resulting overexpansion producing a lip shock of greater strength ε (or static pressure ratio crossing the shock--$P_2'/P_2 = P_b/P_2$ in Fig. 21b.)

Although the lip shock and the internal shock are consequences of the same phenomena, their different locations dictate different influences on the flowfield and in particular the base pressure. The internal shock causes the base pressure to decrease by preventing compression waves from the constant pressure boundary from influencing the near wake. In contrast the lip shock occurs with separation of the viscous near wake shear layer distorting the velocity profile of the viscous mixing layer thus resulting in an unknown influence on the near wake. Furthermore the lip shock will cause an increase in the pressure in the inviscid flow along the near wake. This second influence, however, is expected to diminish in the downstream direction as the lip shock becomes weaker.

Hama's results (Ref. 16) show that if, in addition to boattailing, the boundary layer approaching separation is turbulent, the lip shock almost totally disappears. This condition also will occur with most feasible truncated plug nozzles. In order to predict lip shock strengths for the experimental test models, the plot of lip shock strength, ε, vs. Mach number times Reynolds number at the plug lip, was used from Hama's results (see Fig. 21b). For ATP1 and $L/L_{max} = 0.2766$, $M_1 = 1.60$ and $R_{e_1} = 2.283 \times 10^6$ so that $M_1 \times R_{e_1} = 3.653 \times 10^6$. Similarly for ATP2 and $L/L_{max} = 0.2766$, $M_1 = 1.58$ and $R_{e_1} = 2.536 \times 10^6$ so that $M_1 \times R_{e_1} = 4.009 \times 10^6$. These ATP1 and ATP2 nozzles investigated both gave static pressure ratios crossing the shock (i.e., the shock strength) of about 1.08 as shown in Fig. 21b. This value is just slightly above the no shock, $\varepsilon = 1.0$, case. Short plug lengths were used because longer plugs would have more of a boattailing effect and therefore weaker shocks. The Reynolds number was calculated using the total length of the plugs on the test models.

It should be mentioned that for very large area ratio truncated plug nozzles where the Mach numbers and Reynolds numbers near the base corner are large, the lip shock can be strong. Likewise for expansion-deflection nozzles where a very large expansion is necessary around the base corner, the lip shock would be strong.

Recompression and Reverse Flow

Some insight into the complex recompression and reverse flow region of the near wake can be obtained from a correlation of shadowgraphs and static pressure measurements along the axis of the flow field. Measurements of static pressure along the flow axis were made with the sliding tube probe. Before gathering data, it was necessary to verify that the presence of the sliding tube probe did not significantly disturb or influence the flow field. The ATP2 nozzle with $L/L_{max} = 0.2327$ plug was used. For this case the ratio of the outside diameter of the sliding tube probe to the base diameter was 0.125. Flow disturbances created by support structures and probes of this type have been documented by numerous investigators (e.g., Ref. 17 and 18). These results indicate that for the Mach numbers encountered in the present T-P nozzle experiments, a probe-to-base diameter ratio of 0.125 should not significantly disturb the flow. In order to verify this, the nozzle base pressure was measured without the sliding tube centerline probe present. Then the centerline probe was attached to the nozzle base and both the base pressures from the base tap and from the centerline probe were measured. The results of this experiment, shown in Fig. 22, indicate that the base pressure is not significantly affected by the presence of the sliding tube probe.

Correlations of the centerline static pressure ratio with shadowgraphs of the flow field are presented in Figs. 23 and 24 for the "closed" and "open wake" respectively. The shadowgraph photographs have been reduced to the scale of the pressure distributions so that direct comparisons can be made. The case shown in Fig. 23 resembles the design operating condition for this type of nozzle. This flow field may be conveniently divided with reference to the centerline static pressure, i.e., constant pressure, rising pressure, and a region of falling pressure downstream of the maximum.

The near wake ends just slightly ahead of the peak static pressure. Therefore half of the near wake has a constant pressure and half has a rising pressure. This extensive region of essentially constant pressure with only a slight increase near the base indicates that the reverse flow is of relatively low subsonic velocity. The rising pressure in the second half of the near wake results from the recompression or turning of the inviscid flow back to the axial direction. This turning is accomplished through the recompression shock wave. The flow through the near wake neck accelerates through the sonic velocity (i.e., critical point) just downstream of the peak static pressure and becomes increasingly supersonic as the pressure continues to fall. The subsequent pressure rise is due to the interaction of the recompression and internal shock waves near the axis.

For the "open wake" case shown in Fig. 24, there is no essentially constant pressure region as in the "closed wake" case. There is, however, a rising pressure region and a region of falling pressure downstream of the peak. Since the centerline static pressure ratio increases from

the minimum value at $\dot{X}/r_{sh} = 0.50$ as the base is approached, it appears that the reverse flow velocities are relatively high. The distinct rising pressure region indicates that a recompression of the inviscid flow takes place although the shadowgraph indicates that this phenomena is more complicated than in the "closed wake" case.

The shock wave pattern visible in Fig. 24 suggests a possible helical-type shock pattern in the annular inviscid flow region. It should be mentioned that since this shadowgraph is a plane view of a circular flow region, only the edges of the shock waves can be seen. Of course, edges of shocks on the backside or frontside of the region can also be seen. This may explain the shock waves which appear to invade the reverse flow region. The flow mechanism which maintains the base pressure at almost ambient pressure is not at all clear.

Mach Disc

Downstream of the neck of the near wake the internal shock interacts at the centerline in one of two different ways. The first is the regular reflection or weak shock and the second is the Mach disc or strong shock. Furthermore, the Mach disc has been observed to form from two different conditions, the primary (internal shock) formation and the secondary (secondary shock) formation. Fig. 25 illustrates these shock wave interactions.

The Mach disc is seen as a near-normal shock wave on the nozzle axis downstream of the wake neck. This phenomenon has been studied by Peters (Ref. 19) and others for conventional C-D nozzles. Depending on the degree to which the nozzle flow is underexpanded, the internal shock wave will either undergo a normal reflection at the centerline or reflect from the Mach disc. Examples of regular reflection at the centerline can be seen in Figs. 16b, 17b and 17c. The Mach disc forms by basically the same mechanism as that which leads to Mach reflection (or Riemann wave) of an oblique shock from a solid surface. When the flow passes through the incident portion of the internal shock, it is turned away from the nozzle centerline. In passing through the reflected part of the shock, the flow must be turned parallel to the centerline. If the turning angle of the reflected shock is above the critical angle for the upstream Mach number, regular reflection cannot occur. In this case, the reflection point moves off the centerline to a point where the turning angle through the shock is below the critical angle. A normal shock then forms between the reflection point and the nozzle centerline. Since the flow is axisymmetric, this normal shock takes the form of a disc. The flow passing through the Mach disc has a different history than the flow passing through the incident and reflected internal oblique shock. Therefore a slip line forms downstream of the reflection point. Across this line the static pressures are equal, but the Mach number is discontinuous. These slip lines appear in the shadowgraphs as white lines extending downstream from the edges of the Mach discs.

As the overall pressure ratio is increased and the internal shock inclines more steeply toward the axis, the Mach disc location moves upstream toward the critical point (point at which the flow becomes sonic) on the wake axis. Since the Mach number ahead of the Mach disc decreases as the critical point is approached, the Mach disc strength also decreases. This process can be seen in the sequence in Fig. 18. In Fig. 18c, the strength has decreased to the point where the Mach disc is barely visible.

The nozzle flow field characteristics are further complicated by the expansion at the plug base corner. For the shorter plug lengths ($L/L_{max} < 0.429$), this expansion intersects the expansion from the shroud exit. After intersecting the internal shock, it reflects from the constant pressure boundary as a compression wave. This compression wave, which is inclined toward the nozzle axis, may complicate the Mach disc formation (as in Figs. 15a and 15b) or actually lead to the formation of a second Mach disc, as in Fig. 18b. Such a formation is termed a secondary Mach disc. Apparently the reflection of the expansion waves will only form a Mach disc if the expansion waves from the plug can reflect upstream of recompression. This can only happen with the shorter plugs, and indeed has been observed in the flowfield of the zero length plugs alone.

The location of either the Mach disc or the regular reflection on the centerline and the size of the Mach disc depend on the nozzle operating characteristics. During moderate ambient to total pressure ratio (P_{at}/P_{01}), just after the near wake has "closed", a regular reflection occurs not far downstream of the wake neck. As this pressure ratio decreases, the regular reflection moves downstream. Eventually a regular reflection can no longer satisfy the downstream conditions and a Mach disc forms. The Mach disc continues moving downstream with decreasing P_{at}/P_{01} as shown in Fig. 26. At the same time the disc increases in diameter as shown in Fig. 27. Since in atmospheric flight the ambient pressure ratio decreases with increasing altitude, the Mach disc structure will become more prominent at higher altitudes.

The secondary Mach disc is not formed in the same manner as the primary Mach disc and therefore can be expected to react in a slightly different manner. The secondary Mach disc structure, however, has only one noticeable variation from the trends observed for primary Mach discs. Its diameter increases only slightly with decreasing ambient pressure ratio and a regular reflection has not been observed in this formation.

The data in Figs. 26 and 27 exhibits noticeable scatter with increasing pressure ratio. This is primarily a measurement problem. As the pressure ratio increases the Mach disc or regular reflection moves closer to the critical point of the near wake. Here the flow is transonic and is characterized by viscous mixing effects which cause density gradients. As a result, the shock waves are weak, and in the shadowgraphs are not as clearly defined in this region.

The Mach disc strength increases with decreasing P_{at}/P_{01}, because as this ratio decreases the disc moves further downstream of the critical point, into a higher Mach number flow. This Mach disc behaviour is not unique to plug nozzle flowfields (Ref. 19).

Transonic Data

All experimental data for nozzle PLTR1 were obtained with the nozzle operating on the NTF. The static pressure taps were connected to a 10 tube, 60 in. (152.40 cm) mercury manometer bank. Due to the magnitude of the pressures to be measured it was necessary to bias the manometer reservoir by pressurizing it. The pressure bias on the reservoir was in turn measured on another 60 in. (152.40 cm) manometer. During a data gathering experiment all manometer readings were recorded photographically for later data reduction. The accurary to which the manometers could be interpreted was ±0.025 in. (0.0635 cm) of mercury.

The experimental data gathered in this phase is presented in Fig. 28. The reduced data is given in terms of the ratio of static pressure to the stagnation pressure in the stilling chamber. Data for both the wall contour, Group C, and the plane of symmetry at the sideplate, Group S, are shown. The locations of the pressure taps in Group C are given in Table III and those of Group S in Table IV. Data gathered with four different stilling chamber stagnation pressures is shown to lie essentially on the same curve. As only ten pressures could be measured simultaneously, it was necessary to obtain these curves in sections. The sections are designated by dotted lines crossing the curves. The smoothness of the curves between sections demonstrates the consistency of the measuring technique. Both Group C and Group S show the expected trends. The discrepancy in the region of Taps S15, S16 and C11 was shown to be a result of faulty taps. The data scatter at Tap S23 is due to the presence of a shock between S22 and S23 at the lower stilling chamber pressures.

ANALYTICAL PHASE

In order to optimize design, predict performance, and design altitude test facilities (Ref. 14) for this type of nozzle, it is desirable to calculate the entire nozzle flow field. The method of solution presented is for "closed wake" operation. The essential features of the "closed wake" flow field are shown in Fig. 3. The flow becomes sonic near the minimum area and then expands supersonically in the internal expansion portion of the nozzle. The external expansion begins at the shroud exit where the flow initially overexpands slightly, leading to the formation of the internal shock wave which recompresses the flow at the external boundary back to ambient pressure. The strong internal shock wave emanating from the shroud exit must be included in the overall solution. This shock penetrates deeply into the flow field, and may interact with the near wake region. The presence of this shock will certainly have an effect on the location of the external boundary, and could have an effect on the plug base pressure.

When the flow, which has been accelerated along the plug surface, reaches the corner of the plug base, it expands around the corner, initiates the lip shock and separates. The result is a separated region in the middle of the nozzle flow field. The high velocity nozzle flow surrounding the separated base region attempts to "pump out" this region through a mixing or shear layer along the interface. This mixing layer thickens as it progresses downstream and encounters some form of recompression region, so that it eventually satisfies ambient conditions. The recompression region is the result of a system of compression waves generated in the inviscid supersonic flow, adjacent to the mixing region. These compression waves coalesce to form the recompression shock. This shock is necessary to turn the inviscid flow parallel to the axis, after it has been accelerated toward the nozzle axis by the expansion around the corner. The shear layer will decelerate until the static pressure in the layer is nearly equal to that behind the recompression zone. Based on the velocity profile in the shear layer just before recompression, it appears that a significant part of this layer has relatively low velocity or kinetic energy. Since the lower energy flow cannot negotiate recompression, it is recirculated into the base region.

The analytical treatment of the nozzle flow field must incorporate the important characteristics outlined above. The pressure acting on the plug base is very important, since it can contribute significantly to the total thrust or drag of the nozzle. The location of the internal shock in turn may have an influence on the plug base pressure. The location of the external boundary is important when testing nozzles in altitude test facilities, or if it impinges on adjacent parts of the vehicle surface.

The object of the present research was to modify and extend the analytical solution of Hall and Mueller (Ref. 21) to include the internal shock wave. The supersonic inviscid portion of the flow was calculated using the rotational method of characteristics in order to include

the entropy gradient behind the internal shock. The separated flow region was determined by an integral method, and coupled to the method of characteristics by an iterative technique. Solutions were obtained for a variety of T-P nozzle geometries and overall pressure ratios.

FLOW MODEL

The overall flow model and computational scheme will be presented first, to clarify the complete solution technique. The details of the calculations for the individual parts of the solution will be explained in later sections.

Fig. 3b shows the essential features of the flow field under consideration. The nozzle geometry is a typical internal-external-expansion truncated plug nozzle with nonisentropic contours. Once the flow has passed through the sonic line and begins to accelerate supersonically, the governing equation for the inviscid flow becomes hyperbolic and can be solved by the method of characteristics. This method has been shown to be very accurate for a variety of supersonic flows of the type under investigation (Refs. 21 and 22). Two ways of including real gas effects into the method of characteristics are described in Appendix I. The axisymmetric rotational method of characteristics is used in the present study, in order to include the entropy gradients downstream of the internal shock in the calculations. Entropy gradients from other sources are not allowed, and it is therefore not possible to use the characteristics in a boundary layer, even if only the supersonic portion is considered. The entire flow field between the nozzle surfaces and between the external boundary and separated base region is assumed to be inviscid and adiabatic. In addition, the boundary layers on the nozzle surfaces are assumed to be negligible. In order to establish the origin of the internal shock wave near the shroud exit, an overexpansion technique is used. With this method the flow is initially expanded to a pressure below the actual ambient pressure. After a short distance downstream the external boundary pressure is set equal to the ambient pressure and the calculations procede normally. For all cases studied the nozzle was assumed to be exhausting into still air at zero velocity.

The solution of the separated base region is obtained using an extension of the flow model developed by Zumwalt (Ref. 23), and later modified by Mueller (Refs. 24 and 25) and Hall and Mueller (Ref. 21). With this analysis, a conical wake assumption is employed whereby the pressure field impressed on the separated shear layer is determined by the method of characteristics over a conetail. This method establishes the general features of the entire base region, while calculating the base pressure.

The conetail surface provides the boundary for the method of characteristics in the base region. However, the solution of the base region (including the orientation of the conetail) requires inputs from the method of characteristics. Therefore, in addition to the iterative base pressure solution, the solution of the entire nozzle flow field becomes iterative.

INVISCID FLOW SOLUTION

A complete derivation of the general method of characteristics, as well as a derivation of the axisymmetric rotational method of characteristics, is presented in Appendix I of reference 15. In the following sections, the actual computational procedures which employ these equations will be explained.

Initial Conditions

Since the method of characteristics is not able to handle subsonic or sonic flows, the solution must be started at a point where the flow has become supersonic. An adequate theoretical approach for determining the location of the sonic line in annular nozzles was not available for inclusion in this analytical procedure. However, a transonic solution for annular nozzles where the flow is essentially planar in the throat region has been concurrently developed and will be described in a later section. In this section, the starting line for the method of characteristics was obtained by a method similar to that outlined in Ref. 21.

The sonic line was assumed to be a straight line located at the geometric throat of the nozzle. One-dimensional isentropic relations were then used to establish the area ratio at which the flow will have reached a Mach number of 1.05. Using this area ratio and the nozzle geometry, the starting line could be physically located within the nozzle. A series of starting points were equally spaced along this line, and all starting Mach numbers were set equal to 1.05. The flow angle (with respect to the nozzle centerline) at each point on the starting line is calculated by assuming a linear variation between the plug angle and the shroud angle. The other flow variables necessary for the characteristics calculation can be obtained from the Mach number and flow angle. With the starting conditions thus determined, the calculations proceeded downstream using the standard method of characteristics technique.

Standard Method of Characteristics

Because the method of characteristics represents the solution of a hyperbolic differential equation, downstream boundary conditions are not required, and the solution proceeds downstream using only the known upstream values and the upper and lower boundary conditions. Disturbances in the flow field are not able to propagate upstream and affect regions of the flow which have already been calculated.

The actual calculational procedure varies somewhat, depending on whether the new point to be calculated is an interior point or a boundary point. Fig. 29 illustrates the process for the three types of calculations. For an interior point (Fig. 29a) conditions are known at the upstream points 1 and 2. This includes the locations of the points and the values of all flow variables. The physical location of point 3 is established by the intersection of the right-running characteristic through point 1 and the left-running characteristic through point 2.

Using the known values of Prandtl-Meyer angle, ν, and flow angle, θ, at points 1 and 2, in conjunction with the following equations from Appendix I, reference 15,

$$\nu_3 = \frac{F_1 + F_2}{2} \tag{I36a}$$

and:

$$\theta_3 = \frac{F_1 - F_2}{2} \tag{I36b}$$

where:

$$F_1 = (\nu_1+\theta_1) + \bar{C}_{13}\Delta\xi_{13} - K_{13}\left(\frac{\tilde{s}_3}{\mathscr{R}} - \frac{\tilde{s}_1}{\mathscr{R}}\right) \tag{I37a}$$

and:

$$F_2 = (\nu_2-\theta_2) + \bar{C}_{23}\Delta\eta_{23} - \bar{K}_{23}\left(\frac{\tilde{s}_3}{\mathscr{R}} \quad \frac{\tilde{s}_1}{\mathscr{R}}\right) \tag{I37b}$$

where:

$$C = \sin\mu \frac{\sin\theta}{r} \tag{I34}$$

and

$$K = \frac{\sin\mu \cos\mu}{\gamma} \tag{I35}$$

the values of ν and θ at point 3 can be calculated. In the axisymmetric case, the characteristics are curved, and point 3 (location and flow variables) must be established with an iteration scheme. An initial location of point 3 is obtained by extending straight line characteristics through points 1 and 2, and then ν and θ are calculated for the new point. From the values of ν and θ, the slopes of the two intersecting characteristics can be determined at point 3. A more accurate value for the intersection point of the curved characteristics can be obtained by projecting the characteristics along the averaged slopes. A new left-running characteristic slope is calculated by averaging the slopes at points 2 and 3. The new right-running characteristic slope is obtained similarly from points 1 and 3. These new slopes are then projected to construct a new location for point 3, at which new values of ν and θ are obtained. This process is repeated until the calculated flow conditions at point 3 converge to within a specified accuracy. The accuracy of this method may be increased by decreasing the mesh size, since the resulting shorter characteristics more closely approximate a straight line.

The construction for a lower boundary point on a solid surface is shown in Fig. 29b. For this situation only one upstream point and one characteristic equation are available for the calculation. However,

there is only one unknown at the boundary--the Prandtl-Meyer angle. The flow angle is known, since at a solid boundary the flow must be parallel to the surface. The solution is still iterative because of the curved characteristic between points 1 and 3, and the iteration proceeds in the manner outlined above for a field point.

For the calculation of a point on a constant pressure upper boundary, the construction in Fig. 29c is used. In this case, the Prandtl-Meyer angle, ν, is known from the pressure on the boundary, and only the flow angle must be determined. The equation for a left-running characteristic is used, and the iteration follows the standard procedure. Calculations for upper solid boundary points and lower constant pressure boundary points are analogous to those presented above. Care must be taken, however, to use the proper characteristic equations.

The standard method of characteristics was used to construct the solution of the nozzle flow field from the starting line to the shroud exit. It was discovered that, due to computer round-off error, the solution began to diverge in progressing downstream. This difficulty was overcome by re-incrementation of the most recent characteristic points at specified intervals. Basically, the process consisted of distributing the characteristic points evenly across the flow field before continuing downstream.

In addition to the re-incrementation during the internal expansion phase of the flow, a special routine was developed such that a row of characteristic points could be established at the nozzle exit plane. This step was necessary in order to control the depth of penetration of the expansion at the shroud exit corner. In general, the last row of characteristic points would not fall at the exit plane, and therefore the extent of the corner expansion would vary considerably for each case. The exit values were obtained by noting whenever a new characteristic point was located downstream of the exit. When this occurred, the values at the exit plane were calculated by a linear interpolation along the characteristic lines. After all points had passed the nozzle exit, the interpolated values at the exit were recalculated so that they were evenly distributed along the exit line. These points constituted the initial conditions for the downstream continuation of the solution.

Hartree Technique

Before undertaking a detailed explanation of the corner expansion process and the shock wave calculations, it is necessary to describe the modified calculation method that was used for the method of characteristics downstream of the shroud exit. This procedure was introduced by Hartree (Ref. 26), and therefore will be referred to as the Hartree Technique.

The difference between the standard and Hartree technique is demonstrated in Fig. 30. With the standard approach, a characteristic network is generated, as shown in Fig. 30a. Point A is calculated from the known

points B and C. The location of point A cannot be arbitrarily chosen, since it is uniquely determined by the intersection of the characteristics through points B and C.

In the Hartree Technique, illustrated in Fig. 30b, the location of point A can be chosen to simplify the computational procedure. Upstream conditions are known at points along the vertical line, $\tilde{X}$, which extends across the region under consideration. A second vertical line at $\tilde{X} + \Delta\tilde{X}$, is then constructed across the flow field, and points, at which downstream flow variables are to be calculated, are placed on this line. The calculation is started by assuming values for ν and θ at point A. Usually these values are set equal to the upstream values at the same radial location. Using the assumed ν and θ, a left and right-running characteristic is projected back upstream to line $\tilde{X}$. The projected characteristics intersect line $\tilde{X}$ at points B and C, and the flow conditions of these points are obtained by a linear interpolation between known values. Points B and C are then used in a standard calculation to establish a new point A, which in general will not coincide with the original location where the solution is desired. Therefore, new characteristic slopes are calculated by the averaging method and projected back upstream from the original location of point A. This process is repeated until the characteristics through B and C intersect at the location chosen for point A, and all flow variables have converged to within the required accuracy. The overall accuracy of this method has been shown to be comparable to the standard method of characteristics (Ref. 27).

The Hartree Technique requires considerably longer computational time than the standard technique. However, the convenience of being able to predetermine the location of downstream points outweighs this disadvantage. This scheme is most useful in the vicinity of an imbedded shock wave. Calculations across a shock wave require a characteristic point on both sides of the shock. In the standard method, these shock points must be determined by interpolation between neighboring points. This necessitates knowing the location of surrounding points with respect to the shock location, in order to determine which points to use in the interpolation. As a result, the computer bookkeeping becomes very complicated. With the Hartree Technique, shock wave points are handled with no more difficulty than a regular interior point. It is only necessary to place a point at the desired location and perform a standard Hartree calculation.

Added to the advantages mentioned above, the Hartree Technique has several other features that recommend its use. For example, the downstream step size can be chosen at will, instead of being determined by the shape of the characteristics.

The Hartree Technique was used for all calculations downstream of the shroud exit, with the only exceptions being the corner expansions and the region near the start of the internal shock. The calculational methods for these special regions will be described below.

Corner Expansion

Fig. 31 shows the construction of the characteristics used for the corner expansion. The solution is known at the exit plane from the upstream calculations. A line downstream at a distance $\Delta\tilde{X}$ from the exit is established, along which points in the solution are to be obtained. Using the point at the exit corner and the next point below it on the exit plane, a standard method of characteristics calculation is performed for the solution at the standard point shown in Fig. 31. A linear interpolation is then performed to determine the flow conditions on the new solution line. This defines the first ray in the expansion fan. The points below the first ray in the expansion fan are calculated using the Hartree Technique. Succeeding points in the expansion fan are calculated by first assuming a Prandtl-Meyer expansion at the exit corner. The total change in flow variables through the expansion corner is then divided into a number of equal steps (the number depending on the accuracy desired). The flow variables at the exit corner are set equal to the values for the next step in the expansion, and this point is used in conjunction with the previous point on the new solution line in a standard calculation. Linear interpolation is again used to place the new point on the solution line. This process is continued until the entire expansion fan has been calculated.

In order to determine the intersection of the constant pressure boundary with the new solution line, a line is extended through the exit corner at an angle equal to the flow angle after the expansion. Conditions along this line and at the first boundary point are set equal to the flow properties after the corner expansion. Characteristic points are then placed on the constant pressure boundary at equal increments. The solution between the last ray in the expansion fan and the constant pressure boundary point is constructed in the same manner as described above for expansion wave points.

Shock Wave Detection

In the method of characteristics solution, a shock wave is formed when two characteristics of the same family intersect. This situation can occur in the exhaust flow from an underexpanded rocket nozzle (Ref. 19). The constant pressure boundary originating at the exit is curved, and the characteristics emanating from this boundary will eventually converge. The standard procedure is to expand the flow to the ambient pressure, and then continue the calculations downstream until a shock is detected. With this method the initial shock wave point is not identified until a considerable distance downstream. In the actual case the shock originates near the shroud corner. The inviscid flow fails to negotiate the corner and overexpands to a pressure below the ambient pressure. The boundary layer overexpands with the inviscid flow, and the internal shock forms to return the pressure on the boundary back to the actual ambient pressure.

Because of the importance of detecting the internal shock wave in

the vicinity of the corner, where it is initiated, a modified calculation scheme was developed for this region. Fig. 32 shows the computation method used for this purpose. In order to partially account for the overexpansion, the flow is initially expanded to a pressure below the ambient pressure. After several steps downstream, the boundary pressure is returned to its actual value and the calculations proceed normally. Using this method, the initial shock wave point is detected close to the nozzle exit, and therefore the exhaust flow is more accurately modeled. The determination of the correct amount of overexpansion will be outlined in a later section.

It should be pointed out that overexpanding the flow at the corner is totally consistent with the situation in the actual case. Boynton (Ref. 28) has shown that the presence of the boundary layer produces a flow angle after the expansion, which is well above that predicted by inviscid theory. As explained above, the internal shock is formed because the flow initially overexpands and then recompresses through the shock wave.

Fig. 32 shows how the initial shock point is established by the intersection of two characteristics from the external boundary. Since the Hartree Technique dows not follow characteristics, it was modified for this purpose. New points, at which solutions are to be obtained, are established by the intersection of characteristics from the external boundary with the new solution line. As the iteration proceeds, the value of the axial coordinate is held constant while the value of the radial coordinate is allowed to "float." In this manner, the solution proceeds along characteristics. Only characteristics from the external boundary are developed as described above. The remaining points on a new solution line are calculated with the usual Hartree Technique.

When two characteristics intersect, the initial shock wave angle is set equal to the average angle of the intersecting characteristics. This shock angle is projected downstream to the next solution line. Points are then spaced above and below the shock and the solution proceeds. From this point on, characteristics are no longer followed, since the internal shock location has been determined and experimental evidence indicates that no other strong shocks exist.

Shock Wave Development

Fig. 33 shows the basic construction used for calculating the shock wave development. The physical location of the shock wave point on the new solution line is known from the projection of the upstream wave angle. Flow properties upstream of the shock (point E) are determined by the Hartree Technique, using the two points C and D. A new shock wave angle, β, is assumed, and conditions downstream of the shock are calculated using oblique shock relations. The downstream flow angle, θ_2, is held constant, and the Mach number at point B is iterated using point A on the known solution line. If the Mach number at point B, as calculated from the method of characteristics, does not agree with the Mach number

obtained from the oblique shock relations, a new β is assumed and the process repeated until convergence is reached. This determines the new shock wave angle which is then projected downstream.

In Fig. 33, points B and E are shown as distinct from the shock wave point, only for the purpose of clarifying the explanation. In the actual calculations, these points coincide with the shock point, since the shock is assumed to have negligible thickness.

Lip Shock

When the flow reaches the plug base, it undergoes an expansion about the corner because of the low plug base pressure. The overexpansion at the corner produces a shock wave in the same manner that the internal shock at the shroud was formed. This shock is called a lip shock, and has been studied in the experimental phase of this research. Results show that when the surface upstream of the base is inclined toward the axis (as with plug nozzles), the lip shock strength is greatly reduced. If, in addition, the boundary layer is turbulent, the lip shock almost totally disappears. Since these two situations existed in the cases studied, the lip shock was not included in the theoretical calculations. The flow is expanded to the assumed base pressure and no attempt is made to follow characteristics. The solution is continued along a conetail until the predetermined wake radius is reached. At this stage, the base pressure solution is initiated.

BASE PRESSURE SOLUTION

The flow model used for the determination of the turbulent base pressure is shown in Fig. 34. A complete derivation of the governing equations is presented in Appendix II of reference 15. This model was developed by Zumwalt (Refs. 23 and 29) and later modified by Mueller (Refs. 24 and 25) and Hall and Mueller (Ref. 21).

The following conditions are imposed on the base flow model:

a) The boundary layer approaching the separation corner is neglected, although fully turbulent mixing is assumed.

b) An isentropic expansion takes place at the base corner from (1) to (2), and the effect of a lip shock is ignored.

c) The inviscid flow past a conetail, using the rotational method of characteristics, is utilized to define the pressure field impressed on the mixing region from (2) to (3). This conetail surface also serves as the "corresponding inviscid jet boundary."

d) The pressure normal to the "corresponding inviscid jet boundary" is assumed to be constant within and near the mixing region at each cross section.

e) Velocity profile similarity is assumed in the mixing region. The error function velocity distribution is located within the intrinsic coordinates x, y, and is represented by $X \approx x$ and $Y = y - y_m(x)$ where $y_m(0) = 0$.

f) The geometry of the mixing region is taken into account in the integral representation for the momentum and mass flux between (2) and (3).

g) Recompression is assumed to result from an oblique shock turn from (3) to (4) at an empirically determined trailing wake radius ratio.

A streamline, j, can be identified which divides the amount of mass passing over the corner at (1) from the mass flow entrained by the viscous action of the free jet mixing region. Another streamline, d, can be identified which has just sufficient kinetic energy at (3) to negotiate the pressure rise at (4). Streamlines below the d-streamlines have lower kinetic energy and are not able to pass through recompression. These streamlines are turned back to recirculate in the base region. In the absence of base bleed, conservation of mass requires that the j- and d-streamlines be identical.

The control volume between cross-sections (2) and (3) is bounded by streamlines R and -R, as shown in Fig. 34. These streamlines were defined by Zumwalt so that the cross-sectional area normal to the direction of flow would remain nearly constant, and the PdA pressure force could be neglected in the momentum equation. For the axisymmetric flow field described above, Zumwalt formulated the momentum equation in the axial direction using geometrical relations and the relation between the viscous and inviscid coordinate systems. This equation was solved simultaneously with combined viscous and inviscid continuity equations written for the control volume between cross-sections (2) and (3). For the error function velocity profile, $\phi = \frac{1}{2}(1+\mathrm{erf}\eta)$, where $\phi = u/u_a$ and $\eta = \sigma y/x$, it was found that $\eta_R = 3$ was large enough for ϕ_j to approach its asymptotic value. The result of this analysis is a nonlinear equation which is used to locate the j-streamline at cross-section (3), namely:

$$\left\{(B-3)^2+2(1-C_{3a}^2)\left[I_1\Big|_{-\infty}^{3}-I_1\Big|_{-\infty}^{\eta_j}\right]B-2(1-C_{3a}^2)\left[J_1\Big|_{-\infty}^{3}-J_1\Big|_{-\infty}^{\eta_j}\right]\right\}_{3a} = \left(\frac{\sigma\bar{r}}{x\cos\theta}\right)^2_{3a} \qquad (1)$$

where the integral limits refer to η values, and:

$$B = \frac{J_1\Big|_{-\infty}^{\eta_j}-\left[1-(C_{3a}/C_{2a})\right]J_1\Big|_{-\infty}^{3}-(C_{3a}/C_{2a})(J_1-J_2)\Big|_{-\infty}^{3}}{I_1\Big|_{-\infty}^{\eta_j}-\left[1-(C_{3a}/C_{2a})\right]I_1\Big|_{-\infty}^{3}-(C_{3a}/C_{2a})(I_1-I_2)\Big|_{-\infty}^{3}+\left[(\gamma-1)/\gamma\right](3/C_{2a}C_{3a})\left[1-(P_2/P_3)\right]}$$

where:

$$I_1 = \int_{-\infty}^{\eta}\frac{\phi d\phi}{1-C_{3a}^2\phi^2} \qquad (3)$$

$$I_2 = \int_{-\infty}^{\eta} \frac{\phi^2 d\eta}{1-C_{3a}{}^2\phi^2} \tag{4}$$

$$J_1 = \int_{-\infty}^{\eta} \frac{\phi\eta d\eta}{1-C_{3a}{}^2\phi^2} \tag{5}$$

$$J_2 = \int_{-\infty}^{\eta} \frac{\phi^2\eta d\eta}{1-C_{3a}{}^2\phi^2} \tag{6}$$

It should be noted that since these integrals are expressed only in terms of Crocco number, C, they are independent of the ratio of specific heats, γ, although Equation 1 is a function of γ.

In order to determine ϕ_{j_3} from Equation 1 for a given initial condition, the location of recompression, $\bar{r}_3/r_b$, the corresponding inviscid Mach number, M_{3a}, and the jet spread parameter, σ_{3a}, must be known. The location of recompression, r_3/r_b, is determined from experimental data. The Mach number along the inviscid boundary at (3), M_{3a}, is determined from the axisymmetric rotational method of characteristics. The jet spread parameter is established using the equation given by Channapragada (Ref. 30):

$$\sigma_{3a} = \left[R'\{1 + \beta(1 - C_{3a}{}^2)\}\right]^{-1}\sigma_{inc} \tag{7}$$

where $\sigma_{inc} = 12.0$ for the error function velocity profile, $\beta = T_{01}/T_b$ ($\beta = 1.0$ for isoenergetic mixing), and R' is the empirical compressible divergence factor defined by Channapragada as a function of the Crocco number.

The geometric parameter, $\left(\frac{\sigma\bar{r}}{x\cos\theta}\right)$, may be calculated since $\theta_{3-4} = \theta_{1-2}$ from the conical wake assumption, and since:

$$\left[\frac{\sigma\bar{r}}{x\cos\theta}\right]_{3a}^2 = \left[\frac{\sigma\tan\theta}{\left[1/(\bar{r}/r_b)-1\right]}\right]_{3a}^2 \tag{8}$$

At this point, $\phi_{j_3} = \phi_{d_3}$ (for no base bleed) may be obtained from Equations 1 and 2. Therefore, $C_{d_3} = \phi_{d_3}C_{3a}$ for isoenergetic flow. However, the value of C_{d_3} may also be determined from the assumed isentropic recompression mechanism along the d-streamline (i.e., $P_{0_{3d}} = P_r$) from:

$$C_{d3} = \{1 - (P_4/P_3)^{-\left[(\gamma-1)/\gamma\right]}\}^{\frac{1}{2}} \tag{9}$$

where P_4/P_3 is the static pressure rise across the two-dimensional oblique shock which results from the turning of the flow with Mach number M_{3a} through the angle ϕ_{3-4}. When the two values of C_{d_3} are equal then the assumed base pressure ratio is correct for the prescribed initial conditions and nozzle geometry. If the values of C_{d_3} are not equal, a

new base pressure is assumed, and the method of characteristics solution is reinitiated at the plug base. A typical solution curve is shown in Fig. 35. The values of C_{d3} resulting from the above equations are subtracted from each other such that the solution always occurs at zero.

The base pressure analysis described above does have a strong theoretical basis. However, empirical or semi-empirical inputs are still required. A lack of knowledge and understanding of certain facets of the flow make these inputs necessary. In order to use the analysis developed by Mueller (Ref. 24), it is necessary to specify the jet spread parameter, σ_{3a}, which describes the rate at which the width of the shear layer increases in the streamwise direction. The jet spread parameter has been investigated by many authors, and is based on empirical formulations. For the solution presented in this report the jet spread parameter obtained by Channapragada (Equation 7) was used. Another empirical variable which must be included in the base pressure solution is the wake redius ratio, r_w/r_b. This locates the point in the flow field at which recompression is assumed to occur. Based on the work of Mueller (Ref. 24) and shadowgraphs of the nozzle flow field (from the present study), it was decided to use a constant value of 0.50 for the wake radius ratio.

Calculation Procedure

For a given (or calculated) flow field up to the plug base, the calculation procedure for determining the base pressure is as follows:

1. Estimate the value of the base pressure ratio, P_b/P_{01}, and knowing P_1 and M_1, obtain the ratio P_b/P_1. (The terms P_1 and M_1 are the pressure and Mach number at the end of the plug.)

2. $P_b/P_{01} = P_2/P_{01}$ because of the assumption of no pressure gradient in the y-direction. The pressure ratio P_2/P_{01} determines the Mach number M_{2a} and the corresponding Prandtl-Meyer angle, ν_{2a}. The difference in Prandtl-Meyer angles ($\nu_{22} - \nu_{1a}$) determines the change in streamline angle at the plug base (i.e., $\theta_1 - \theta_2 = \nu_{2a} - \nu_{1a}$).

3. Determine a wake radius ratio, r_w/r_b, and perform a method of characteristics solution to a radius, r_w. This determines the Mach number, M_{3a}, at recompression.

4. Determine the location of the j-streamline by iteratively solving Equation (1). The value of the jet spread parameter, σ_{3a}, is that formulated by Channapragada, Equation 7. Also, $\theta_{1-2} = \theta_{3-4}$. The solution to this equation is double-valued, and the larger value of ϕ_j is used for external flows.

5. For no bleed, $\phi_d = \phi_j$ and:

$$C_{d3} = \phi_{d3}C_{3a} = \phi_{j3}C_{3a}$$

6. Also:

$$C_{d3} = \left[1 - \frac{1}{\left[\frac{P_4}{P_3}\right]^{\frac{\gamma-1}{\gamma}}}\right]^{\frac{1}{2}} \quad \text{since } P_{03d} = P_4$$

where P_4/P_3 is the pressure rise across an oblique shock of a stream flowing at a velocity M_{3a} deflected through an angle θ_{3-4}.

7. When the value of C_{d3} obtained from steps 5 and 6 agree, a solution is obtained.

THRUST DETERMINATION

Knowing the general picture of the T-P nozzle flowfields, force component diagrams can be drawn. Fig. 36a shows such a diagram for calculating the thrust of the particular nozzle configuration of interest in this report. Neglecting skin friction effects, the static thrust developed by this T-P nozzle is equal to the change in momentum of the exhaust flow plus the summation of the axial components of all external pressure forces, or

$$F_x = \Delta\tilde{M}_x + \int P_x dA \tag{10}$$

where $\Delta\tilde{M}$ = change in momentum of exhaust flow.

The change in momentum of the exhaust is equal to the product of the mass flow rate ($\dot{m}$) and the axial component of the velocity to which the gas has expanded (u_x). The mass flow rate is the product of the gas density, the axial velocity component, and the cross-sectional area of the flow field. The gas density, ρ, is a function of the pressure P, the gas temperature T, and the gas constant)R, as expressed by the ideal gas law. The velocity u can be expressed as a function of the Mach number M, the ratio of specific heats of the gas γ, the gas temperature, and the gas constant. The axial component of velocity u_x is a function of the velocity and the flow angle θ. Thus the momentum flux $\Delta\tilde{M}_x$ can be expressed as follows:

$$\Delta\tilde{M} = (\rho u_x A)u_x = \gamma P A M^2 \cos^2\theta \tag{11}$$

The flow properties across a T-P nozzle exhaust plane are not uniform. However, since the inviscid external flowfield is calculated by the method of characteristics, the flow properties are calculated at points spanning the shroud exit plane of the nozzle. In calculating the momentum flux, separate annular elements of area elements, dA, enclosing each point are defined as shown in Fig. 36b. The flow properties at each point are assumed to be the flow properties for each respective annulus. Then the momentum flux is the summation of the momentum flux components of the annuli, or

$$\Delta\tilde{M} = \sum_{i=1}^{nl} \gamma P_i M_i^2 \cos^2\theta_i dA_i; \quad \text{for nl = the number of annuli} \tag{12}$$

The pressure forces (with axial components) act only on the shroud exit plane, the plug contour and the plug base. These pressure forces, like the other flow properties, are not uniform except for the plug base. Again, as a result of the method of characteristics solution, the pressures are known at points located along all the surfaces of interest. Annuli enclosing each point can be defined as was done in the momentum flux calculations. The pressure forces can then easily be calculated using the summation,

$$\int P_x dA = \sum_{i=1}^{n2} (P_i - P_{at}) dA_i \tag{13}$$

n2 is the number of total annuli.

P_{at} is the ambient pressure of the quiescent air into which the nozzle exhausts.

The total thrust is calculated in two parts. The first part calculates the thrust contributed by the flow at the nozzle exit plane.

$$T_1 = \sum_{i=1}^{n1} \gamma P_i M_i^2 \cos^2\theta_i dA_i + \sum_{i=1}^{n1} (P_i - P_{at}) dA_i \tag{14}$$

n1 is the number of characteristics points located along the shroud exit plane.

The second part of the calculations determines the thrust contributed by the pressure forces on the plug surface.

$$T_2 = \sum_{i=1}^{j} (P_i - P_{at}) \cos\theta_i dA_i \tag{15}$$

j is the number of characteristic points located along the plug surface (j = n2-n1).

The total static thrust component is then the summation of T_1 and T_2. A thrust coefficient is calculated by using the product of the nozzle chamber pressure and the nozzle throat area ($P_{01} \cdot A_{nt}$) i.e., $C_T = \frac{\text{THRUST}}{P_{01} \cdot A_{nt}}$

TRANSONIC SOLUTION

The work of Hall and Mueller (Ref. 21) has shown that the location, shape, and distribution of flow properties along the sonic line may significantly affect the performance characteristics of a T-P nozzle. A 17% variation in the computed value of the base pressure was noted when the shape of the sonic line was changed from linear to parabolic.

This rather significant effect indicates the necessity of accurately determining the gas properties in the transonic region of these nozzles, if the overall performance is to be accurately predicted. As is common, this task is more easily stated than performed.

The principal obstacles to obtaining a direct closed form solution in the transonic region include: the character of the governing equation, which is both nonlinear and of the mixed type (Ref. 31), and the irregular contour of the nozzle wall normally chosen by designers. While in the past most transonic problems of this type have been handled by an inverse method of solution (Ref. 32), it appears possible to solve this problem directly if certain assumptions and approximations are applied. The method which leads to this direct solution involves reducing the complex original problem to a simpler problem to which the solution is either known or may be determined.

In order to meet design criteria other than the determination of the flow field, the wall contour of a T-P nozzle is often highly complex in nature. Solutions to even the most trivial boundary value problems are rare in regions bounded by curves as complicated as those which form the contours of a typical T-P nozzle. For this reason, it was decided to attempt a solution in a small region of the nozzle known to contain the sonic line, and to make further assumptions as to the character of the wall contour within this region. More specifically, it was assumed that the wall contour could be approximated by circular arcs in this transonic region. Fig. 37 shows the region to be used for computation in both a T-P nozzle and a conventional bell type nozzle. When a few additional restrictions are placed upon the throat gap, and radius of curvature, it becomes possible to devise a system of co-ordinate curves, composed entirely of circular arcs, which are orthogonal everywhere in the region of interest. This system of co-ordinates is commonly called bipolar, and is shown in Fig. 38.

The bipolar co-ordinate curves, ξ = constant or η = constant, are generated as solutions to the transformation equations.

$$x = \sin(\xi)/(\cosh(\eta)+\cos(\xi))$$
$$y = \sinh(\eta)/(\cosh(\eta)+\cos(\xi)) \tag{16}$$

This system of co-ordinates may also be produced by a transformation from the complex plane (ξ, η) to the real plane, (x, y) (Ref. 33).

$$i\bar{Z} = \frac{a(e^{W}+1)}{(e^{W}-1)} \tag{17}$$

$$Z = x + iy$$
$$W = \xi + i\eta \tag{18}$$

Each line of constant ξ or constant η can be shown to be a circle in

the real plane. The circles of constant ξ value have their centers restricted to lie on the x axis of the (x, y) plane. Similarly the circles of constant η value have their centers restricted to lie on the y axis. If both ξ and η are confined to the region defined as

$$-\pi/2 \leq \xi \leq \pi/2$$

$$\pi/2 \leq \eta \leq \pi/2$$

the transformation is single valued.

Any region, whose boundaries lie on lines on constant ξ and η in the real plane, may be transformed into a rectangular region in the complex plane. Thus under certain limiting assumptions as to the nature of the wall contour within only a small portion of the nozzle, it is possible to simplify the geometry of the region of interest. While this assumption simplified the problem greatly, it was still necessary to deal with the nonlinear character of the governing equation.

It is well known that the flow of an incompressible gas is governed by Laplace's equation for the velocity potential.

$$\Delta\phi = 0 \tag{19}$$

However, when the effect of compressibility is included, the equation becomes nonlinear and correspondingly more complex.

$$\left[1-\left(\frac{\phi_x}{c}\right)^2\right]\phi_{xx}-\frac{2}{c^2}\phi_x\phi_y\phi_{xy} + \left[1-\left(\frac{\phi_y}{c}\right)^2\right]\phi_{yy} = 0 \tag{20}*$$

where

$$c^2 = c_0^2 - \frac{\gamma-1}{2}\left[(\phi_x)^2 + (\phi_y)^2\right] \tag{21}$$

Upon examination of the new governing equation, it is clear that it still contains the Laplacian of the velocity potential together with other second order derivatives which are nonlinear. If these nonlinear terms are gathered together,

$$\Delta\phi = \frac{1}{c^2}\left[(\phi_x)^2\phi_{xx}+2\phi_x\phi_y\phi_{xy}+(\phi_y)^2\phi_{yy}\right] \tag{22}$$

the governing equation is similar to an inhomogenous Laplace's equation, sometimes called a Poisson equation, with the inhomogenous term being comprised of the nonlinear compressibility terms.

$$\Delta\phi = -f \tag{23}$$

*Subscripts x, y, ξ, η, n indicate partial differentiation with respect to the subscript variable.

where

$$f = \frac{-1}{c^2}\left[(\phi_x)^2\phi_{xx}+2\phi_x\phi_y\phi_{xy}+(\phi_y)^2\phi_{yy}\right] \tag{24}$$

This similarity led to the idea that treating the equation as an inhomogenous Laplace's equation would lead to the desired solution, if a compressibility function, f(x, y), could be constructed which provided an accurate approximation to the nonlinear compressibility terms. Before discussing the method used to approximate the compressibility function, it is necessary to consider the effect of transforming the governing equation to the ξ, η plane.

The transformed equation can be seen to be nearly identical with the equation in the (x, y) co-ordinate system. The primary difference is the presence of an additional term arising from the transformation of the nonlinear terms.

$$\Delta_{(\xi,\eta)}\phi = -f^T \tag{25}$$

$$\begin{aligned} f^T = \frac{-1}{c_0^2}\Big\{ & K_1\left[\frac{\gamma+1}{2}(\phi_\xi)^2+\frac{\gamma-1}{2}(\phi_\xi)^2\right] \\ & + K_1\left[2\phi_\xi\phi_\eta\right]\phi_{\xi\eta} \\ & + K_1\left[\frac{\gamma-1}{2}(\phi_\xi)^2+\frac{\gamma+1}{2}(\phi_\eta)^2\right]\phi_{\eta\eta} \\ & + \left[\frac{K_2}{K_1}\phi_\xi+\frac{K_3}{K_1}\phi_\eta\right]\left[(\phi_\xi)^2+(\phi_\eta)^2\right]\Big\} \end{aligned} \tag{26}$$

and

$$\begin{aligned} K_1 &= (\xi_x)^2+(\xi_y)^2 \\ K_2 &= \{(\xi_x)^2-(\xi_y)^2\}\eta_{xy}+2\xi_x\xi_y\xi_{xy} \\ K_3 &= -2\xi_x\xi_y\xi_{xy}+\{(\xi_x)^2-(\xi_y)^2\}\xi_{xy} \end{aligned} \tag{27}$$

All additional complexity introduced by this transformation can be absorbed into the new compressibility function. The problem may then still be treated as an inhomogenous Laplace's equation, but as a result of the earlier assumptions the geometry in this plane is a rectangle.

The problem of constructing a sufficiently accurate compressibility function remains. Were the solution to the problem known there would be little problem in differentiating and evaluating the compressibility function. Similarly, were an approximation to the solution known, an approximation to the compressibility function could be easily determined. An initial approximation to the compressibility function can be made based on the assumption of one-dimensional flow within stream tubes, formed by the co-ordinate curves. The flow field corresponding to this compressibility function can then be calculated. If further increases in accuracy are desired, a more accurate approximation to the compressibility function can be determined, based on this flow field. Thus an iterative

process is developed, by which the compressibility function may be approximated as accurately as desired.

These simplifications lead to a solution by treating the original problem as an elliptic rather than a mixed type equation. There are certain aspects of the mixed type equation which must be retained, notably, the boundary conditions which are necessary to fully determine the solution. When treating the governing equation as elliptic in nature, it is necessary to specify the normal derivative on the downstream boundary. Due to the actual mixed type of the equation, the normal derivative is not known on this boundary. It is possible to determine the value of the normal derivative on the outflow boundary, which are compatible with the sonic line within the flow field by use of the Method of Characteristics. The problem may then be fully and properly specified, and a solution may be obtained, if the normal derivative is specified on the wall contours and at the inflow boundary,

$$\phi_n = 0 \quad \text{on walls} \tag{28}$$

to assure no flow through the walls, and

$$\phi_n = g_s(\xi_s, \eta) \tag{29}$$

at the inflow boundary. This last boundary condition is the same as specifying the velocity normal to the inflow boundary.

The problem has been simplified to what is frequently called a Neumann Problem on a rectangle. While a closed form analytic solution to this problem does exist (Ref. 34), it is extremely time consuming to evaluate the formula. For this reason the solution was approximated by a finite difference scheme. A Jacobi iteration scheme was used to solve the equations as the normally more efficient Gauss-Seidel and successive over-relaxation methods cannot be used on this type of problem.

A computer program was developed to execute all of the necessary steps leading to a solution in accordance with the method of solution described above. This program was compiled and run on the University of Notre Dame's IBM 370-155 computer. Approximate computer storage was 96K bytes.

DISCUSSION OF ANALYTICAL RESULTS

A Fortran IV computer program combining the rotational method of characteristics and the base pressure solution technique was written for the University of Notre Dame UNIVAC 1107. The iterative solution of the flow field and base pressure for the conical-plug cylindrical-shroud, T-P nozzle required that the downstream step size for the Hartree Technique as well as the amount of overexpansion be specified at the outset.

In most cases, the downstream step size, $\Delta\tilde{X}$, used in the Hartree

Technique, is under the control of the user and is adjusted according to the accuracy desired. This general rule, however, does not apply in the region of the initial shock wave development. The difficulty encountered in this area can be explained with the aid of Fig. 33. The point A is used for the calculation of point B behind the shock. In the vicinity of the initial shock wave development, the shock points are quite close to the external boundary. If the step size is chosen too large, the location of point A will be above the external boundary, where the solution does not exist, and the calculations at point B will not be possible. The value of $\Delta\tilde{X}$ necessary to avoid this situation must, in general, be found by trial and error. However, the following procedure has proven successful for all cases studied in the present investigation.

The two points at the shroud exit plane with the lowest Mach numbers were used in a standard method of characteristics calculation for a third point downstream. The points with the lowest Mach numbers were used, since this gave the smallest downstream distance to the new point. The step size was then set equal to 80% of the distance from the exit plane to the new point. For the cases studied, this distance was equal to 0.003328 in. (0.008453 cm) ($\Delta\tilde{X}/r_{sh}$ = 0.00824).

As the calculations proceeded downstream, the shock wave point moves away from the external boundary and it is possible to increase the step size. For the solutions obtained during this research, the step size was doubled after a short distance downstream. The solutions with the larger step size differed by less than 0.2% from the solutions that retained the original $\Delta\tilde{X}$.

By using the overexpansion at the shroud exit, as explained in the Method of Solution, the internal shock wave is detected in the vicinity of the exit corner. However, the question arises as to the effect of the overexpansion on the subsequent development and location of the shock.

The effects on the internal shock location for overexpansions of 75%, 85% and 95% are shown in Fig. 39. The value of the pressure, to which the flow is expanded, is determined by multiplying the percent overexpansion by the actual ambient pressure. These results show that changes in the amount of overexpansion have only a small effect on the shock wave location. The total deviation between the results for 75% and 95% overexpansion is less than 4%. This implies that an optimum value for the overexpansion can be selected without the need for extensive empirical correlations. Based on this and the experimental data shown in Fig. 39, a value for the overexpansion of 85% was used for all analytical solutions presented. The reason for the discrepancy between theory and experiment near the nozzle exit (L_{sh} = 0.300 in. (0.762 cm); L_{sh}/r_{sh} = 0.742) will be explained in a later section.

Ambient Pressure

As rocket or air-breathing engines are operated at increasing altitudes,

the ambient pressure decreases while the chamber pressure remains relatively constant. This variation of ambient pressure has a very pronounced effect on the flow fields of plug nozzle configurations. Figs. 40 and 41 indicate the influence of ambient pressure ratio on the location and shape of the external constant pressure boundary and the internal shock wave respectively. Ambient pressure ratios above 0.18 were not used since according to Fig. 13 the wake would not be "closed" for this T-P nozzle. Despite the large effects of the changing ambient pressure on the constant pressure boundary and internal shock wave shown in Figs. 40 and 41, the base pressure remains constant. This results from the fact that the wake is "closed" and that there is no interference in the near wake from the external flow.

Nozzle Geometry

For truncated plug nozzles there are a large number of geometries possible. Having restricted this present study to the conical-plug, cylindrical-shroud T-P nozzle, the effects of shroud length, plug length, and plug angle on the flow field and base pressure were documented for "closed wake" operation.

Shroud Length

The effect of shroud length on the inviscid flow (i.e., constant pressure boundary and internal shock) is shown in Fig. 42. The corresponding effect of shroud length on the base pressure ratio is presented in Fig. 43. These calculations indicate that for 100% increase in shroud length, the base pressure ratio increases by about 104%. The longer the shroud, the greater is the internal expansion. The length of the shroud therefore, is determined by the amount of internal expansion desired.

Plug Length

As the plug length is increased, the nozzle flow expands further before reaching the end of the plug. This higher Mach number at the plug corner produces a lower base pressure (Ref. 25). Fig. 44 shows the magnitude of the base pressure ratio decrease with increasing plug length ratio for both ATP1 and ATP2. The larger area ratio nozzle (ATP2) has the lower base pressure ratio since the Mach number approaching the base corner is higher than for the lower area ratio case (ATP1).

Plug Angle

The influence of plug angle on the constant pressure boundary and internal shock locations for two plug lengths is presented in Figs. 45 and 46. As the plug half-angle, α, increases, the expansion ratio from the throat to the shroud exit increases although the throat area and overall nozzle exit area remain constant. Thus the Mach number at the shroud exit is higher and the static pressure is lower. The pressure at the shroud exit is still higher than the ambient but less expansion

is necessary to meet the ambient pressure than for a smaller value of α. Therefore the constant pressure boundary moves toward the nozzle axis as α increases. The internal shock also moves toward the nozzle axis since the smaller expansion from the shroud exit pressure to the ambient pressure produces a smaller local overexpansion, in the vicinity of the shroud exit, which generates the internal shock. Although the plug length in Fig. 45 is $L/L_{max} = 0.3275$ and that of Fig. 46 is $L/L_{max} = 0.3785$, the constant pressure boundaries and internal shock locations are identical as far as they are drawn. Any influence of this part of the external flow field by the plug length would occur further downstream.

The effect of plug angle on base pressure ratio for the cases shown in Figs. 45 and 46 is presented in Fig. 47. Plug length strongly influences the flow in the vicinity of the near wake and therefore the base pressure. The increase in base pressure ratio with increasing plug angle shown in Fig. 47 is consistent with the earlier analytical results of Mueller (Ref. 25) which agreed very well with experiments.

Ratio of Specific Heats

The comparison of analytical and experimental results to be presented later will be for the ratio of specific heats, γ, of 1.4. This is the value for air and is used extensively in this investigation since air is the working fluid in the experimental facility. In nozzle exhaust flows, however, the value of γ will depend on the particular fuel, oxidizer, fuel-oxidizer ratio, chamber temperature and pressure, etc. Analytical solutions were obtained to determine the effect of γ on the internal shock wave location and the plug base pressure. Fig. 48 presents the effect of γ on the internal shock location. A significant change is evident in the shock position, with the difference increasing with downstream distance. The end point of the shock wave for $\gamma = 1.2$ at $\ddot{X}/r_{sh} = 2.10$ is 30% higher than the end point for $\gamma = 1.667$. The variation of the plug base pressure ratio is shown in Fig. 49. The trend of increasing base pressure with γ coincides with other analytical results (Ref. 24) but no experimental verification has been obtained.

Thrust

Static thrust performance for varying plug length ratios is shown in Fig. 50. As the plug length increases, the thrust decreases for both ATP1 and ATP2. This indicates that truncating the plug will increase thrust performance of a particular nozzle, and that a nozzle plug length is an important parameter in the nozzle design. These results may be readily explained. As the plug length increases there is more plug surface being acted on by the flowfield pressure forces. The flow expands along the plug surface until at some point the pressure is lower than the ambient pressure, and thereafter a drag force results. This drag increases as the plug length increases causing the static thrust to decrease. The base pressures during "closed" wake operation are usually higher than the ambient pressure, so the base region contributes to the thrust. But as the plug length increases both the base pressure and

base area decrease resulting in a smaller base region thrust component. The net result is to develope less thrust for longer plugs. Fig. 50 also shows improved thrust performance with decreasing throat area and nozzle area ratio. The nozzle size should not affect performance since the shroud and plug boundary layers were not considered in this analysis. Thus this performance difference results from the difference in area ratio. However the difference in thrust coefficient ($T/P_{01}A_{nt}$) shown in Fig. 50 is attributed more to the decrease in nozzle throat area than to area ratio associated performance losses.

Thrust performance for varying plug half-angle (α) is shown in Fig. 51. The increases in thrust with plug angle increases is a result of the increased flow expansion with increased plug angle. When the flow expands more, the momentum flux component of thrust (the principle component) increases. In addition, because the base pressure increases with increasing plug half angle, the base region contributes additional increases in thrust. In designing T-P nozzles it is important to realize that increasing the plug half-angle could eventually cause separation of the flow from the plug surface. The analytical procedures used to calculate these thrust relations cannot calculate, or even predict this separation. It is advisable to limit plug half-angles so that the flow will remain attached on the entire plug length.

COMPARISON OF EXPERIMENTAL AND ANALYTICAL RESULTS

The comparison between theory and experiment are shown in Figs. 52 and 53 for the location of the internal shock wave for ATP1 and L/L_{max} = 0.2327 and 0.4802 respectively. The results presented for these two plug lengths are typical of all the plug lengths studied. Solutions were obtained for three overall pressure ratios for each of the plug lengths studied, in order to demonstrate the versatility of the analytical method. The overall pressure ratios were chosen to give as large a variation as possible within the limits of the NTF during the "closed wake" operation. The theoretical solution detects the shock near the shroud exit, $\ddot{X}/r_{sh}$ = 0.742. However, because of the difficulty in obtaining data from the shadowgraphs this close to the exit, the plots for both the shock wave location and constant pressure boundary location are initiated at a dimensionless distance of $\ddot{X}/r_{sh} \approx 1.0$ from the nozzle throat. Since the solution terminates at the trailing wake radius ratio, the results extend further downstream as the plug length is increased.

The analytical and experimental results show very good agreement for all cases, which justifies the use of a constant overexpansion. The largest deviations, on the order of 10%, occur for the longer plug lengths. This is probably due to the error involved in measuring the smaller base radii which are used as a reference in the photographs. Another feature of the results is that, in general, the difference between experiment and theory is greatest near the nozzle exit and decreases with distance downstream. The reason for this is that the overexpansion technique used at the exit does not fully account for all the viscous effects associated with the boundary layer expanding around the corner. As the solution proceeds downstream, the viscous effects diminish and the analytical results more closely approximate the actual shock location. For example, for the case with L/L_{max} = 0.4802 and P_{at}/P_{01} = 0.135, the difference between theory and experiment at $\ddot{X}/r_{sh} \approx 1.0$ is about 10%. However, for the same case, the error has decreased to less than 1% at the downstream location at which the solution ends.

In Figs. 54 through 55, the analytical and experimental results for the constant pressure boundary location are presented for the same configurations for which the internal shock wave results were obtained. The correlation between experiment and theory is excellent, with the maximum discrepancy (Fig. 55a) equal to 5.4% which is on the order of the experimental accuracy. It appears as though the viscous interactions at the corner have much less effect on the constant pressure boundary than on the shock wave. As was the case with the internal shock, the agreement improves with distance downstream.

The analytical values of the base pressure ratio for the plug lengths studied for both ATP1 and ATP2 are compared with the experimental data in Fig. 56. Theoretical base pressures were not obtained for plug lengths smaller than $L/L_{max} \approx 0.220$ for ATP1 and $L/L_{max} \approx 0.135$ for ATP2. The reason for this is that shorter plugs would end upstream of the shroud exit plane. Care had to be used in calculating the base

pressure of the short plugs because often the solution would converge using an isentropic recompression instead of the known shock recompression. For these plug lengths, if the base pressure at the current iteration was low, the flow deflection angle at recompression exceeded the critical angle for the Mach number upstream of recompression, M_{3a}. This situation arose because the low area ratios of the experimental nozzles and the short length of the plugs, coupled with the low base pressure guess (and resulting extra short near wake) allowed only a small distance for the flow to accelerate before recompression was reached. The turning angle, as calculated, was greater than it actually should be. The combined effect results in M_{3a} being too low for the necessary turning angle at recompression. In most nozzle configurations the area ratios would be larger, and the plugs would not be as short, so this difficulty should not be encountered.

Base pressure solutions were calculated with a shock recompression for all the plug lengths studied experimentally. Reasonable agreement was obtained between experiment and theory for all but the shortest plug length for ATP1, as shown in Fig. 56. The difference between analytical and experimental base pressure was greater for this plug than for the other plugs. The shadowgraphs for this plug (Fig. 15) indicated nothing unusual which might account for the lower base pressure. It is possible that the boundary layer on this shortest plug was not fully turbulent before separation at the plug corner. The base pressure depends on the degree of mixing in the viscous free shear layer and if this layer was transitional the base pressure could be lower than if this layer is fully turbulent. In actual nozzle configurations, the area ratios will be greater and the nozzles will be larger, and the flow would always be expected to be fully turbulent in the boundary layer along the plug.

The theory also correctly predicted the trend of decreasing base pressure with increasing area ratio. The agreement between theory and experiment improved for the increase in area ratio from ATP1 to ATP2. This was probably a consequence of the larger size of ATP2. With increased size, the viscous effects of the boundary layers became less influential. These viscous effects were not included in the method of characteristics calculations. A problem was encountered in calculating the flowfield for some special cases for area ratios larger than 17. When the Mach number at the shroud exit plane was large, the internal shock was initiated very close to the constant pressure boundary. In this case the first characteristics points crossing the shock could no longer be calculated for the normal Hartree step size, because the right running characteristics for these points project outside of the constant pressure boundary. This problem could be overcome by decreasing the Hartree step size. This has the added advantage of increasing the accuracy of the calculations which is needed for the higher Mach numbers.

In the region of practical interest, the theoretical base pressure averages about 15% higher than the experimental values. While this agreement is not excellent, it does represent a substantial improvement over the solution which does not include the internal shock wave, i.e.,

Refs. 20 and 21. For ATP1 with L/L_{max} equal to 0.4810, the experimentally determined value of the base pressure ratio is 0.070. Using the no-shock solution (Ref. 21), the analytical value of P_b/P_{01} was 0.0879 as contrasted to a value of 0.0783 for the present method, which includes the internal shock. Thus, the error in the base pressure has been reduced from 27% to 12%, or less than half the error for the no-shock solution. These results clearly demonstrate the necessity of including the internal shock for an accurate base pressure solution. This improvement can be explained with the help of Fig. 57. These results show the analytical Mach number distribution along the plug surface from the starting line to the plug base. The Mach number distribution on the shroud surface is included for completeness. The flow accelerates through the internal expansion portion of the nozzle, and then continues to expand at a constant rate until the expansion wave from the shroud intersects the plug. At this point, the Mach number gradient begins to increase and the value of the surface Mach number becomes continually larger up to the plug base. The Mach number just upstream of the corner expansion, M_{1a}, for this case is equal to 1.965. In Fig. 57 there is no evidence of compression waves impinging on the plug surface. However, when the internal shock wave is not included, compression waves from the constant pressure boundary are able to penetrate to the plug surface, and thereby decrease M_{1a}. For the no-shock solution, a value of 1.876 is obtained for the Mach number at the plug base. This lower Mach number results in a higher base pressure. With the internal shock included in the solution, the compression waves from the constant pressure boundary coalesce behind the shock (as in the actual case), and are not able to reach the plug surface. It is therefore very important to include the internal shock in the nozzle flow field solution if an accurate base pressure is desired.

With the internal shock included in the flow field solution, the theoretical base pressure is still about 15% high. There are several possible reasons for this difference. The most plausible cause, however, is the viscous effects of the boundary layers on the nozzle surfaces. The nozzles used in this investigation had very small throat areas and therefore the viscous effects, which are not included in the method of characteristics calculations, could be quite important. This effect would probably be less critical for larger nozzle configurations. Indeed the theoretical base pressure is only, on the average, 10% high for the larger nozzle ATP2.

Fig. 58 shows several isotachs, lines of constant velocity, calculated using the analytic procedure described earlier. As was expected, the fluid in the vicinity of the wall was accelerated to the sonic condition more quickly than the fluid near the centerline. The characteristics of the calculated flow field are similar to those reported by other authors (e.g., Ref. 32 and 35).

Any attempt to compare the shape of the analytically produced isotachs with the experimental data, was precluded by insufficient accuracy in the experimental data. As an example of the difficulties encountered

in locating the isotachs experimentally, the size of the pressure taps should be considered. The pressure taps were constructed from 0.032 in (0.081 cm) hypodermic tubing. On the non-dimensional scale of Fig. 58, this is equivalent to 0.16 units, or more than twice the maximum deflection of the sonic line from the geometric throat. The probability of accurately locating the sonic line by this method is therefore greatly decreased, as only an integrated effect is measured by the pressure taps.

In Fig. 59, the static to total pressure ratio obtained analytically is compared with that obtained experimentally. The comparison is made both at the wall and on the centerline. While the experimental data is subject to the smearing effect, noted earlier, a valid comparison between the two curves is possible. Small scale deviations from the general curve cannot be expected to be evident in the experimental curve, however magnitudes and trends may be compared. Such a comparison reveals an acceptably high degree of agreement between experimental and analytic results. Further agreement might result from further refinement of the compressibility function and further refinement of the experimental apparatus and technique.

CONCLUSIONS AND RECOMMENDATIONS

The analytical solution presented was found to accurately predict truncated plug nozzle flow fields (including the base pressure) over the range of nozzle configurations and overall pressure ratios studied. The Hartree Technique used with the method of characteristics appeared to give very good results for the calculation of the inviscid part of the nozzle flow field. This conclusion was verified by a substantial amount of experimental data.

The introduction of the overexpansion process at the shroud exit enabled the solution to detect the internal shock wave in the region where it develops in the actual flow. It was shown that the amount of overexpansion had very little effect on the downstream development of the shock wave, and therefore an optimum value could be used for all cases. This eliminated the need for empirical data for each case. The shock wave location was accurately determined for all cases investigated.

The base pressure solution developed by Zumwalt and later modified by Mueller produced good agreement with experiment, and correctly predicted the variation in base pressure with plug truncation and area ratio. It was also found that for the configurations studied, the base pressure solution was relatively insensitive to changes in the wake radius ratio, and therefore a constant value could be used with confidence. For the cases studied, $L/L_{max} \approx 0.50$ represented the upper limit for the validity of the base pressure solution.

The base pressure results were greatly improved by the inclusion of the internal shock wave in the overall solution. The error in the base pressure was less than half of that obtained with the no-shock solution. It was further demonstrated that, in order to achieve this improvement, it is essential to have the internal shock originate near the shroud exit. If the overexpansion technique introduced (or a similar technique) is not used, the shock will originate downstream of the plug base where it cannot influence the base pressure.

Detailed optical investigations of the nozzle flow fields produced excellent results. The shadowgraph photographs provided quantitative data, as well as qualitative insight into the basic flow field characteristics. These photographs also delineated the reflection mechanism of the internal shock wave and in particular the Mach disc. The Mach disc in T-P nozzle flows exhibited the same general characteristics as those in C-D nozzle flowfields. It was also found from these and subsequent experiments that the lip shock was very weak and could be excluded from the analytical flow model.

A limited number of nozzle-diffuser experiments indicated that the long second throat diffuser had no effect on the nozzle base pressure during "closed wake" operation.

The static pressure ratios along the nozzle centerline produced a trend for the "open wake" case which was somewhat similar to that for the "closed wake". In particular, this similarity included a rising pressure or recompression region which appeared to be more complicated than for the "closed wake" case.

Analytical studies showed that variations in the ratio of specific heats had a significant effect on both the internal shock location and the base pressure ratio. These effects were large enough that they could not be neglected for calculations on nozzles using gases other than air.

A new method of calculating the flow field including the sonic line in the transonic region was successful. The results appeared to be reasonable when compared with those of other investigators and a very limited amount of experimental data.

Although the analytical solution of the nozzle flow produced very good results, more theoretical and experimental work could be performed in order to improve the theoretical predictions over a wider range of parameters. This analytical procedure should be extended to include cases where the T-P nozzle is exhausting into a moving airstream. The interaction of the nozzle flow and the freestream could effect the altitude compensation properties of these nozzles. The transonic solution procedure should be applied to as wide a range of throat radii of curvatures as possible and the results compared with appropriate experimental data.

Additional experiments could be performed to study the impingement of the nozzle flow on a surface of varying distance from the nozzle. Data of this type would be helpful in evaluating the nozzle performance during blast-off or powered planetary landings. The nozzle-diffuser interactions should also be studied in more detail.

APPENDIX I

REAL GAS EFFECTS

In adapting computer programs to include real gas effects two alternatives are available. The first is a tabular search for the gas properties at a particular temperature and pressure. The second alternative involves actually calculating the properties of the gas at each point (Ref. 36). In both methods arrays of three new variables must be saved at each characteristic point. These are the static temperature, the static pressure, and the ratio of specific heats. Both of these techniques will be discussed.

Tabulation of Gas properties

At each point in the programs where the ratio of specific heats, γ, appears, the computer must search the table of gas properties for the value of the ratio of specific heats corresponding to the static temperature, static pressure, and Mach number at this position. In the method of characteristics solution, for example, the value of the ratio of specific heats must be iterated along with the streamline angle and Prandtl-Meyer angle. Also the Prandtl-Meyer angle is a function of both the Mach number and the ratio of specific heats. The base pressure solution also would depend on the ratio of specific heats. The Crocco number which is used extensively in this solution is a strong function of both Mach number and ratio of specific heats. Each equation in Ref. 21 which is used in the solution must be evaluated using the local value of the ratio of specific heats.

Calculation of Gas Properties

Again at each point in the program where the ratio of specific heats appear, the following calculations (or something similar) must be made to evaluate the ratio of specific heats. The following procedure taken from Reference 1 is applicable over a very wide temperature and pressure range, but this analysis is limited to diatomic gases such as hydrogen and oxygen. This analysis treats isentropic flows by combining the Van der Wall equation of state with quantum mechanical considerations. The calculation procedure outlined below would be applicable to a method of characteristics solution in which the Mach number was specified.

1. Evaluate the constant θ associated with the particular gas. (This constant may also be determined from spectroscopic data.)

$$\theta = \frac{h\nu}{k}$$

2. Make an initial estimate of the static temperature. This may be just the average of the temperatures at the two upstream points in the characteristics solution.

3. Evaluate the specific volume, v:

$$v = b + (v_0 - b)\left(\frac{T_0}{T}\right)^{5/2}\left[\frac{1-e^{\theta/T}}{1-e^{\theta/T_0}}\right]e^{\left(\frac{\theta}{T_0}\frac{e^{\theta/T_0}}{e^{\theta/T_0-1}} - \frac{\theta}{T}\frac{e^{\theta/T}}{e^{\theta/T-1}}\right)}$$

4. Since the Mach number has been specified, the following equation is solved for the static temperature such that the Mach number which is calculated corresponds to the specified Mach number.

$$M^2 = \frac{5\mathcal{R}(T_0-T) + \frac{2\mathcal{R}\theta}{e^{\theta/T_0-1}} - \frac{2\mathcal{R}\theta}{e^{\theta/T-1}} + 2v_0\left(\frac{\mathcal{R}T_0}{v_0-b} - \frac{2a}{v_0^2}\right) - 2v\left(\frac{\mathcal{R}T}{v-b} - \frac{2a}{v^2}\right)}{\left|1 + \frac{1}{\frac{5}{2} + \left(\frac{\theta}{T}\right)^2\frac{e^{\theta/T}}{(e^{\theta/T-1})^2}}\right|\frac{v^2\mathcal{R}T}{(v-b)^2} - \frac{2a}{v}}$$

5. Repeat steps 3 and 4 until convergence on a static temperature has been reached.

6. Calculate P/P_0 and solve for the static pressure P:

$$\frac{P}{P_0} = \frac{\frac{\mathcal{R}T}{v-b} - \frac{a}{v^2}}{\frac{\mathcal{R}T_0}{v_0-b} - \frac{a}{v_0^2}}$$

7. Evaluate the ratio of specific heats:

$$\gamma = \frac{\frac{5}{2} + \left(\frac{\theta}{T}\right)^2\frac{e^{\theta/T}}{(e^{\theta/T-1})^2}\quad\frac{Pv^2+a}{Pv^2-a+\frac{2ab}{v}}}{\frac{5}{2} + \left(\frac{\theta}{T}\right)^2\frac{e^{\theta/T}}{(e^{\theta/T-1})^2}}$$

In the base pressure solution velocity ratios are used in conjunction with Mach numbers. Therefore to determine the actual velocity, the speed of sound must be calculated:

$$C^2 = \left[1 + \frac{1}{\frac{5}{2} + \left(\frac{\theta}{T}\right)^2\frac{e^{\theta/T}}{(e^{\theta/T-1})^2}}\right]\frac{v^2\mathcal{R}T}{(v-b)^2} - \frac{2a}{v}$$

For other calculations, not involving the method of characteristics solutions, the iteration procedure must be modified depending on what variables are known.

REFERENCES

1. Connors, J. F., Cubbison, R. W. and Mitchell, G. A.: "Annular Internal-External-Expansion Rocket Nozzles for Large Booster Applications," NASA TN D-1049, September, 1961.

2. Wasko, R. A.: "Performance of Annular Plug and Expansion-Deflection Nozzles Including External Flow Effects at Transonic Mach Numbers," NASA TN D-4462, April, 1968.

3. Migdal, D. and Horgan, J. J.: "Thrust Nozzles for Supersonic Transport Aircraft," ASME J. Eng. Power, April 1964, pp. 97-104.

4. Mueller, T. J. and Sule, W. P.: "Condensation and Probe Interference Effects on Planar Expansion-Deflection Nozzle Experiments," Journal of Spacecraft and Rockets, Vol. 6, No. 7, July, 1969, pp. 857-859.

5. Beheim, M. A. and Boksenbom, A. S.: "Variable Geometry Requirements in Inlets and Exhaust Nozzles for High Mach Number Applications," NASA TM X-52447, 1968.

6. Valerino, A. S., Zappa, R. F. and Abdalla, K. L.: "Effects of External Stream on the Performance of Isentropic Plug-Type Nozzles at Mach Numbers of 2.0, 1.8, and 1.5," NASA 2-17-59E, March, 1959.

7. Herd, R. J. and Golesworthy, G. T.: "The Performance of a Centerbody Propelling Nozzle with a Parallel Shroud in External Flow," Aeronautical Research Council, Current Papers No. 841, 1966.

8. Berrier, B.L. and Mercer, C. E.: "Off-Design Performance of Two Isentropic Plug Nozzles Designed for a Pressure Ratio of 16.5," NASA TN D-3852, March, 1967.

9. Casci, C., Gismondi, E. and Angelino, G.: "An Experimental Study on the Application of Plug Nozzles to Solid-Propellent Rockets - 1," Spaceflight, Vol. 9 No. 12, December, 1967, pp. 429-432.

10. Smolak, G. R. and Koffel, W. K.: "Investigation of an Air-Cooled, Plug-Type, Variable-Area Exhaust Nozzle," NACA RM E57A07, April 10, 1957.

11. Gaede, A. E. and Lopez, H. J.: "Selection of Nozzle Contours for a Research Scramjet Engine," AIAA Paper No. 67-453, presented at the AIAA 3rd Propulsion Joint Specialist Conference, Washington, D.C., July 17-21, 1967.

12. Burlage, H., Jr. and Dipprey, D. F.: "Liquid Rockets for Advanced Missions," Report AFOSR 69-2951TR, Proceedings of the Fifth AFOSR Symposium on Advanced Propulsion Concepts, Chicago, Ill., April, 1968.

13. Martinez, A.: "Advanced Nozzle Study," Final Report R-6582, Rocketdyne, Canoga Park, Calif., July 15, 1966.

14. Taylor, D. and Toline, F. R.: "Summary of Exhaust Gas Ejector-Diffuser Research," AEDC-TR-68-84, Arnold Engineering Development Center, Arnold Air Force Station, Tennessee, October, 1968.

15. Mueller, T. J., Sule, W. P., and Hall, C. R., Jr.: "Characteristics of Separated Flow Regions within Altitude Compensating Nozzles". University of Notre Dame Report UNDAS TN-029-PR-9, Jan. 1971.

16. Hama, F. R.: "Experimental Investigations of Wedge Base Pressure and Lip Shock," Technical Report 32-1033, Jet Propulsion Laboratory, California Institute of Technology, Pasadena, California, December, 1966.

17. Sieling, W. R.: "The Effect of Sting Diameter and Length on Base Pressure at M=3.88". The Aeronautical Quarterly, Vol. 19, 1968, pp. 368-374.

18. Sieling, W. R. and Page, R. H.: "A Re-examination of Sting Interference Effects". AIAA Paper No. 70-585, May 1970.

19. Peters, C. E.: "Some Studies of Mach Disc Formation for Moderately Underexpanded Supersonic Nozzles," Ph. D. Dissertation, University of Brussels, March, 1968.

20. Hall, C. R., Jr.: "An Analytical and Experimental Study of Non-Uniform Plug Nozzle Flow Fields," Ph. D. Dissertation, Department of Aerospace/Mechanical Engineering, University of Notre Dame, Notre Dame, Ind., August, 1970.

21. Hall, C. R., Jr. and Mueller, T. J.: "Exploratory Analysis of Nonuniform Plug Nozzle Flowfields". Journal of Spacecraft and Rockets, Vol. 9, No. 5, May 1972, pp. 337-342.

22. Weiss, R. F. and Weinbaum, S.: "Hypersonic Boundary Layer Separation and the Base Flow Problem," Research Report 221, Avco-Everett Research Laboratories, Everett, Massachusetts, July, 1965.

23. Zumwalt, G. W.: "Analytical and Experimental Study of the Axially-Symmetric Supersonic Base Pressure Problem," Ph. D. Dissertation, Department of Mechanical Engineering, University of Illinois, Urbana, Illinois, 1959, (MIC 59-4589, University Microfilms, Inc., Ann Arbor, Michigan).

24. Mueller, T. J.: "Determination of the Turbulent Base Pressure in Supersonic Axisymmetric Flow," Journal of Spacecraft and Rockets, Vol. 5, No. 1, January, 1968.

25. Mueller, T. J. and Hall, C. R., Jr.: "Annalytical Prediction of the Turbulent Base Pressure in Supersonic Axisymmetric Flow Including the Effect of Initial Flow Direction," AFFDL-TR-68-132, Air Force Flight Dynamics Laboratory, Air Force Systems Command, Wright-Patterson Air Force Base, Ohio, September, 1968.

26. Hartree, D. R.: "Numerical Analysis," Oxford University Press, London, 2nd ed., Chap. X, pp. 257-263.

27. Chou, P. C., Karpp, R. R. and Huang, S. L.: "Numerical Calculation of Blast Waves by the Method of Characteristics," AIAA Journal, Vol. 5, No. 4, April, 1967, pp. 618-623.

28. Boynton, Frederick, P.: "Exhaust Plumes from Nozzles with Wall Boundary Layers," Journal of Spacecraft and Rockets, Vol. 5, No. 10, October, 1968, pp. 1143-1147.

29. Zumwalt, G. W. and Tang, H. H.: "Transient Base Pressure Study of an Axisymmetric Missile Flying Head-On Through a Blast Wave," Research Report SBW-6, School of Mechanical Engineering, Oklahoma State University, February, 1964.

30. Channapragada, R. S.: "Compressible Jet Spread Parameter for Mixing Zone Analyses," AIAA Journal, Technical Note, Vol. 1, No. 9, September, 1963, pp. 2188-2190.

31. Garabedian, P. R.: "Partial Differential Equations," John Wiley and Sons, Inc., New York, London, Sydney, 1964, pp. 520-521.

32. Ferrari, C., and Tricomi, F. G.: "Transonic Aerodynamics," Academic Press, New York and London, 1968, p. 180.

33. Moon, P., and Spencer, D. E.: "Field Theory Handbook," Springer-Verlag, Berlin, Gottingen, Heidelberg, 1961, p. 53.

34. Duff, G. F. D., and Naylor, D.: "Differential Equations of Applied Mathematics," John Wiley and Sons, Inc., New York, London, Sydney, 1966, p. 282.

35. Serra, R. A.: "Determination of Internal Gas Flows by a Transient Numerical Technique," AIAA Journal, Vol. 10, No. 5, May 1972, pp. 603-611.

36. Coleman, du P. Donaldson: "Note on the Importance of Imperfect Gas Effects and Variation of Heat Capacities on the Isentropic Flow of Gases," NACA RM No. L8J14, December 10, 1948.

TABLE I

Axisymmetric Truncated Plug Nozzle Model ATP1

Overall Area Ratio, $A_{ne}/A_{nt} = 1.555$

Design Mach Number, $M_e = 1.90$

Throat Area, $A_{nt} = 0.330$ in.^{2} (2.129 cm^2)

Shroud Radius, $r_{sh} = 0.405$ in. (1.028 cm)

Shroud Length from Throat, $L_{sh} = 0.300$ in. (0.762 cm),

$L_{sh}/r_{sh} = 0.742$

Plug Angle, $\alpha = 10^o$

Maximum Plug Length, $L_{max} = 1.374$ in. (3.489 cm)

Plug Dimensions, inches (centimeters)

Length Ratio, L/L_{max}	Length from Throat, L, in (cm)	Base Radius, r_b, in (cm)
0.2184	0.300 (0.762)	0.188 (0.477)
0.2766	0.380 (0.965)	0.174 (0.442)
0.3275	0.450 (1.143)	0.162 (0.411)
0.3785	0.520 (1.320)	0.150 (0.381)
0.4290	0.590 (1.499)	0.137 (0.348)
0.4802	0.660 (1.676)	0.125 (0.317)

TABLE II

Axisymmetric Truncated Plug Nozzle Model ATP2

Overall Area Ratio, $A_{ne}/A_{nt} = 1.684$

Design Mach Number, $M_e = 2.00$

Throat Area, $A_{nt} = 0.602$ in.^{2} (3.884 cm^2)

Shroud Radius, $r_{s_h} = 0.568$ in. (1.443 cm)

Shroud Length from Throat, $L_{s_h} = 0.300$ in. (0.762 cm),

$L_{s_h}/r_{s_h} = 0.528$

Plug Angle, $\alpha = 10^o$

Maximum Plug Length, $L_{max} = 2.070$ in. (5.258 cm)

Plug Dimensions, inches (centimeters)

Length Ratio, L/L_{max}	Length from Throat, L, in (cm)	Base Radius, r_b, in (cm)
0.1449	0.300 (0.762)	0.312 (0.792)
0.2327	0.482 (1.224)	0.280 (0.711)
0.2766	0.573 (1.455)	0.260 (0.660)
0.3275	0.678 (1.722)	0.245 (0.622)
0.3785	0.783 (1.989)	0.227 (0.576)

TABLE III

Wall Contour Pressure Tap Locations
for Planar Transonic Nozzle (PLTR1)

Dimensions, inches (centimeters)

Group C - on y = 0

TAP	x-LOCATION		z-LOCATION	
C1	-1.000	(-2.540)	0.000	(0.000)
C2	-0.800	(-2.032)	+0.375	(0.952)
C3	-0.600	(-1.524)	0.000	(0.000)
C4	-0.500	(-1.270)	-0.375	(-0.952)
C5	-0.400	(-1.016)	0.000	(0.000)
C6	-0.300	(-0.762)	+0.375	(0.952)
C7	-0.250	(-0.635)	0.000	(0.000)
C8	-0.200	(-0.508)	-0.375	(-0.952)
C9	-0.150	(-0.381)	0.000	(0.000)
C10	-0.100	(-0.254)	+0.375	(0.952)
C11	-0.050	(-0.127)	0.000	(0.000)
C12	-0.000	(0.000)	-0.375	(-0.952)
C13	+0.050	(0.127)	0.000	(0.000)
C14	+0.100	(0.254)	+0.375	(0.952)
C15	+0.150	(0.381)	0.000	(0.000)
C16	0.200	(0.508)	-0.375	(-0.952)
C17	0.250	(0.635)	0.000	(0.000)
C18	0.300	(0.762)	+0.375	(0.952)
C19	0.400	(1.016)	0.000	(0.000)
C20	0.500	(1.270)	-0.375	(-0.952)
C21	0.600	(1.524)	0.000	(0.000)
C22	0.800	(2.032)	+0.375	(0.952)
C23	0.950	(2.286)	0.000	(0.000)

TABLE IV

Sideplate Pressure Tap Locations
for Planar Transonic Nozzle (PLTR1)

Dimensions, inches (centimeters)

Group S - on y = 0

TAP	x-LOCATION		TAP	x-LOCATION	
S1	-1.000	(-2.540)	S13	+0.050	(0.127)
S2	-0.800	(-2.032)	S14	+0.100	(0.254)
S3	-0.600	(-1.524)	S15	+0.150	(0.381)
S4	-0.500	(-1.270)	S16	+0.200	(0.508)
S5	-0.400	(-1.016)	S17	+0.250	(0.635)
S6	-0.300	(-0.762)	S18	+0.300	(0.762)
S7	-0.250	(-0.635)	S19	+0.400	(1.016)
S8	-0.200	(-0.508)	S20	+0.500	(1.270)
S9	-0.150	(-0.381)	S21	+0.600	(1.524)
S10	-0.100	(-0.254)	S22	+0.800	(2.032)
S11	-0.050	(-0.127)	S23	+0.950	(2.286)
S12	0.000	(0.000)			

Group T - on x = 0

TAP	y-LOCATION	
T1	-0.050	(-0.127)
T2	0.000	(0.000)
T3	+0.050	(+0.127)

Group B - at inflow station

TAP	x-LOCATION		y-LOCATION	
B1	-0.988	(-2.509)	-0.156	(-0.396)
B2	-0.995	(-2.527)	-0.104	(-0.264)
B3	-0.998	(-2.534)	-0.052	(-0.132)
B4	-1.000	(-2.540)	0.000	(0.000)
B5	-0.998	(-2.534)	+0.052	(0.132)
B6	-0.995	(-2.527)	+0.104	(0.264)
B7	-0.988	(-2.509)	+0.156	(0.396)

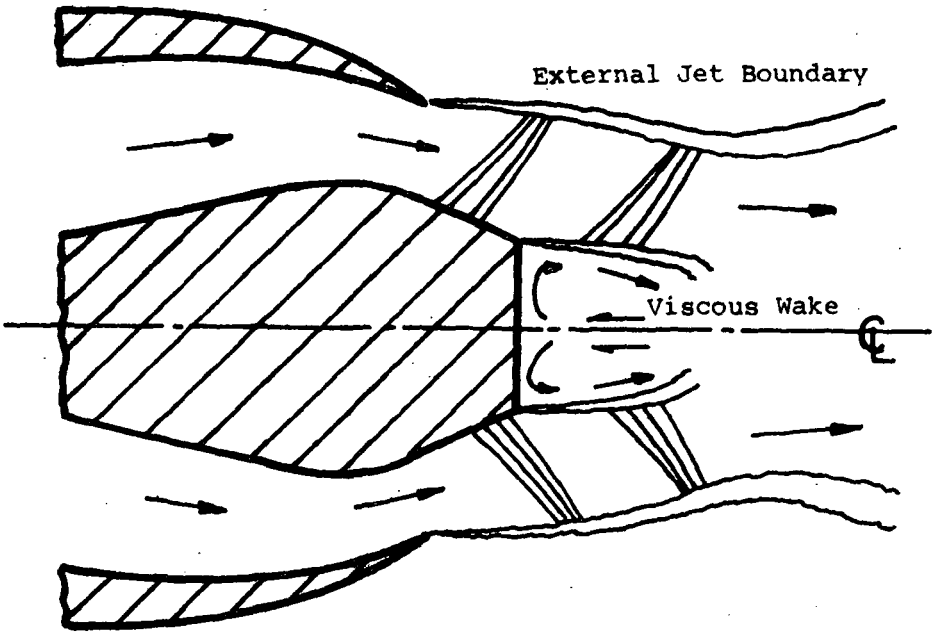

a.) Low Chamber to Ambient Pressure Ratio (i.e., "Open" Wake or Low Altitude Operation).

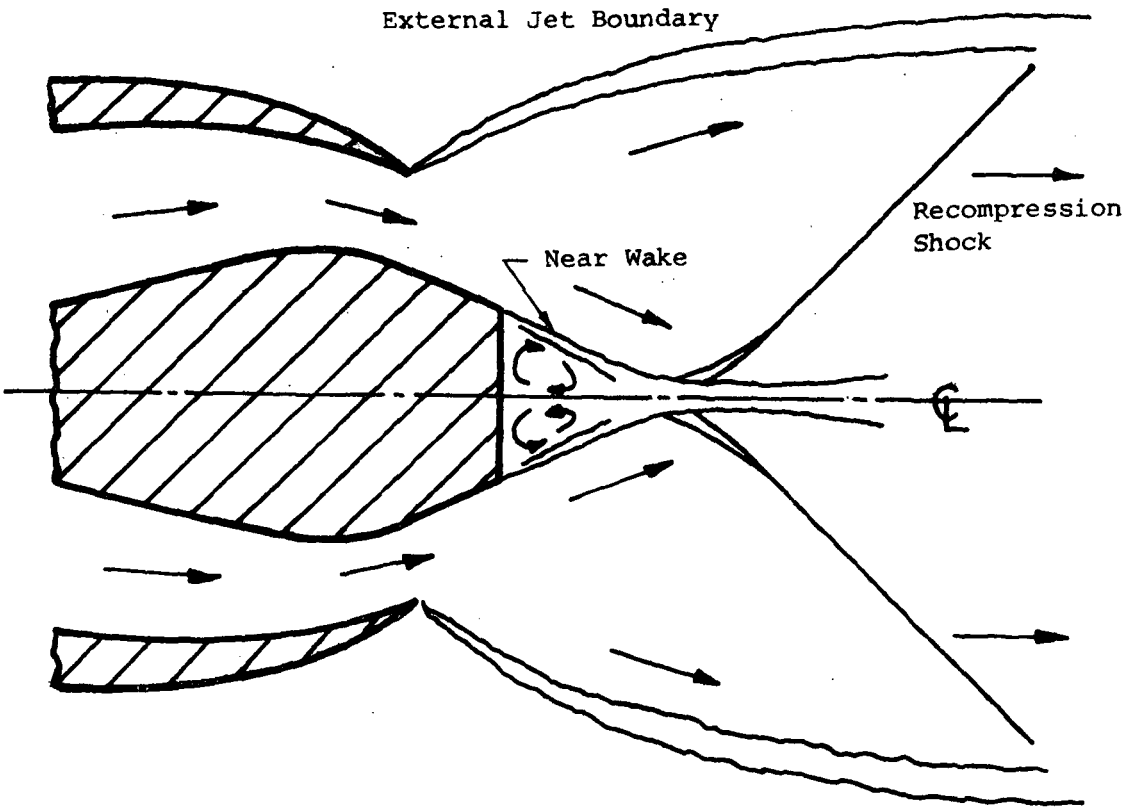

b.) High Chamber to Ambient Pressure Ratio (i.e., "Closed" Wake or High Altitude Operation).

Fig. 1 Essential Features of External Expansion Truncated Plug Nozzle Flow Fields for "open" and "closed" wake.

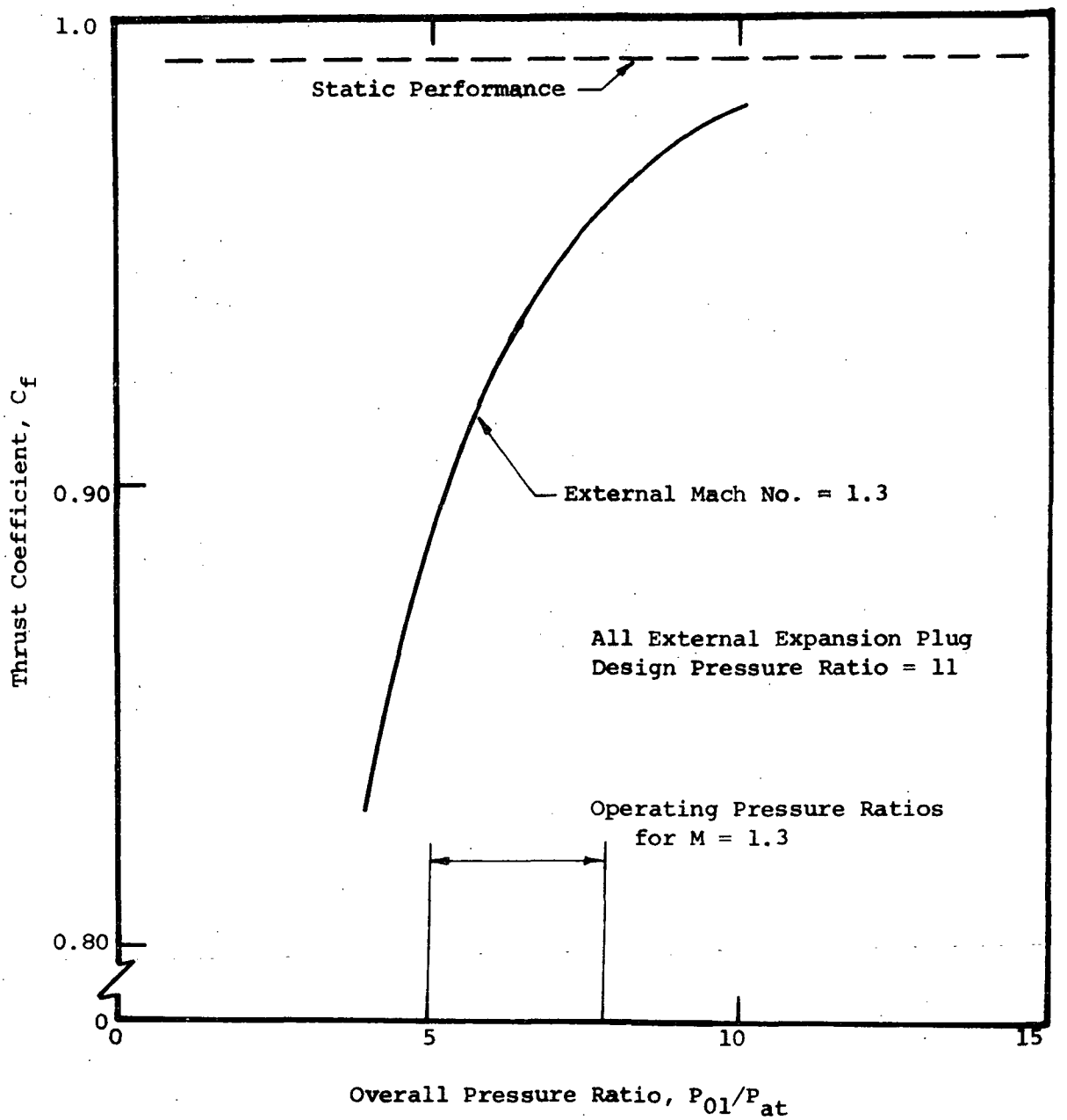

Fig. 2 External Flow Effect on Thrust Minus Drag for an All-External-Expansion Plug Nozzle (Ref. 3).

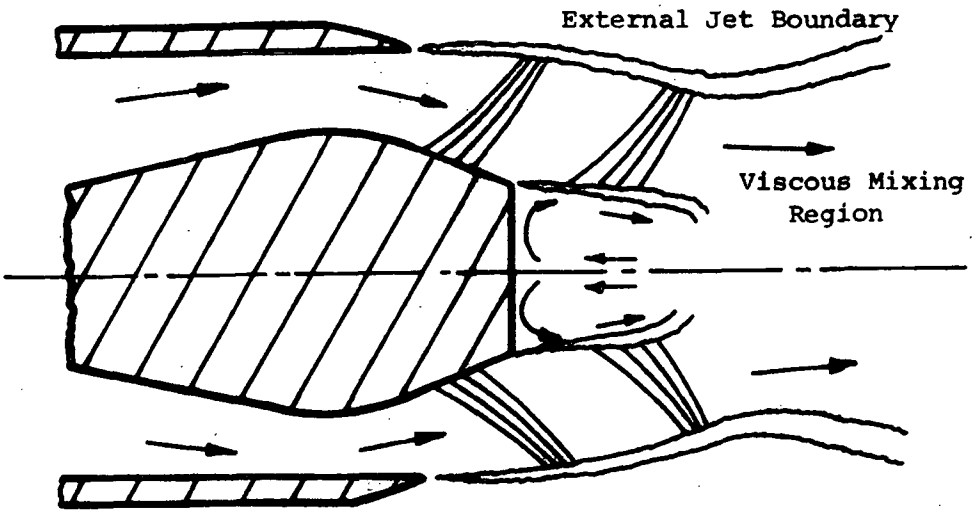

a. Low Altitude Operation, "Open Wake"

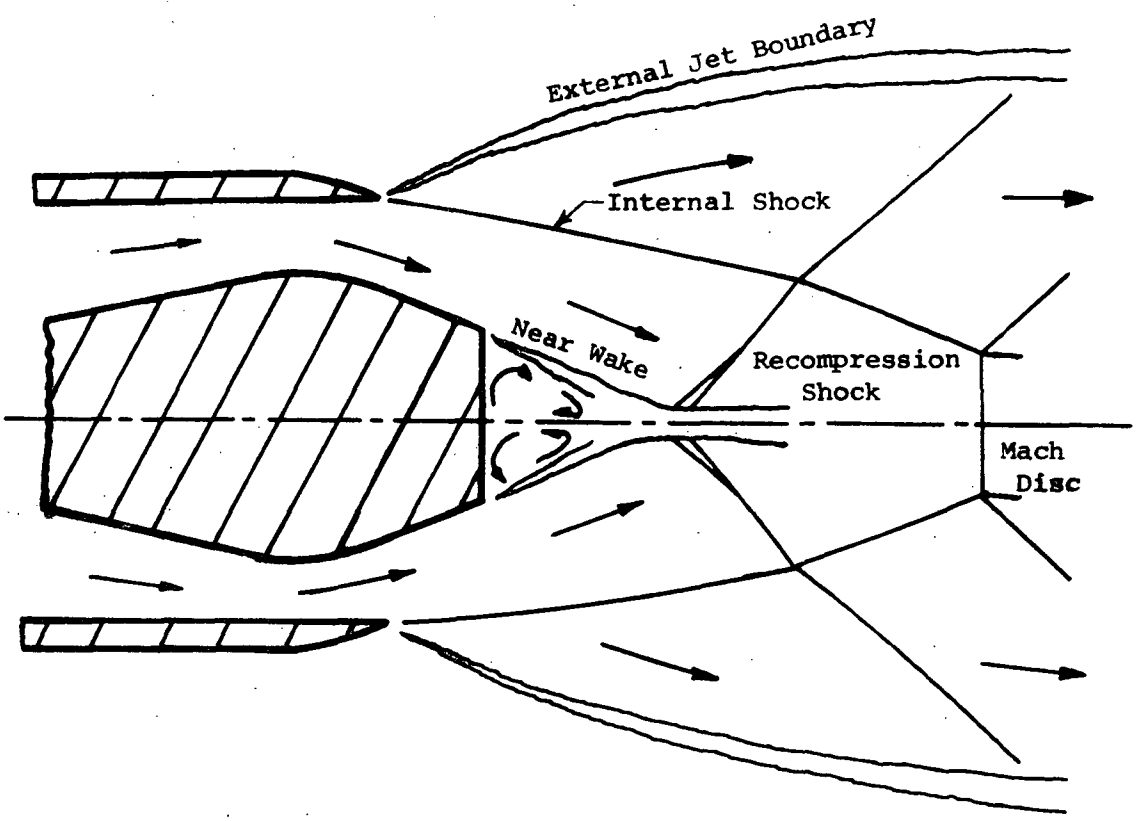

b. High Altitude Operation, "Closed Wake"

Fig. 3 Essential Features of Internal-External Expansion Axisymmetric Truncated Plug Nozzle Flow Fields.

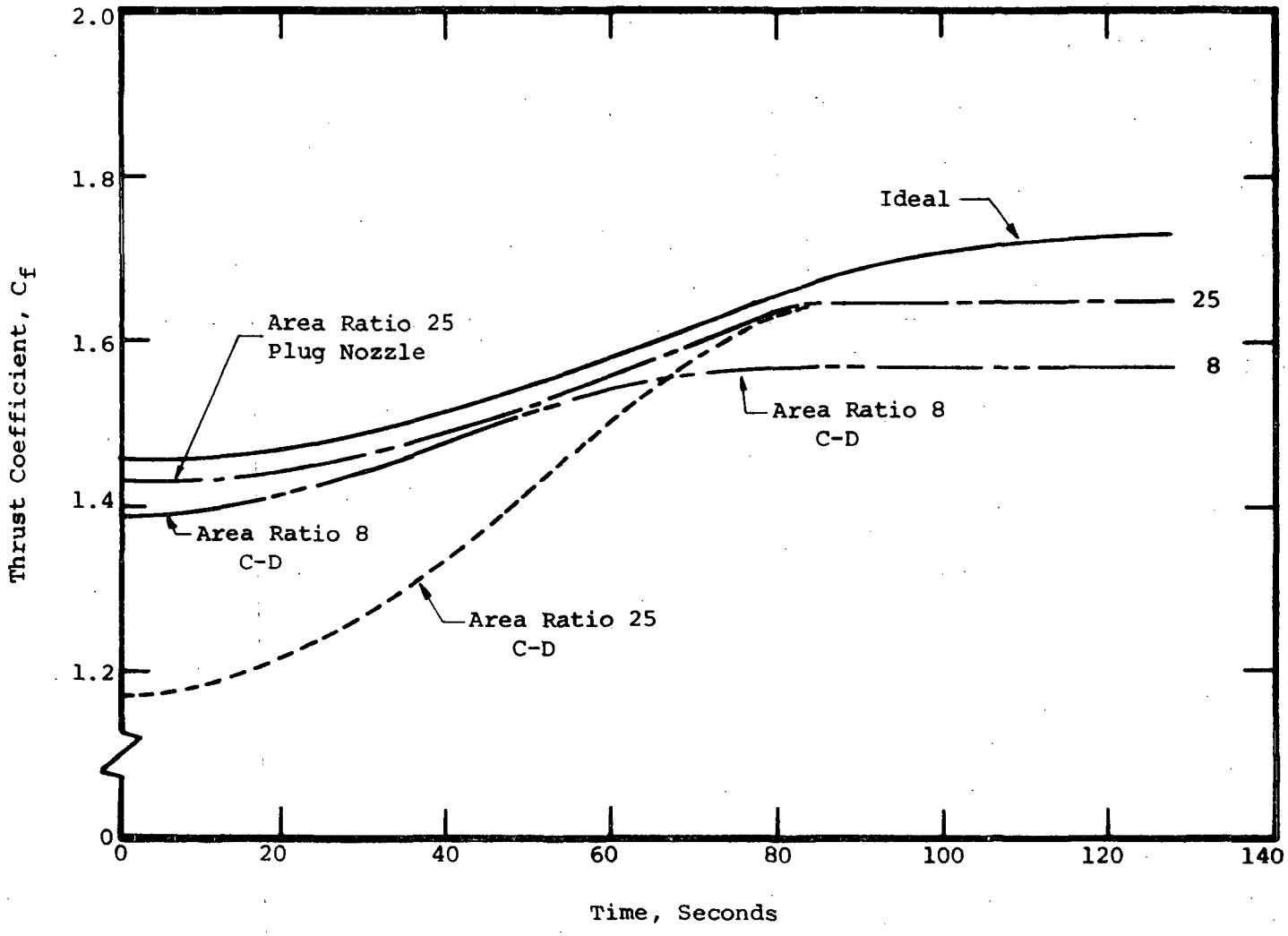

Fig. 4 Thrust Coefficient Comparison for Typical Boost Trajectory with Burnout at 167,000 feet (Ref. 1).

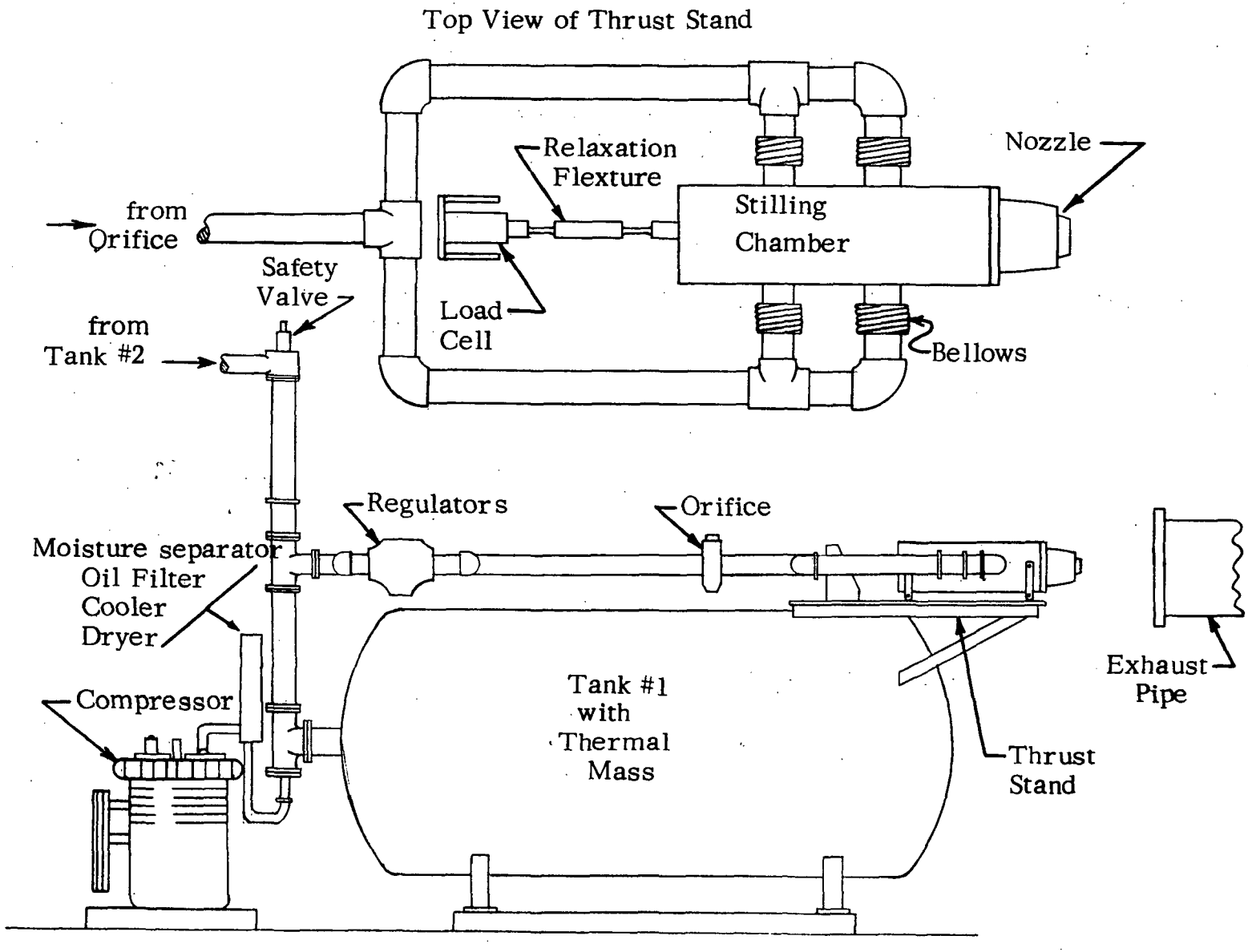

Fig. 5 Sketch of Nozzle Thrust Facility.

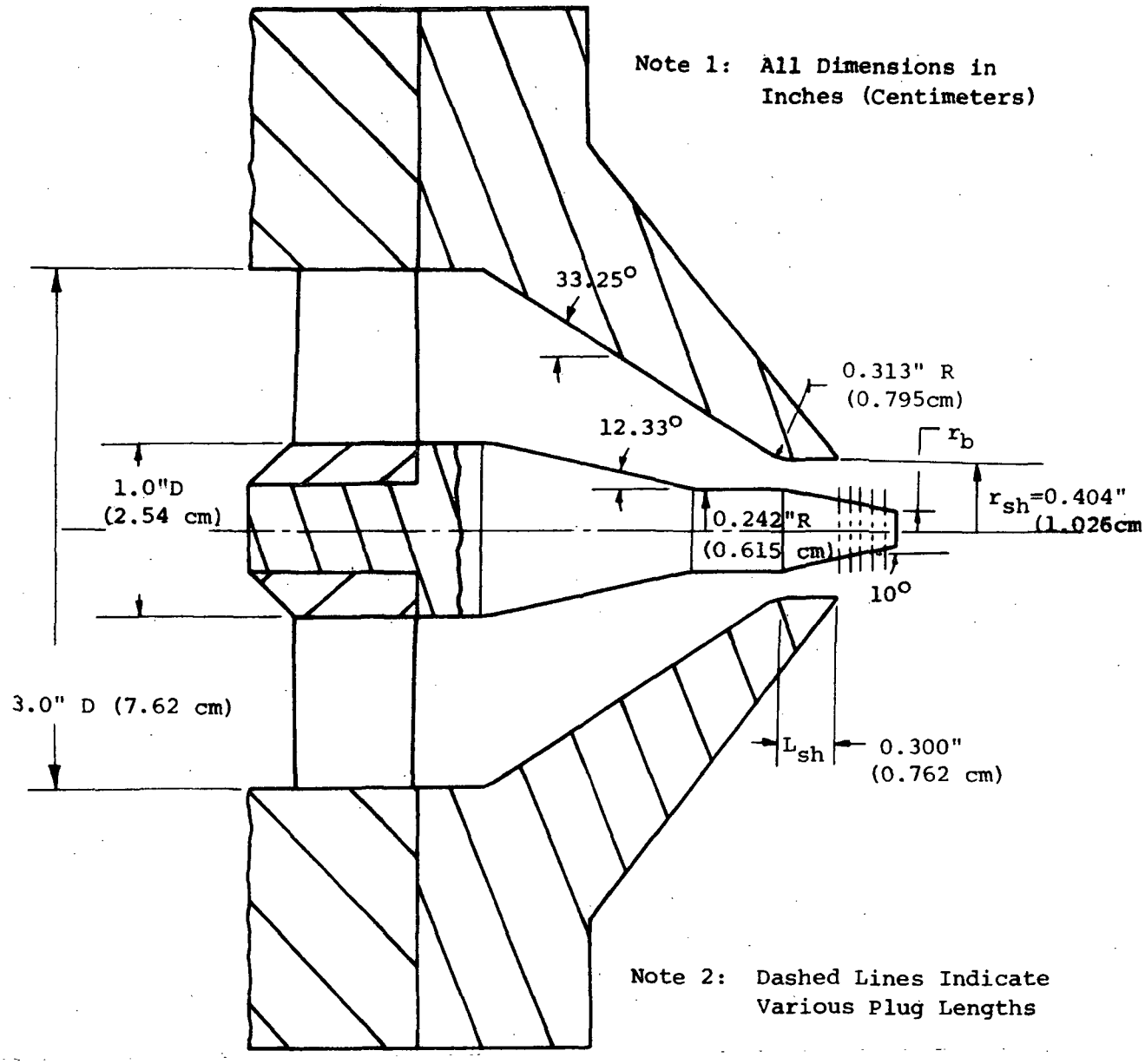

Fig. 6 Schematic of Axisymmetric Internal-External-Expansion Nozzle ATP1.

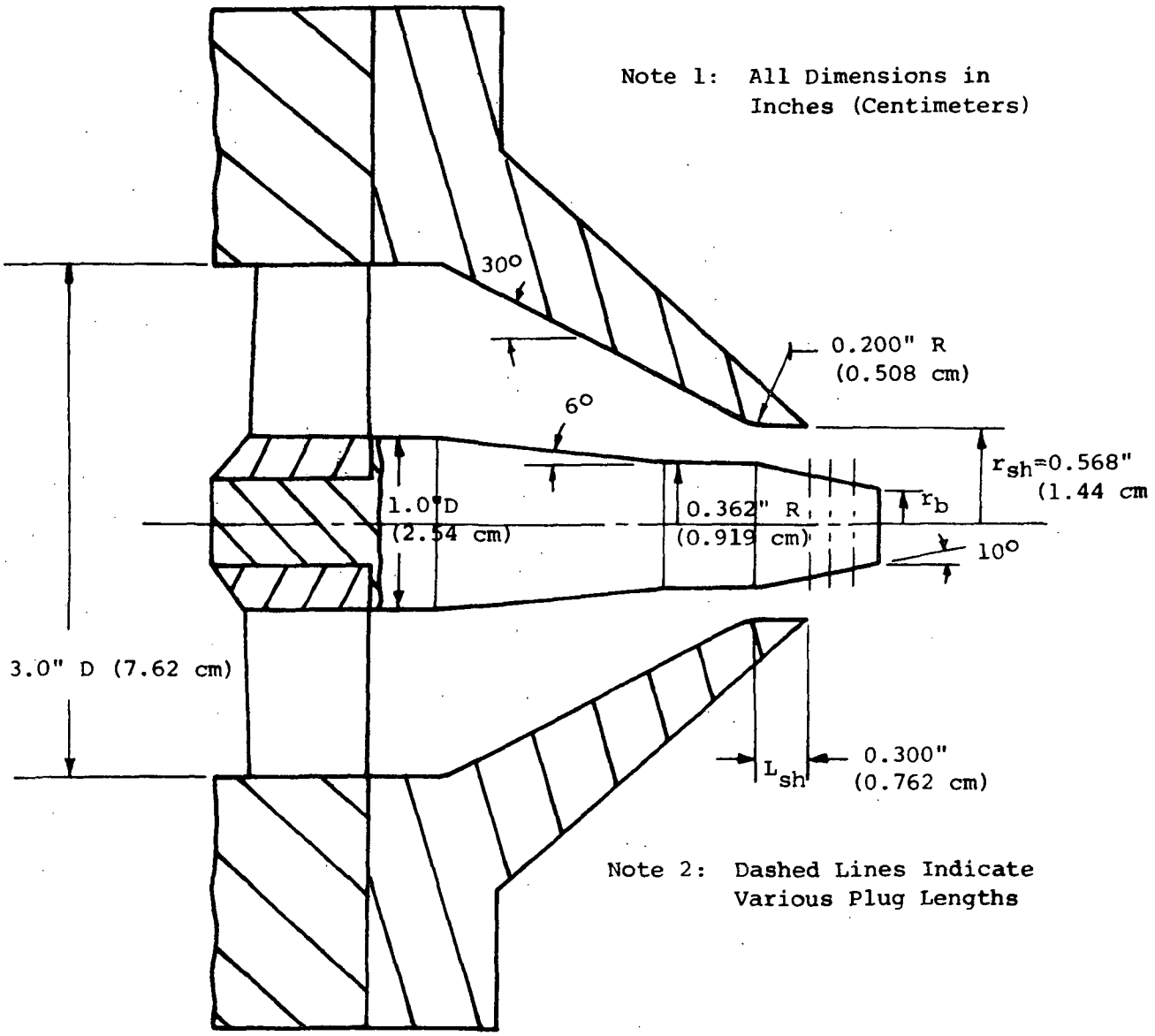

Fig. 7 Schematic of Axisymmetric Internal-Expansion Nozzle ATP2.

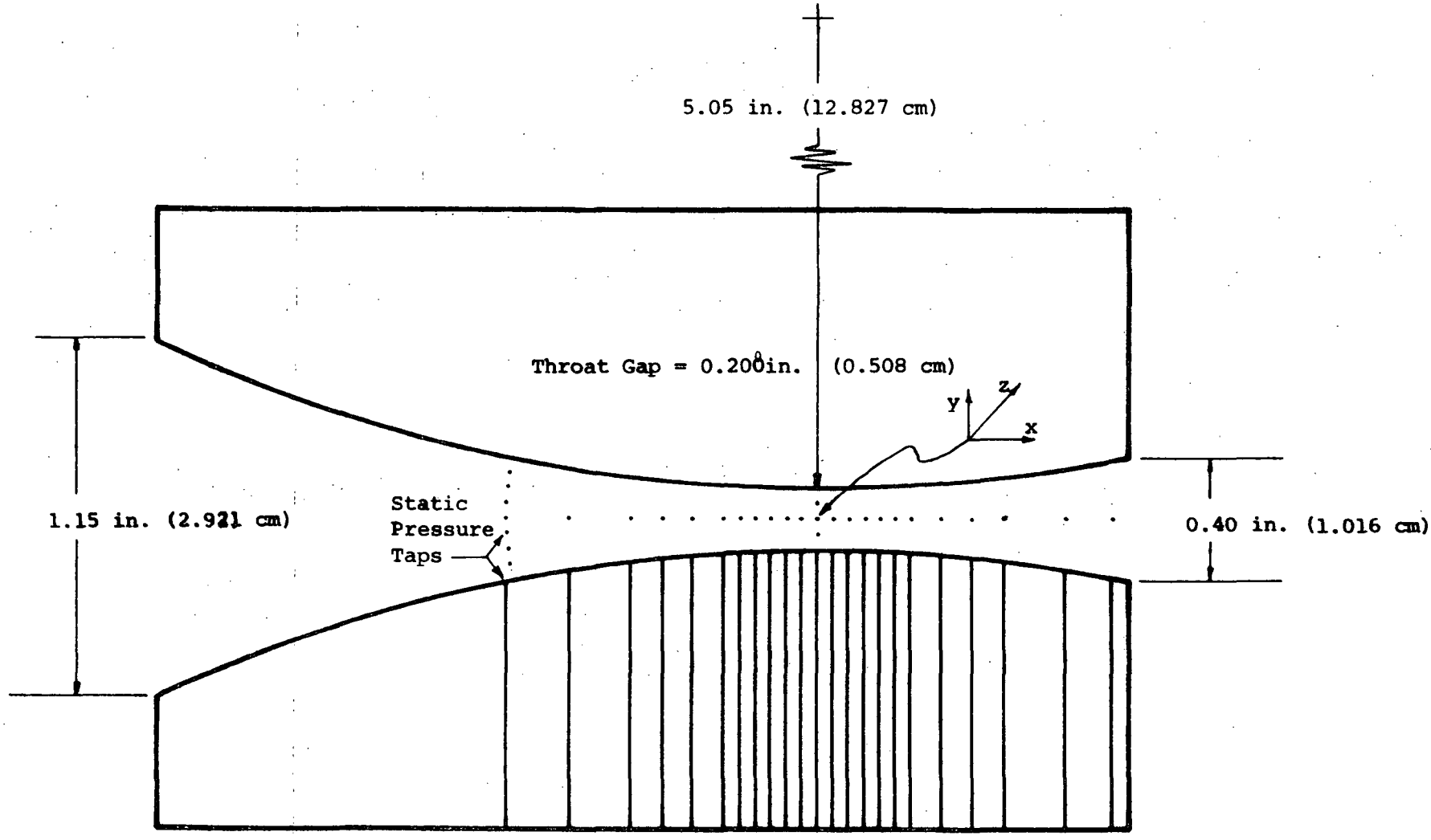

Fig. 8 Schematic of Planar Transonic Nozzle Section PLTR1.

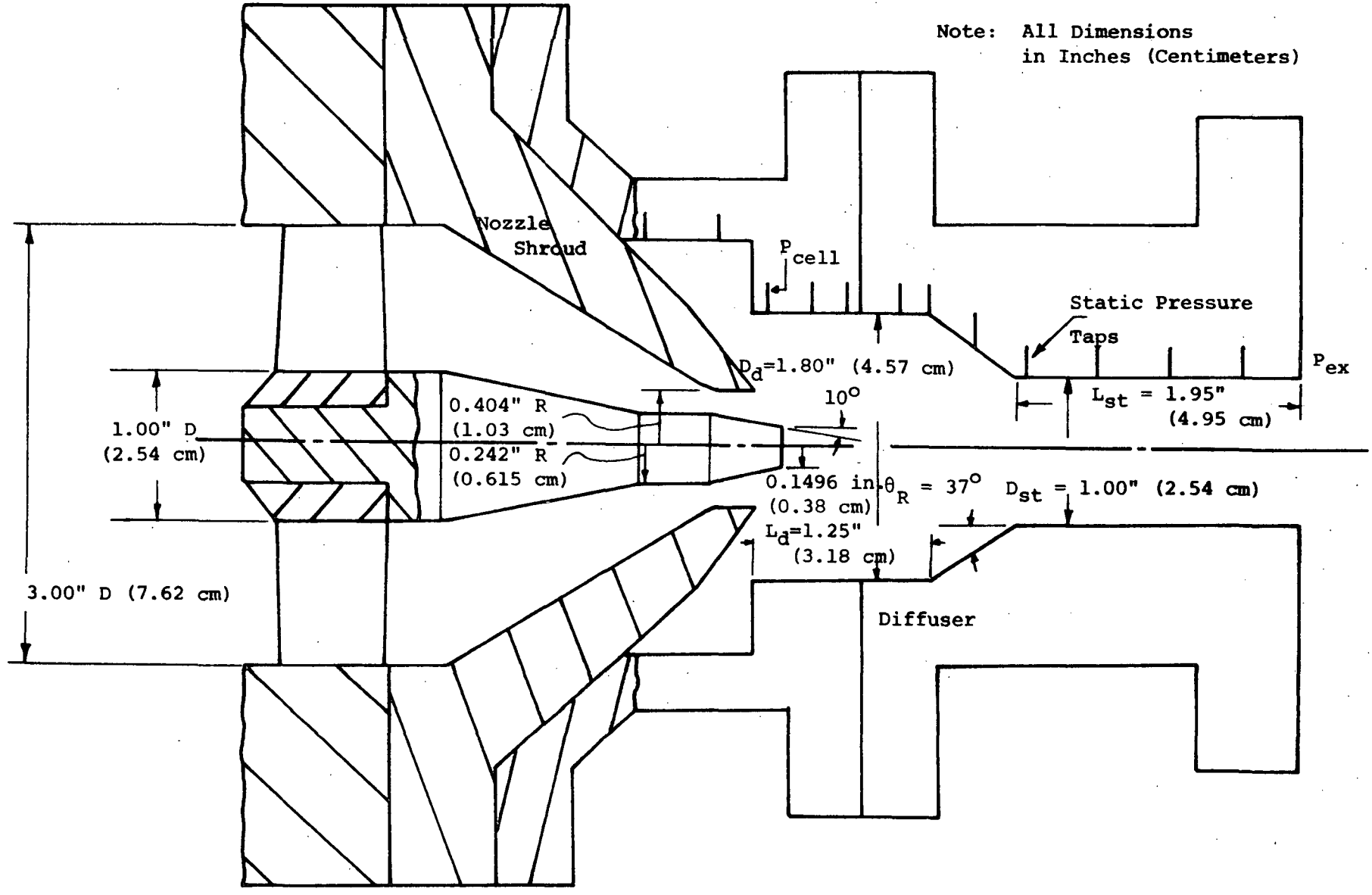

Fig. 9 Schematic of the Axisymmetric Truncated Plug Nozzle - Long Second Throat Diffuser Configuration.

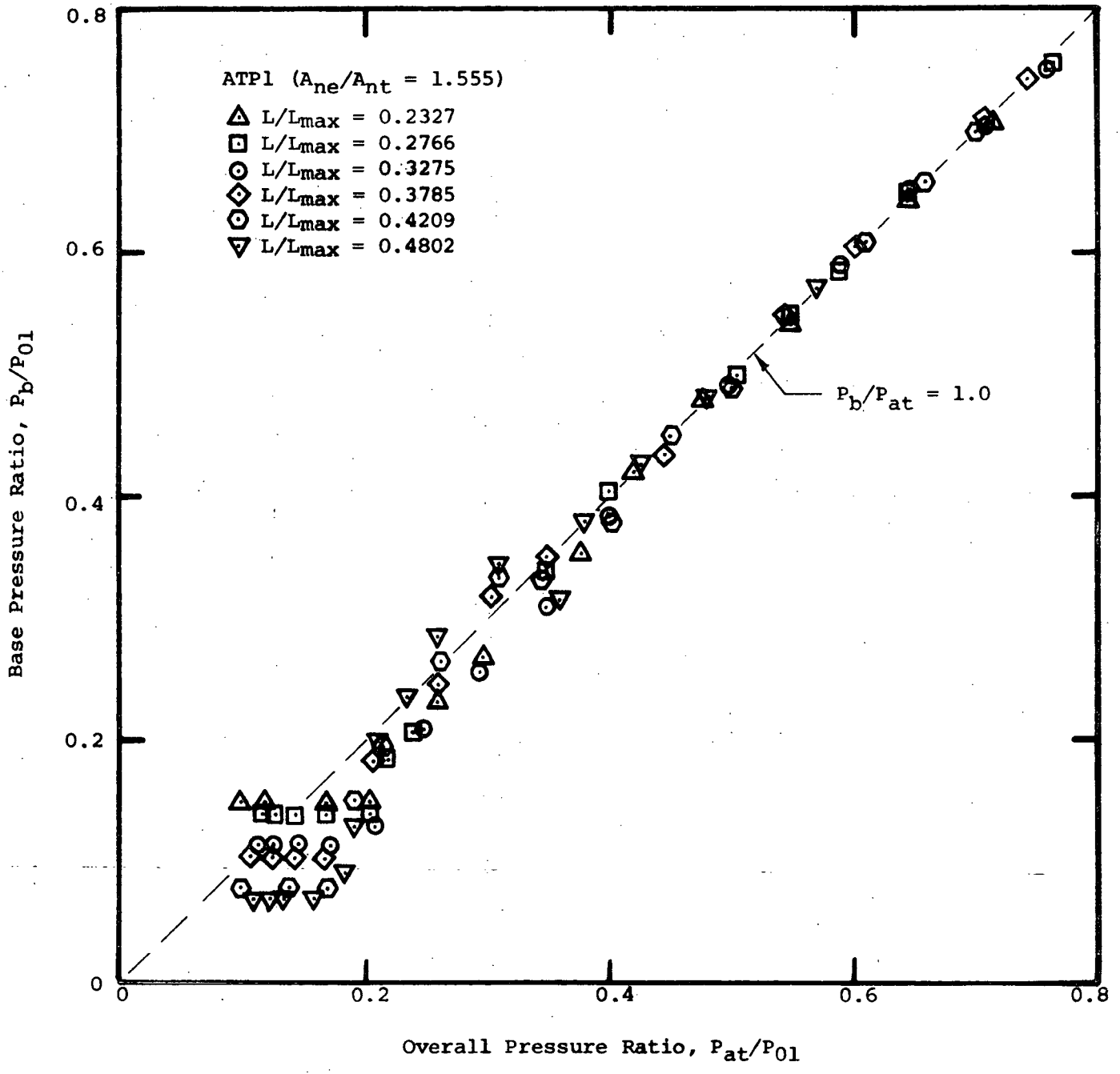

Fig. 10 Base Pressure Characteristics for Axisymmetric Truncated Plug Nozzle ATP1.

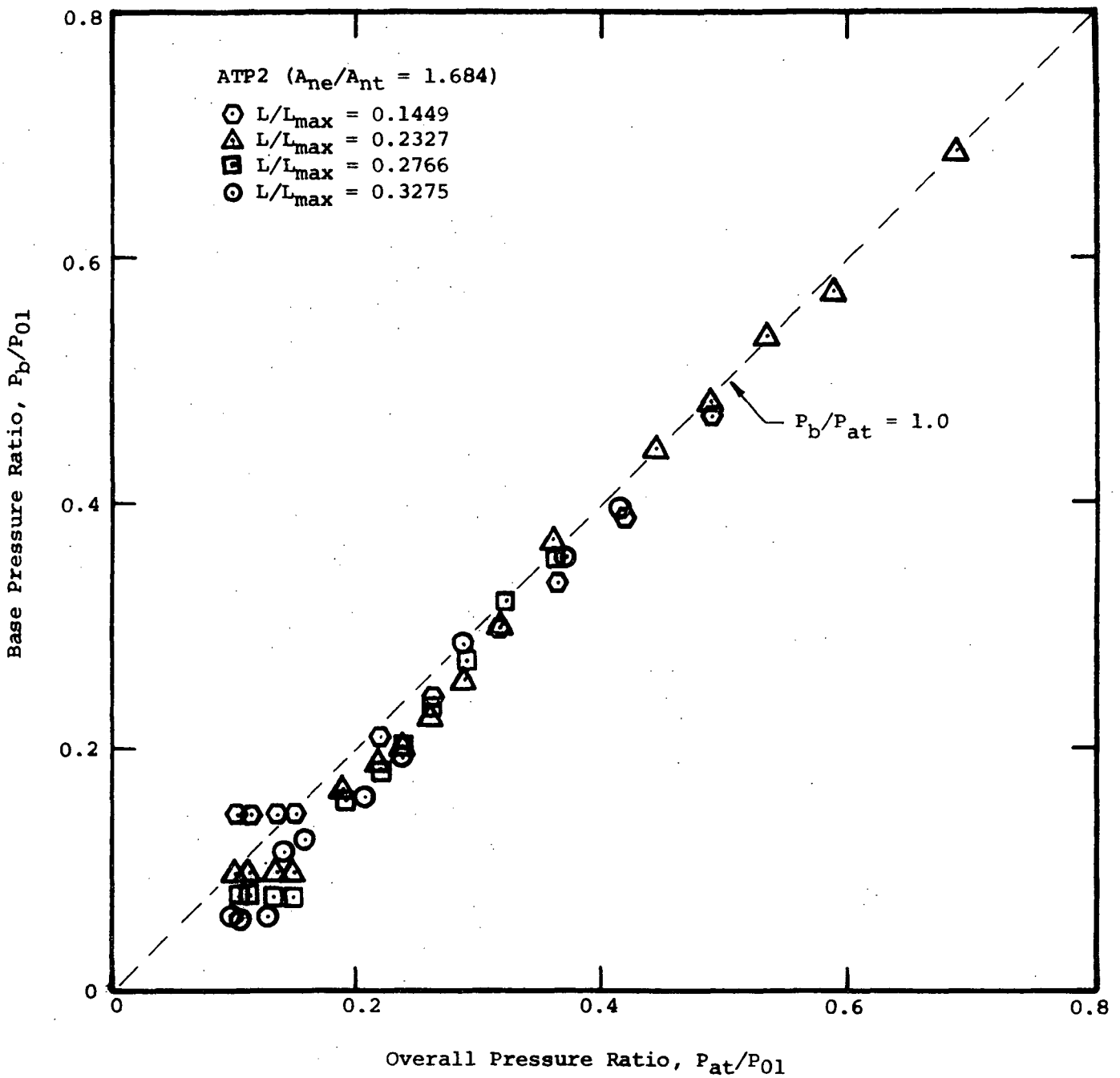

Fig. 11 Base Pressure Characteristics for Axisymmetric Truncated Plug Nozzle ATP2.

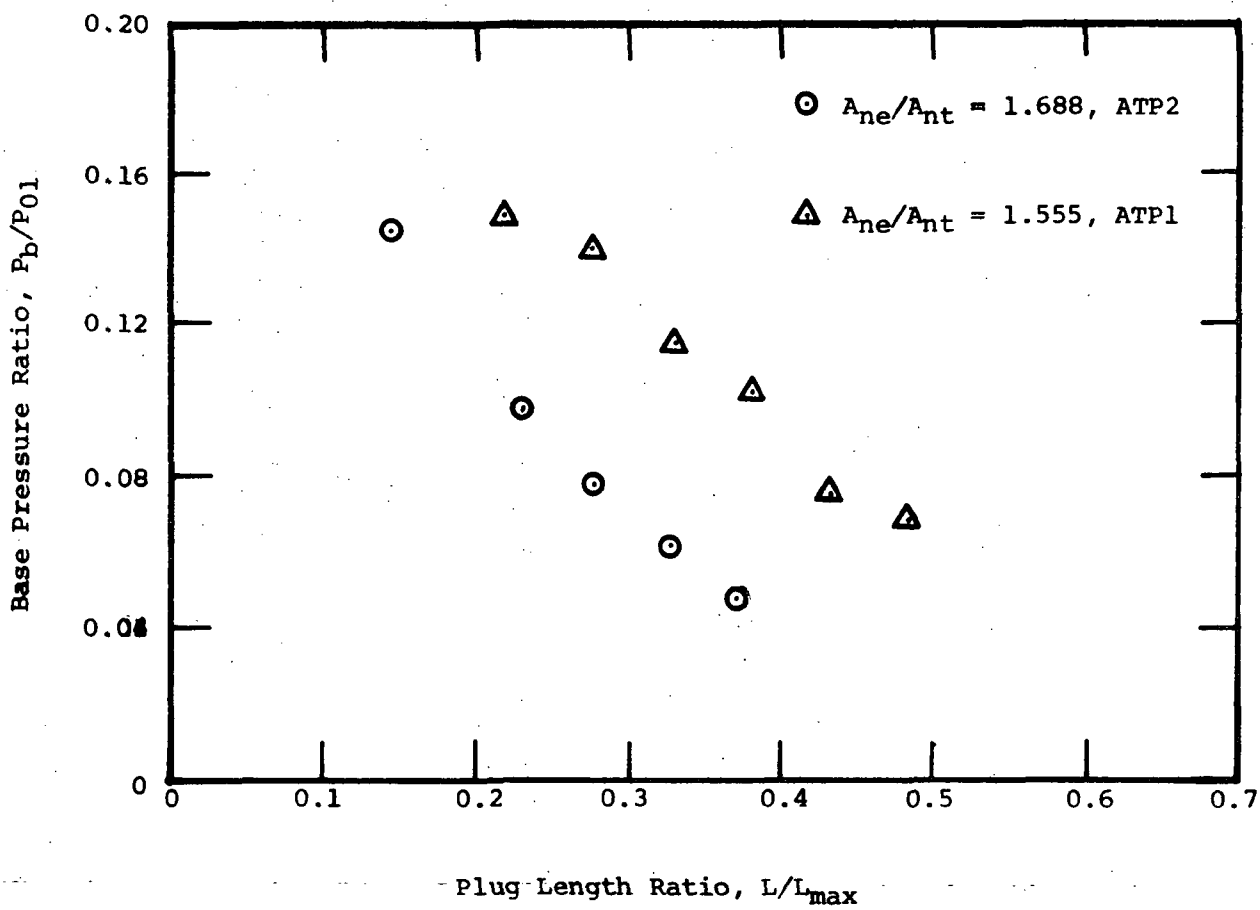

Fig. 12 Variation of "Closed Wake" Base Pressure Ratio with Plug Length Ratio.

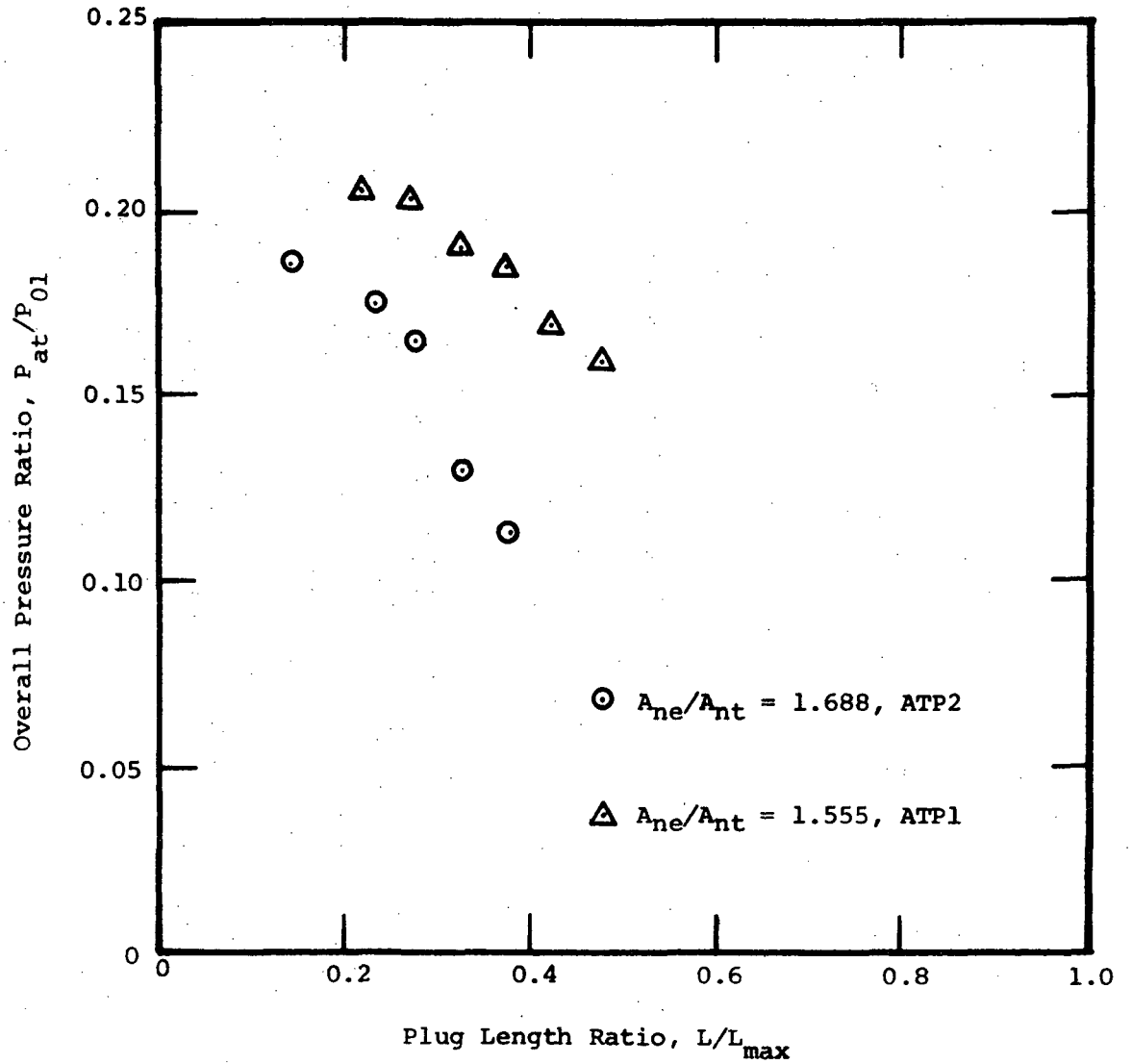

Fig. 13 Effect of Plug Length Ratio on Overall Pressure Ratio at "Wake Closure".

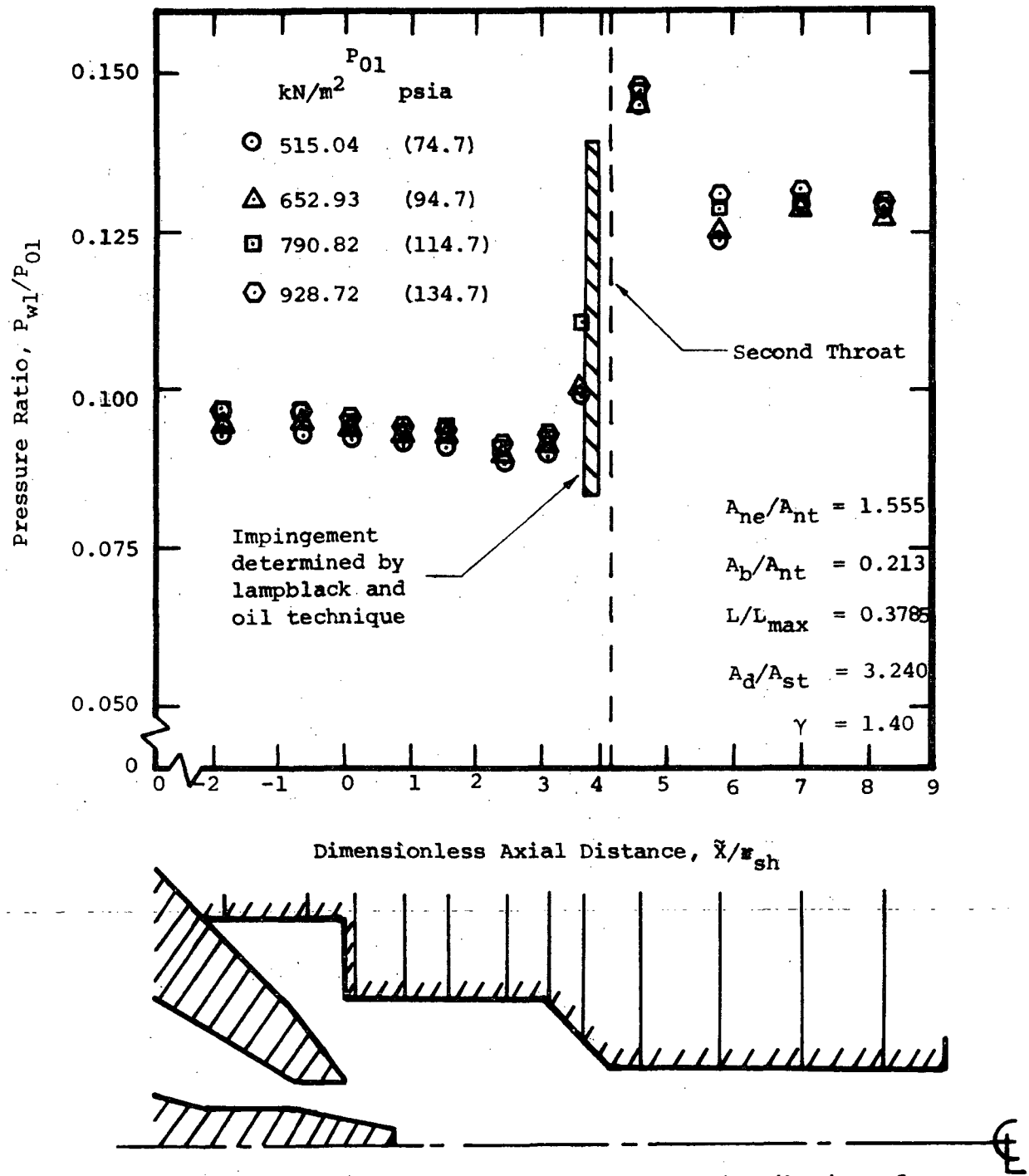

Fig. 14 Long Second Throat Diffuser Static Pressure Distributions for Axisymmetric Truncated Plug Nozzle ATP1 with Plug Wake "Closed".

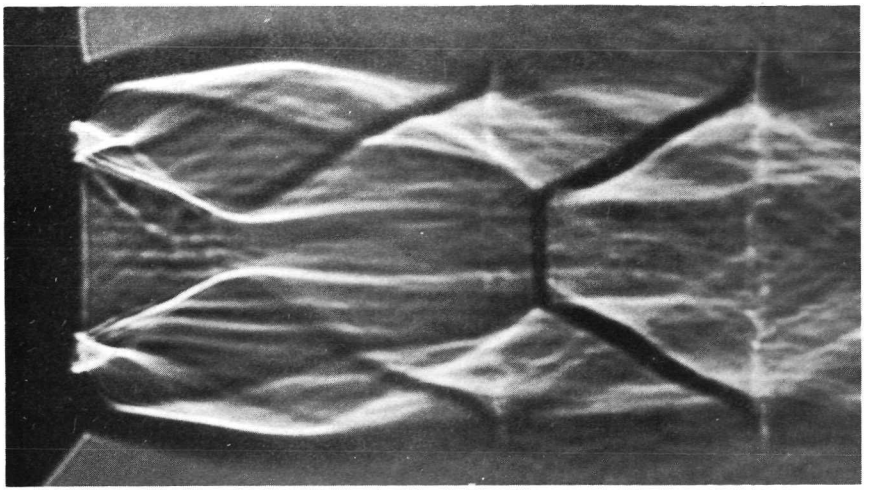

a) $P_{at}/P_{01} = 0.120$ $P_b/P_{01} = 0.149$

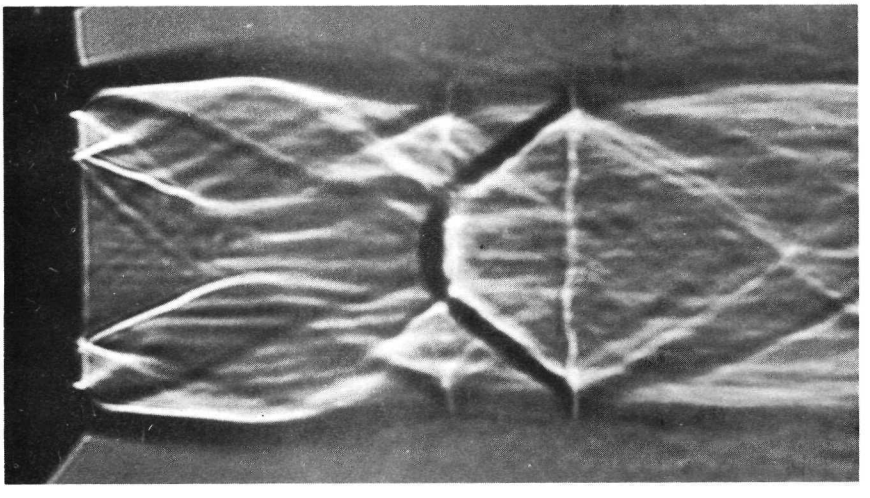

b) $P_{at}/P_{01} = 0.160$ $P_b/P_{01} = 0.149$

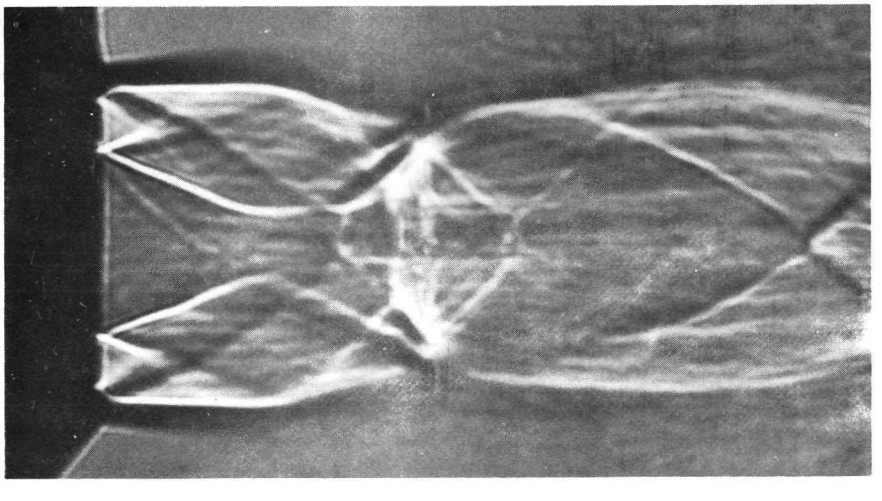

c) $P_{at}/P_{01} = 0.200$ $P_b/P_{01} = 0.149$

Fig. 15 Shadowgraph Sequence of ATP1 Axisymmetric Truncated Plug Nozzle Flow Field ($L/L_{max} = 0.2184$).

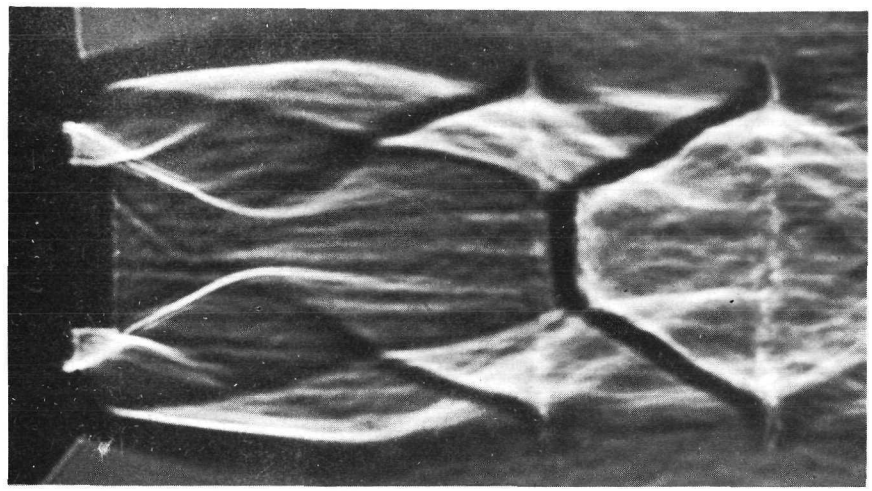

a) $P_{at}/P_{01} = 0.120$ $P_b/P_{01} = 0.140$

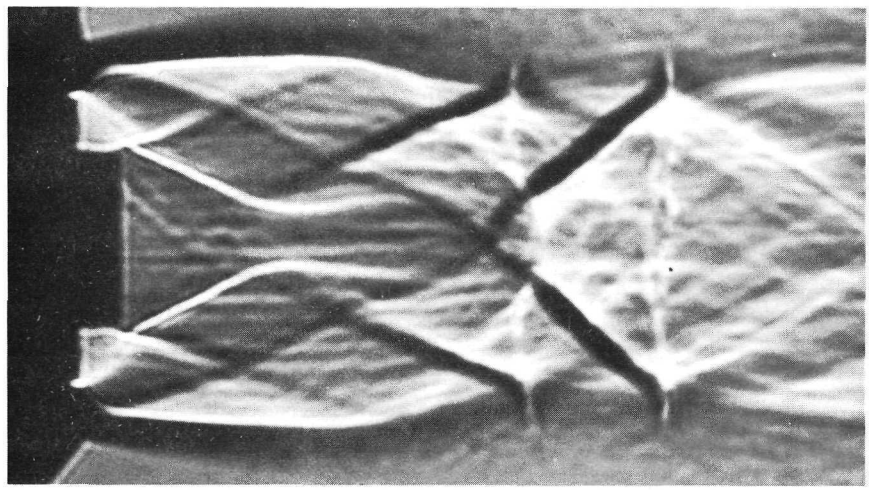

b) $P_{at}/P_{01} = 0.160$ $P_b/P_{01} = 0.140$

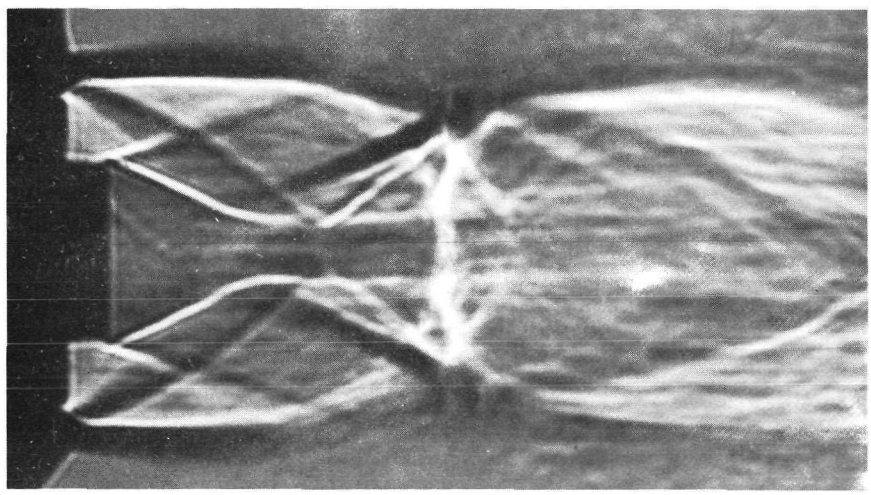

c) $P_{at}/P_{01} = 0.200$ $P_b/P_{01} = 0.140$

Fig. 16 Shadowgraph Sequence of ATP1 Axisymmetric Truncated Plug Nozzle Flow Field ($L/L_{max} = 0.2766$).

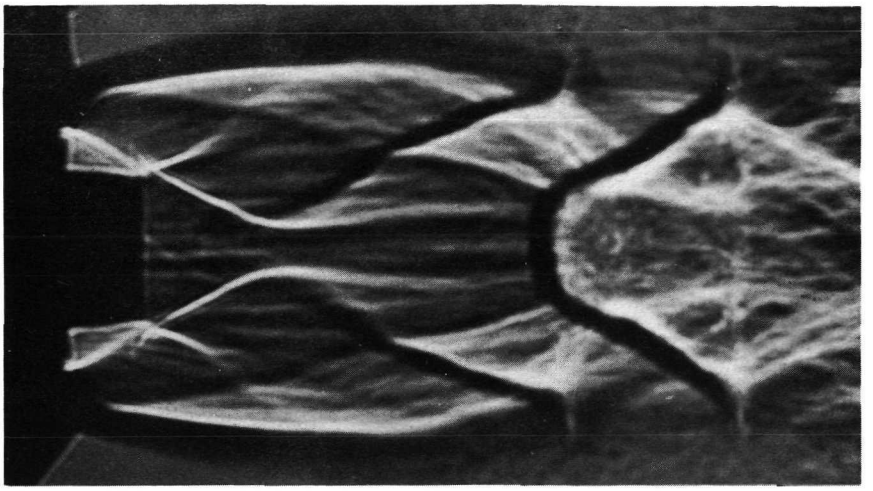

a) $P_{at}/P_{01} = 0.120$ $P_b/P_{01} = 0.116$

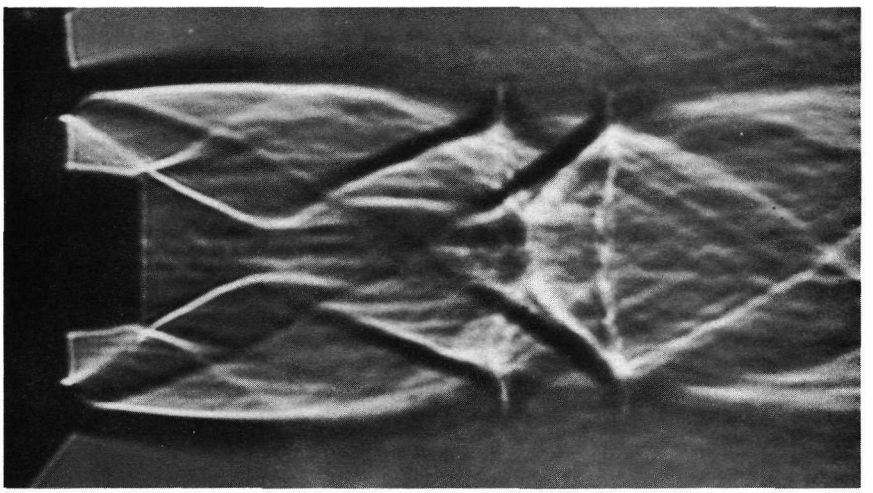

b) $P_{at}/P_{01} = 0.160$ $P_b/P_{01} = 0.116$

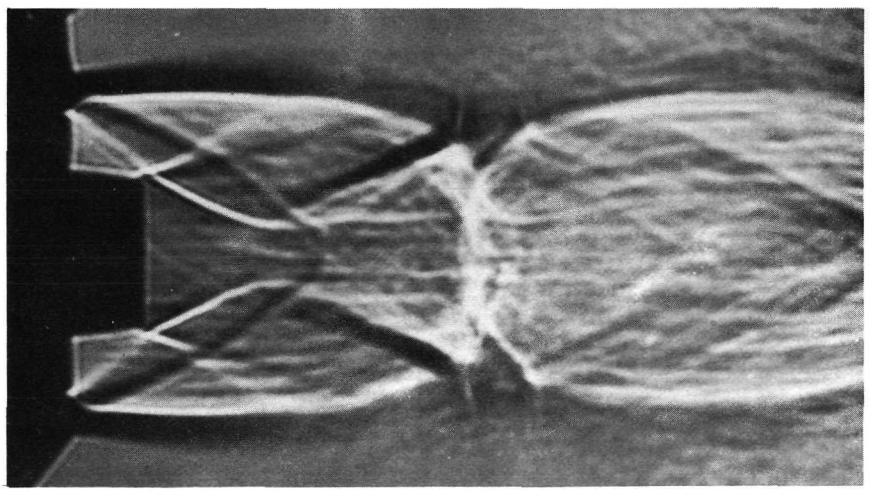

c) $P_{at}/P_{01} = 0.190$ $P_b/P_{01} = 0.116$

Fig. 17 Shadowgraph Sequence of ATP1 Axisymmetric Truncated Plug Nozzle Flow Field ($L/L_{max} = 0.3275$).

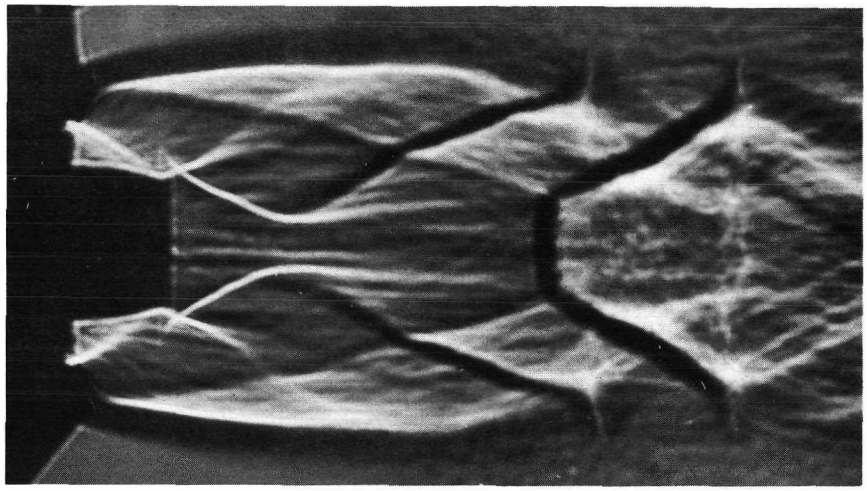

a) $P_{at}/P_{01} = 0.120$ $P_b/P_{01} = 0.104$

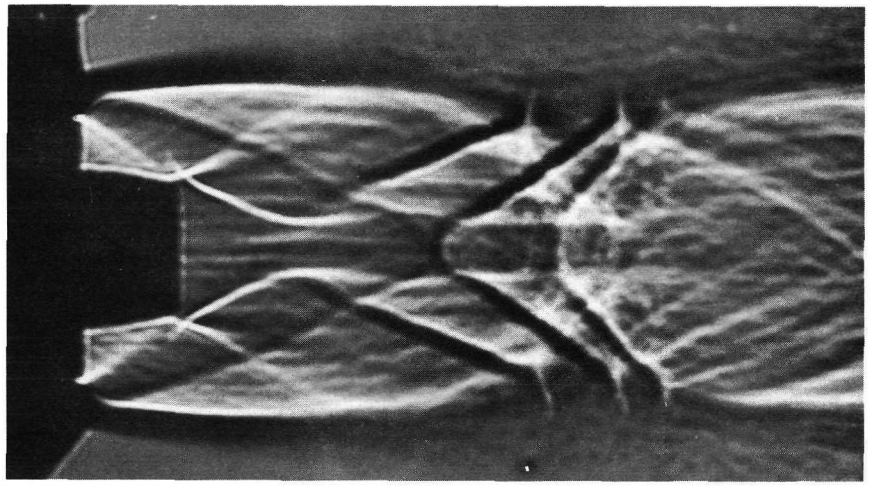

b) $P_{at}/P_{01} = 0.160$ $P_b/P_{01} = 0.104$

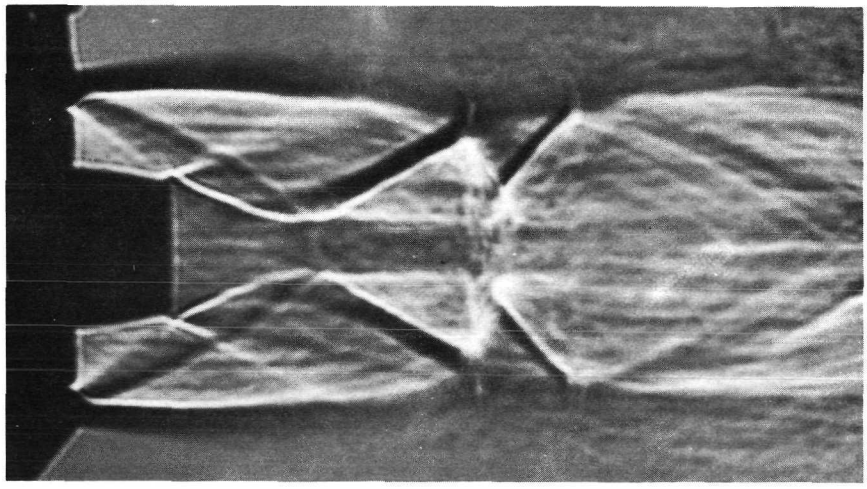

c) $P_{at}/P_{01} = 0.190$ $P_b/P_{01} = 0.104$

Fig. 18 Shadowgraph Sequence of ATP1 Axisymmetric Truncated Plug Nozzle Flow Field ($L/L_{max} = 0.3785$).

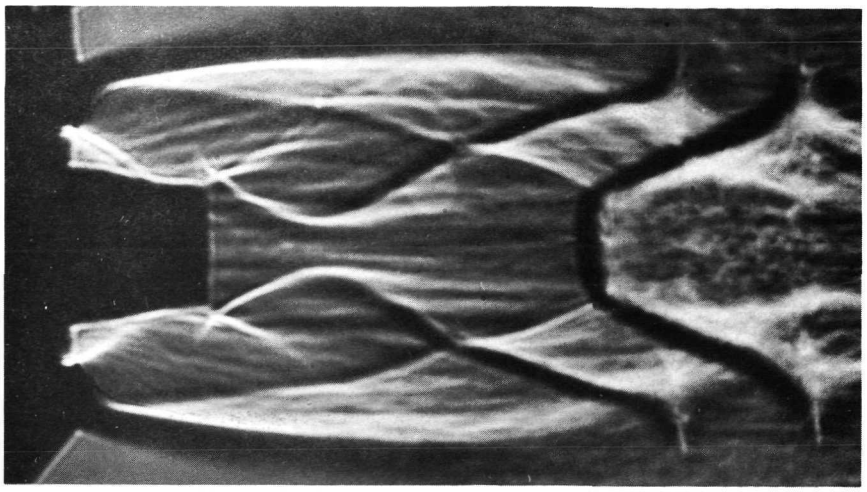

a) $P_{at}/P_{01} = 0.110$ $P_b/P_{01} = 0.078$

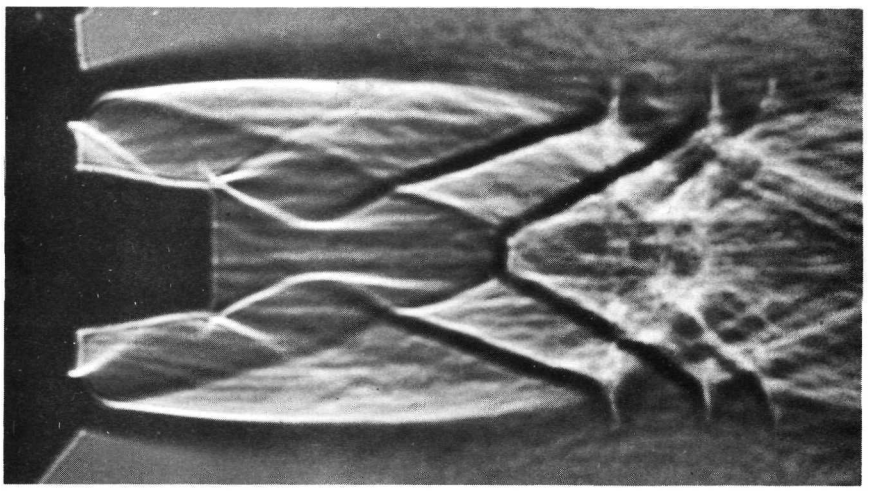

b) $P_{at}/P_{01} = 0.140$ $P_b/P_{01} = 0.078$

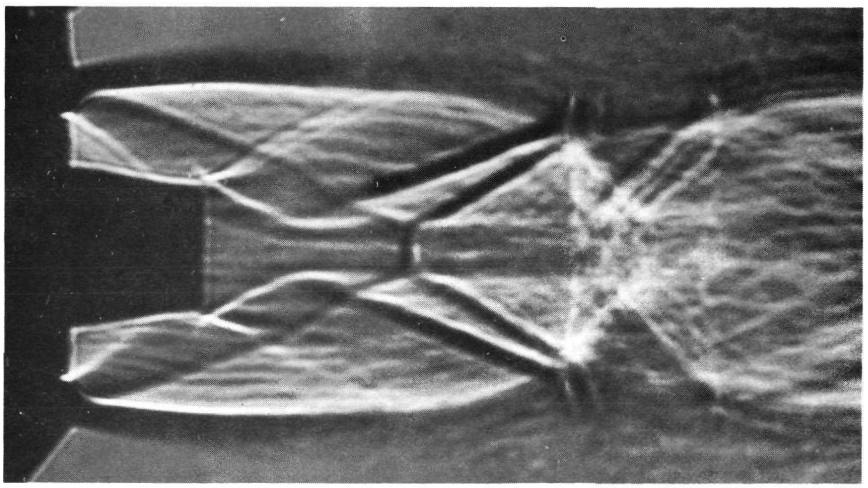

c) $P_{at}/P_{01} = 0.160$ $P_b/P_{01} = 0.078$

Fig. 19 Shadowgraph Sequence of ATP1 Axisymmetric Truncated Plug Nozzle Flow Field ($L/L_{max} = 0.4290$).

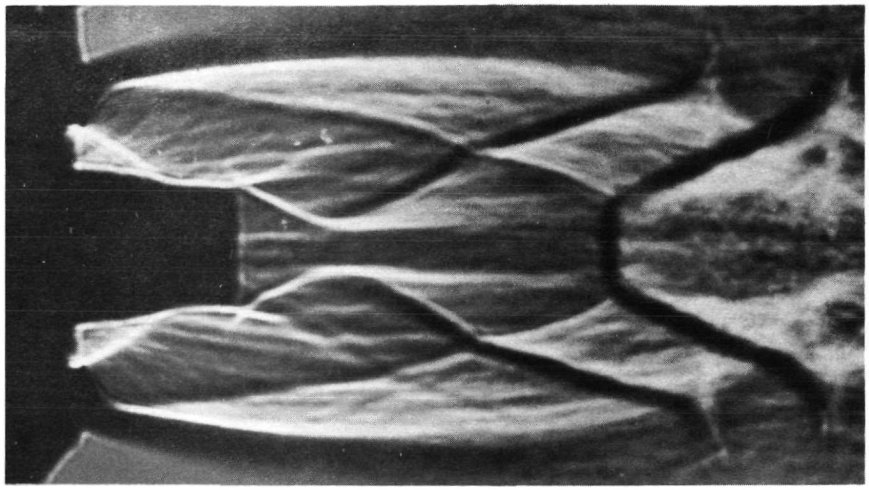

a) P_{at}/P_{01} = 0.110 P_b/P_{01} = 0.070

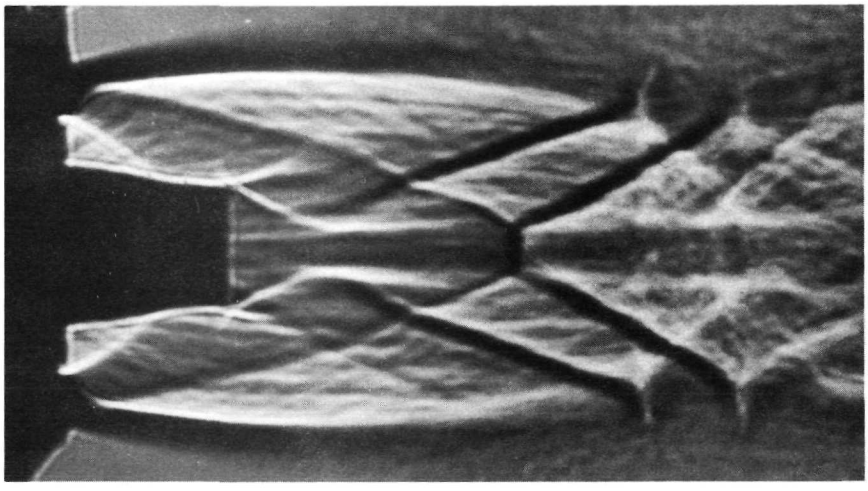

b) P_{at}/P_{01} = 0.135 P_b/P_{01} = 0.070

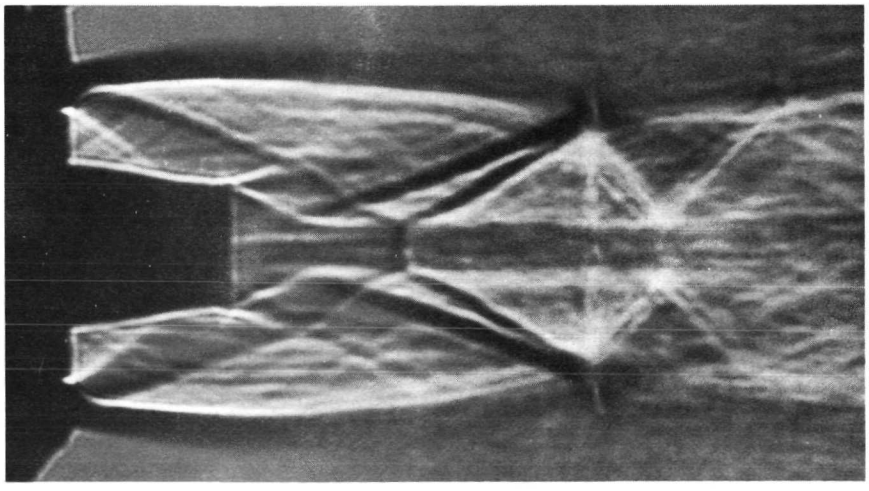

c) P_{at}/P_{01} = 0.160 P_b/P_{01} = 0.070

Fig. 20 Shadowgraph Sequence of ATP1 Axisymmetric Truncated Plug Nozzle Flow Field (L/L_{max} = 0.4802).

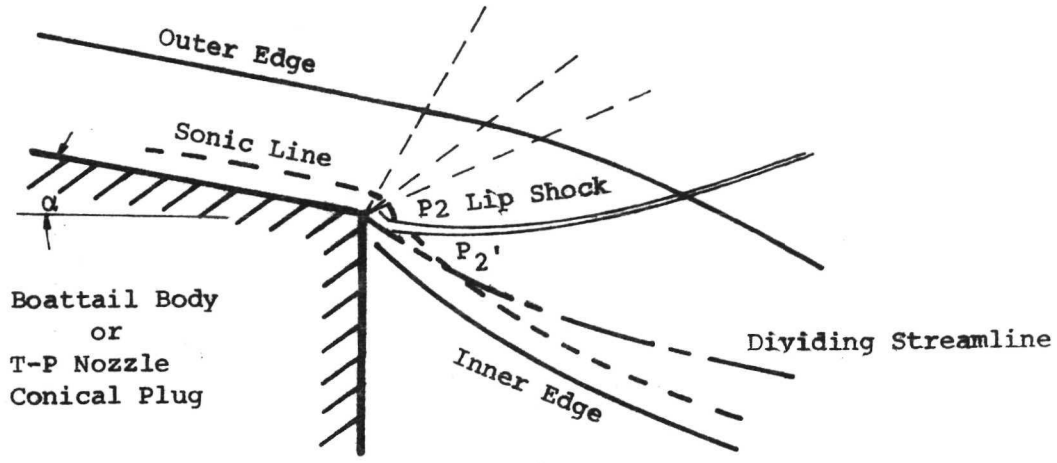

a. Flow Behavior Near Separation and Formation of Lip Shock

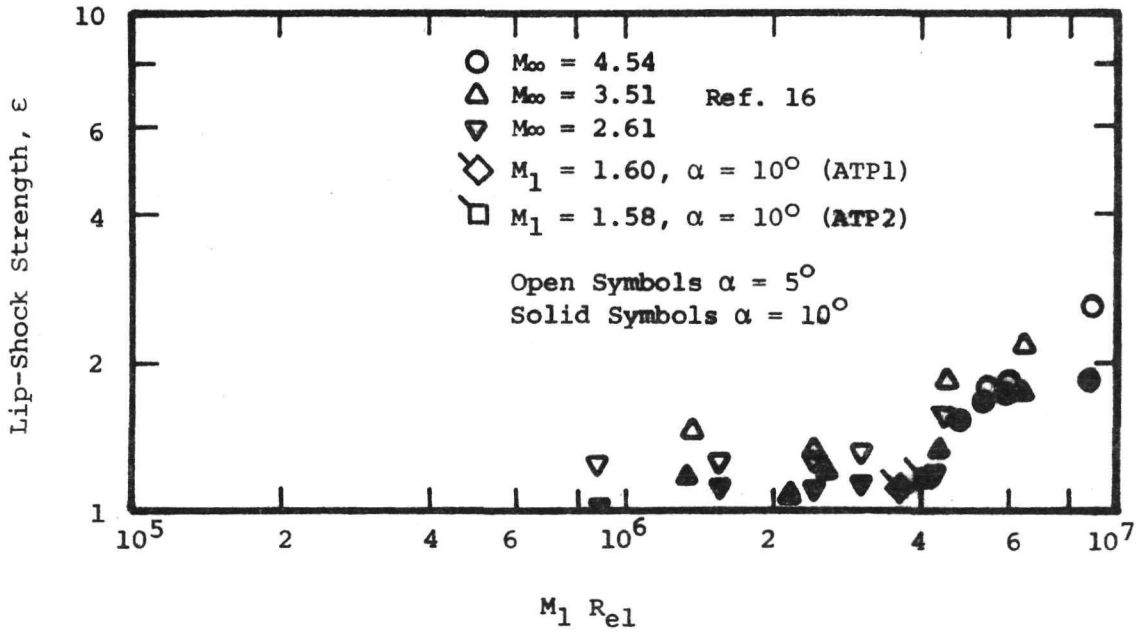

b. Reynolds Number Dependence of Lip-Shock Strength (Boattail).

Fig. 21 Comparison of Lip-Shock Strength of ATP1 and ATP2 with Results of Hama (Ref. 16) for Boattail Bodies.

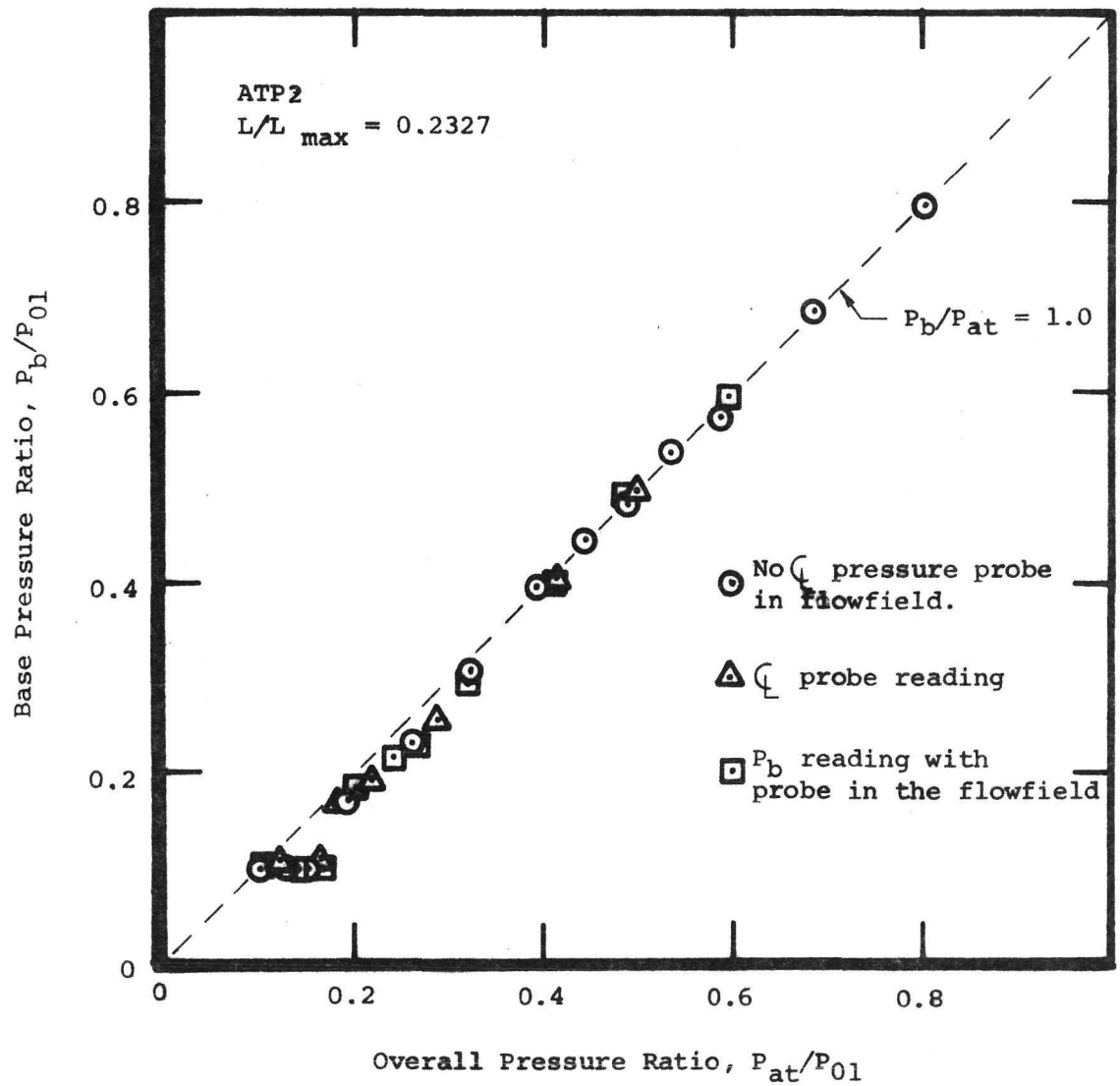

Fig. 22 Base Pressure Characteristics for Axisymmetric Truncated Plug Nozzle ATP2.

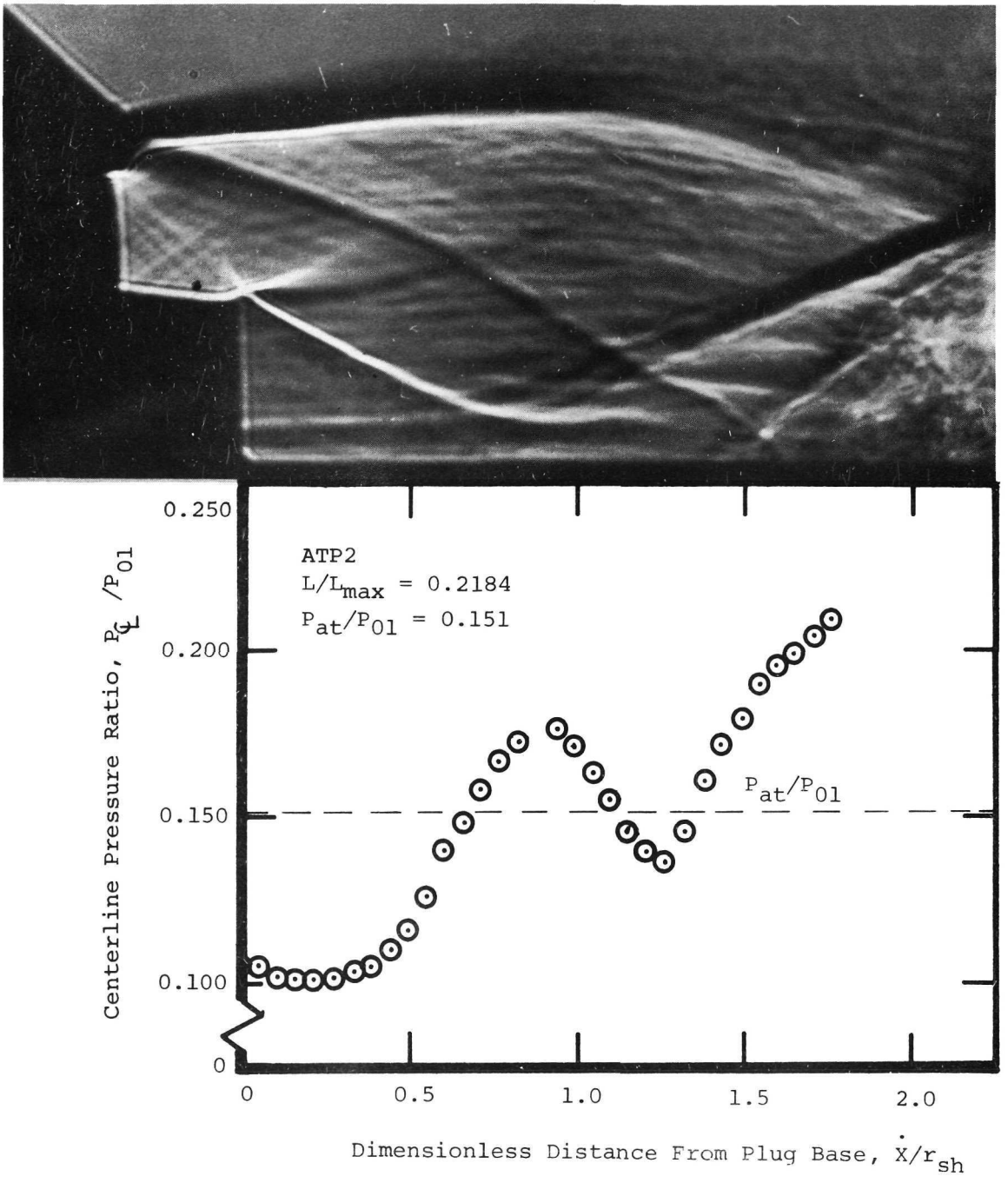

Fig. 23 Correlation of Shadowgraph Photograph and Centerline Static Pressure Ratio Variation for "Closed Wake" Condition.

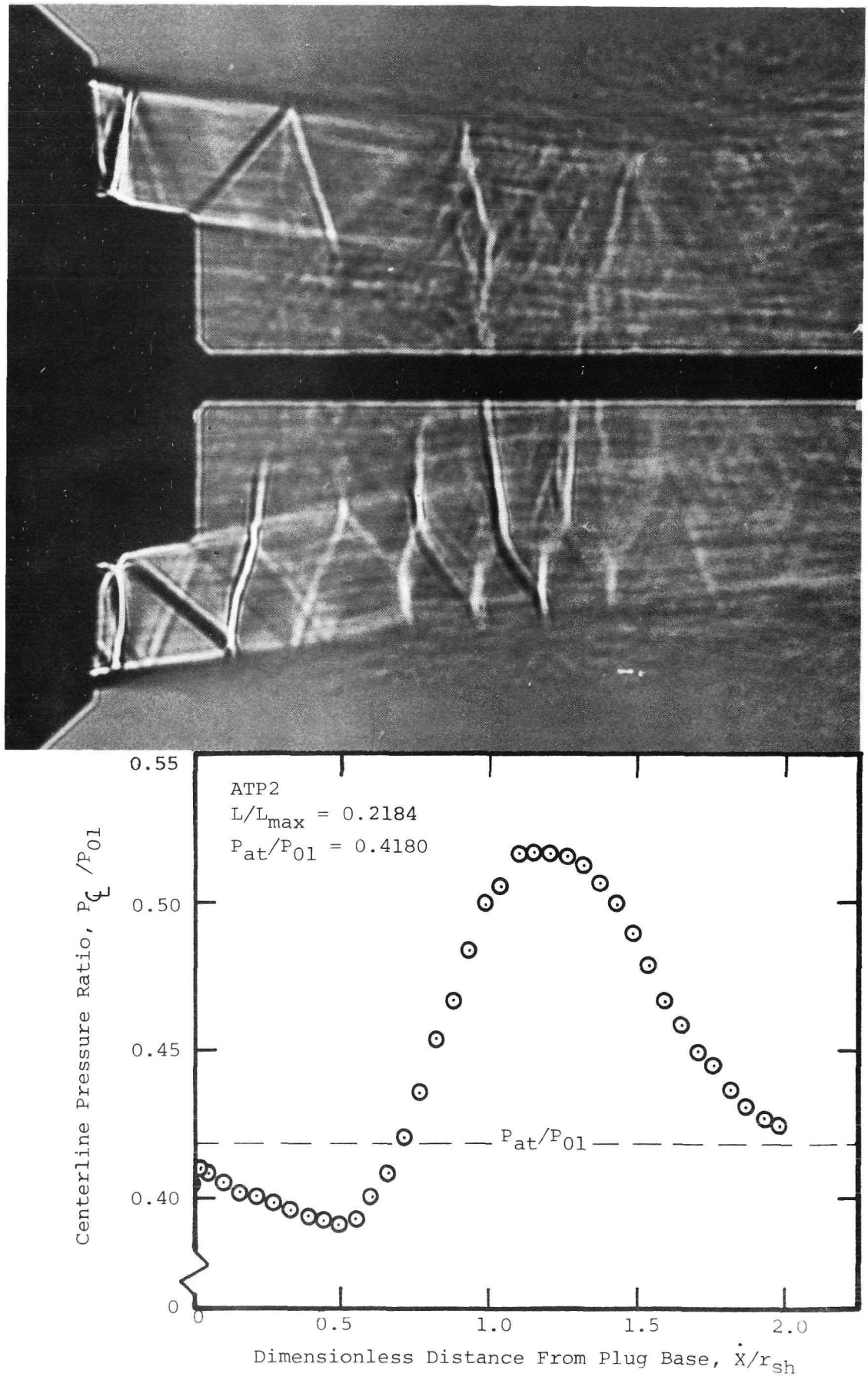

Fig. 24 Correlation of Shadowgraph Photograph and Centerline Static Pressure Ratio Variation for an "Open Wake" Condition.

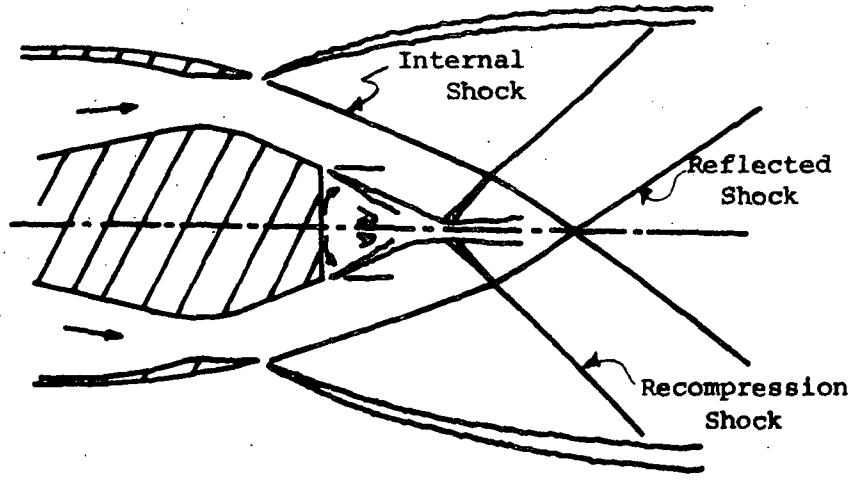

a.) Regular Reflection of Internal Shock

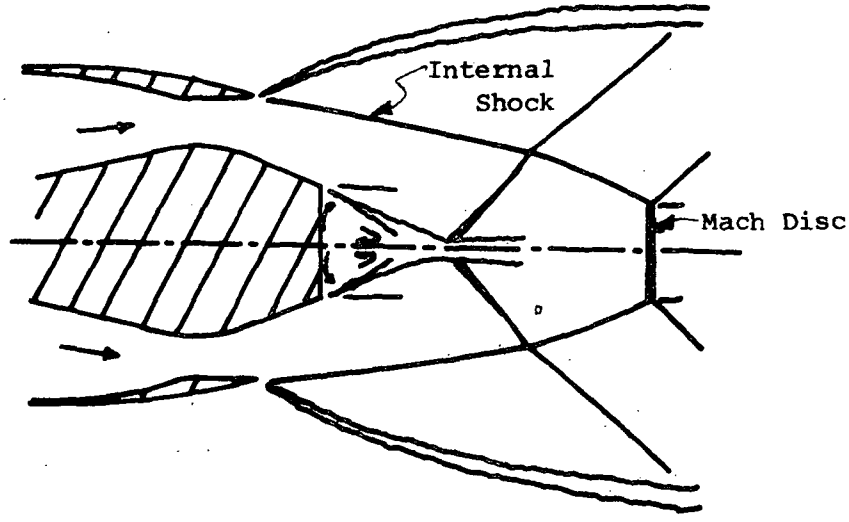

b.) Primary Mach Disc Formation

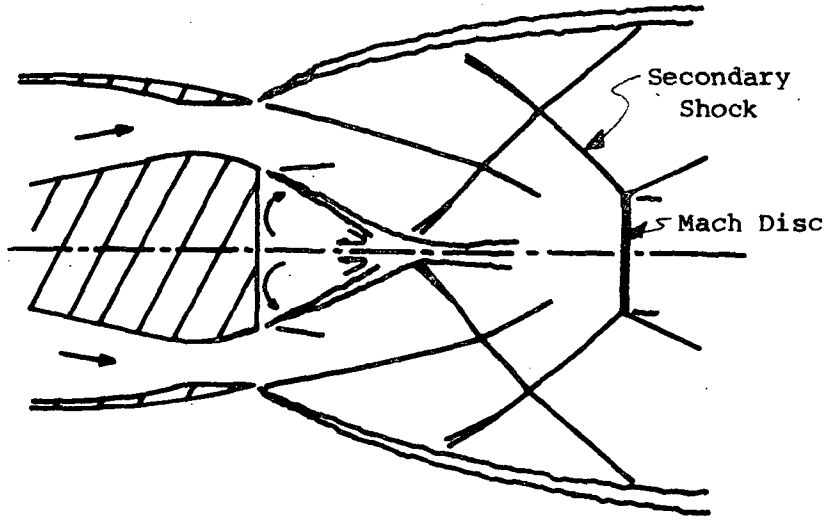

c.) Secondary Mach Disc Formation

Fig. 25 Shock Wave Interactions for an Axisymmetric Truncated Plug Nozzle.

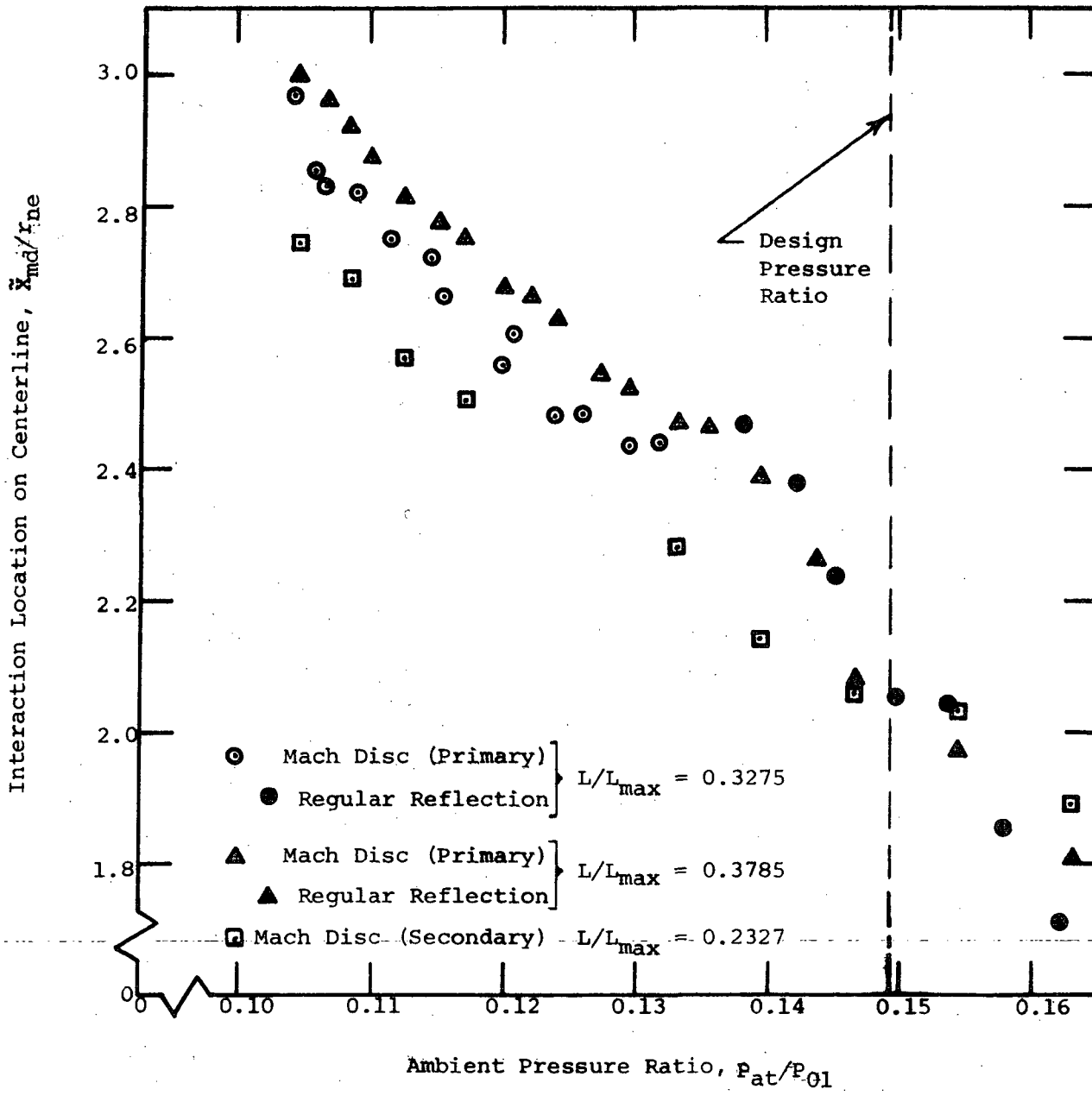

Fig. 26 Effect of Ambient Pressure Ratio on Mach Disc Location (A_{ne}/A_{nt}=1.555).

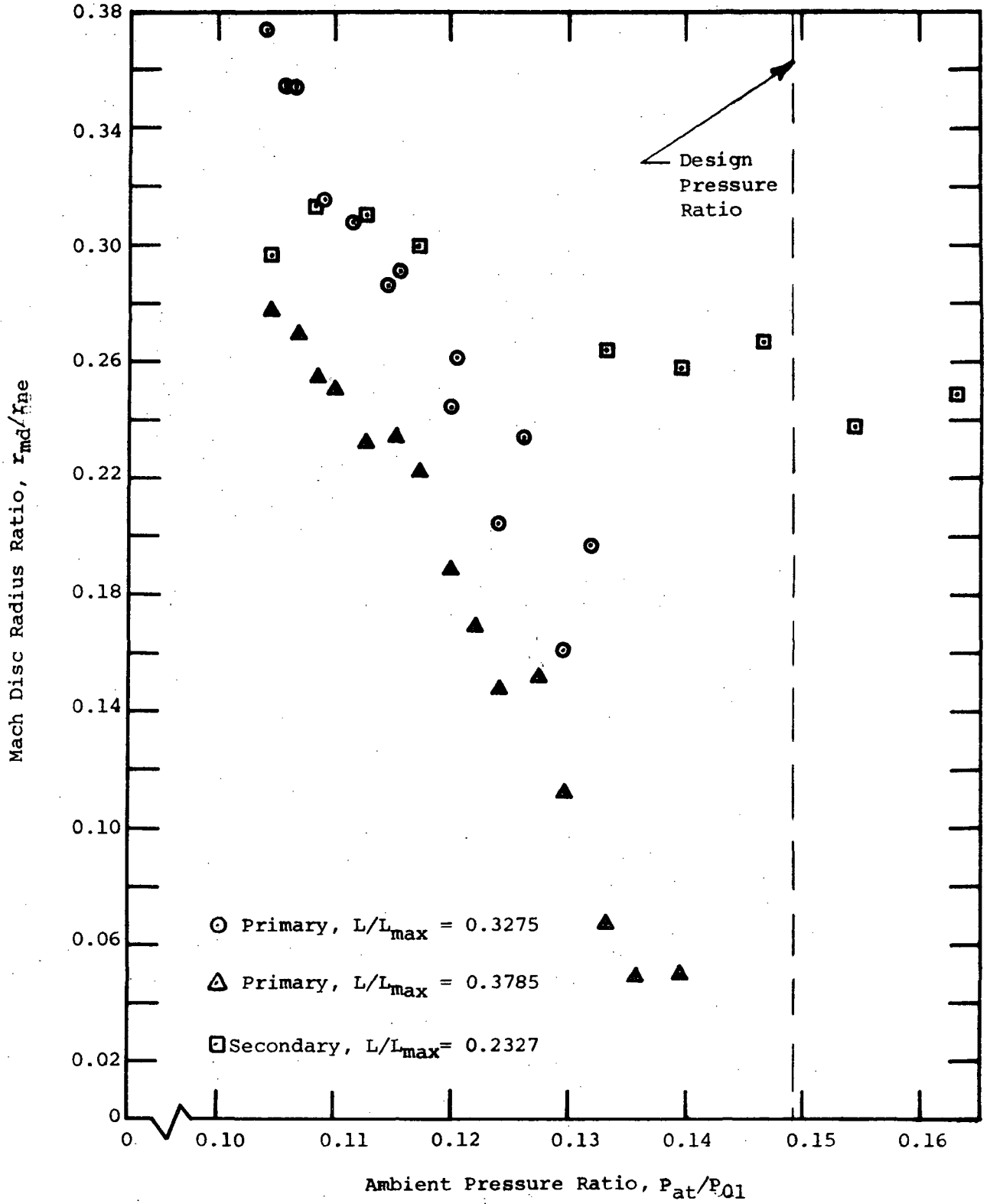

Fig. 27 Effect of Ambient Pressure Ratio on Mach Disc Size (A_{ne}/A_{nt} = 1.555).

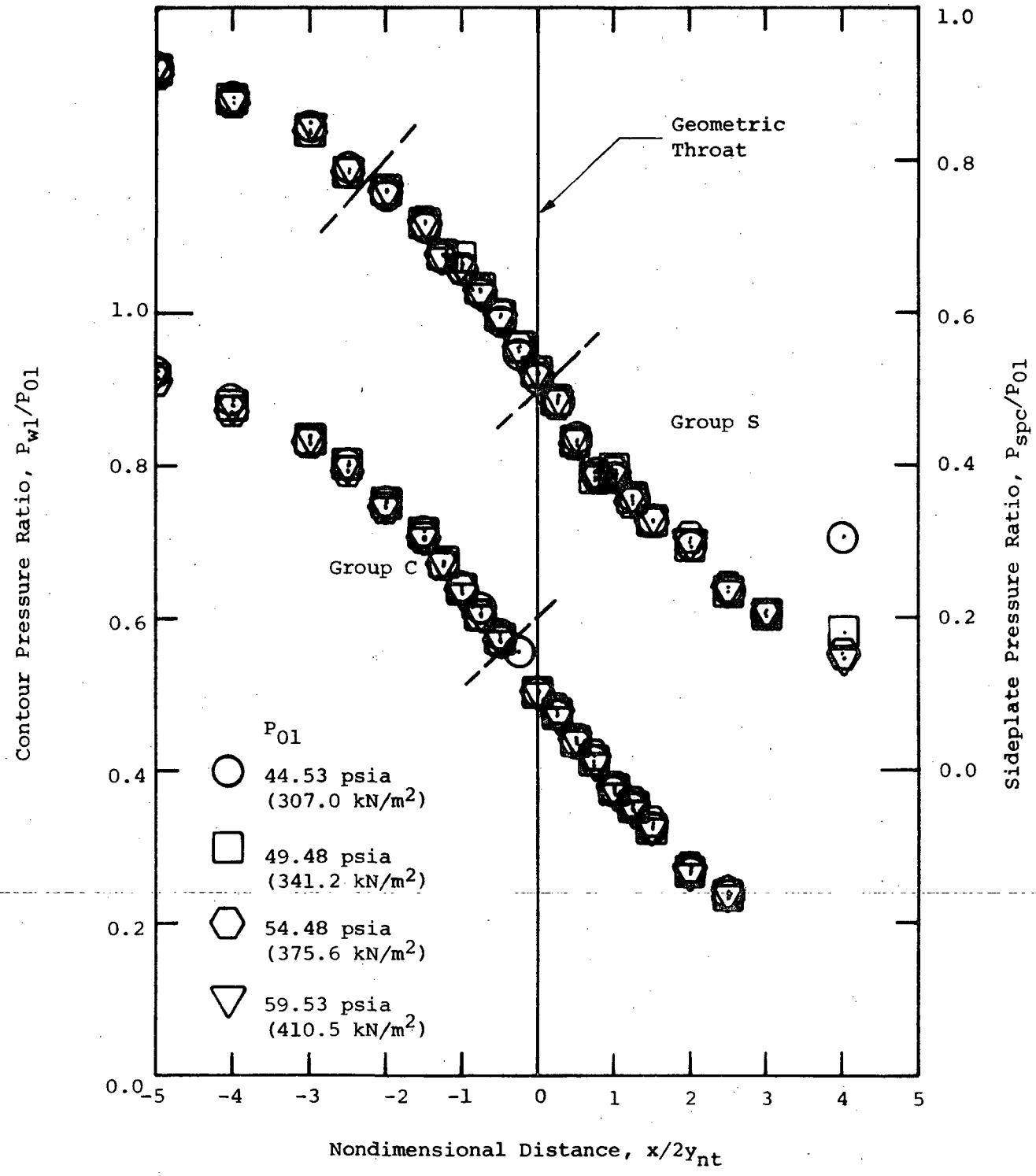

Fig. 28 Static Pressure Ratios versus Nondimensional Distance from Geometric Throat for PLTR1.

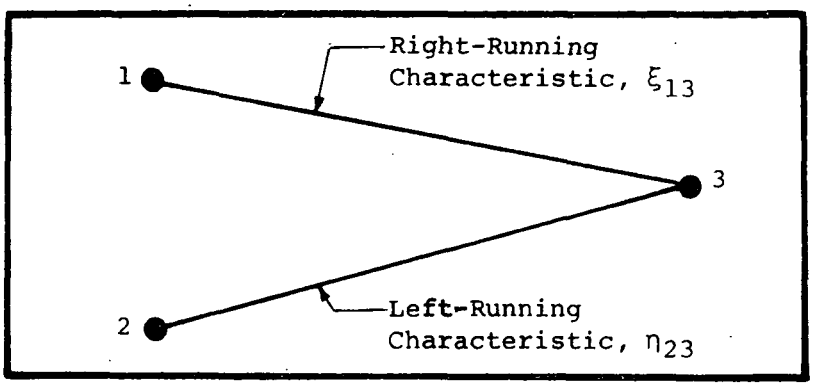

a) Interior Point

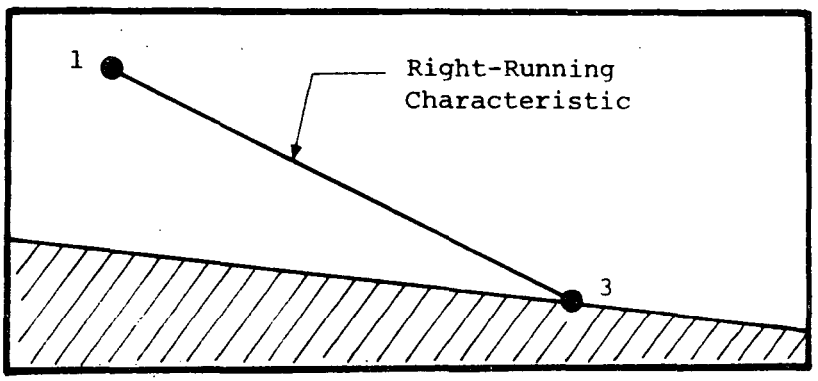

b) Solid Lower Boundary

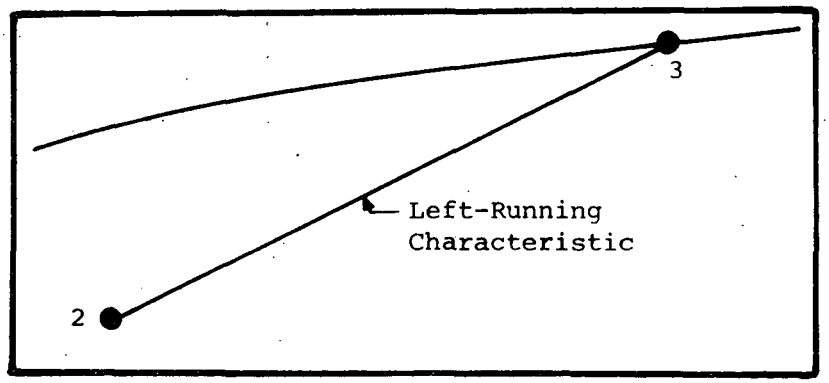

c) Constant Pressure Upper Boundary

Fig. 29 Method of Characteristics Computation Scheme.

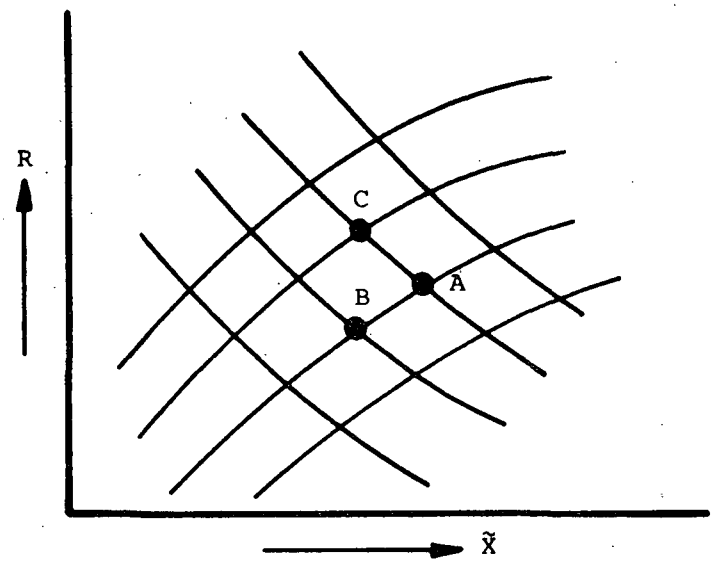

a) Standard Method of Characteristics

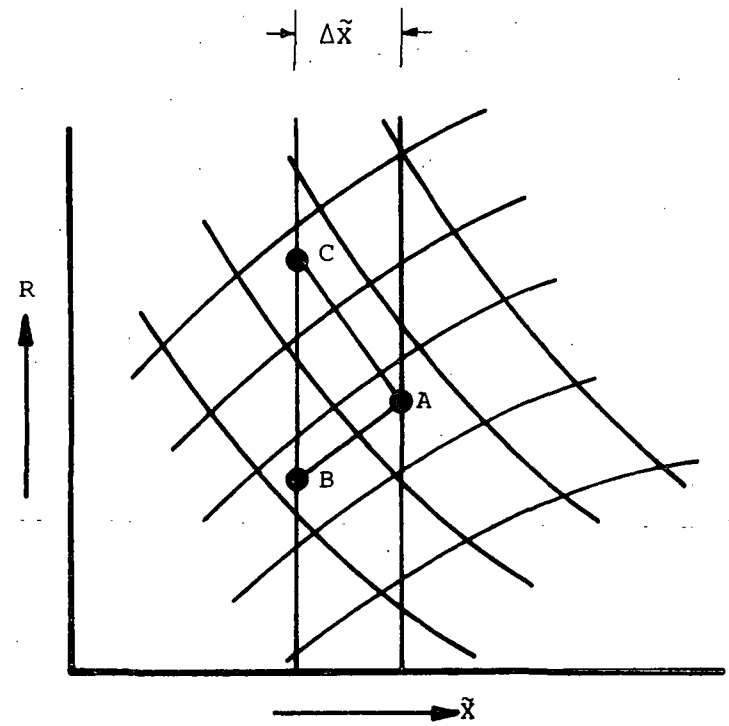

b) Hartree Technique

Fig. 30 Comparison between Standard Method of Characteristics and Hartree Technique.

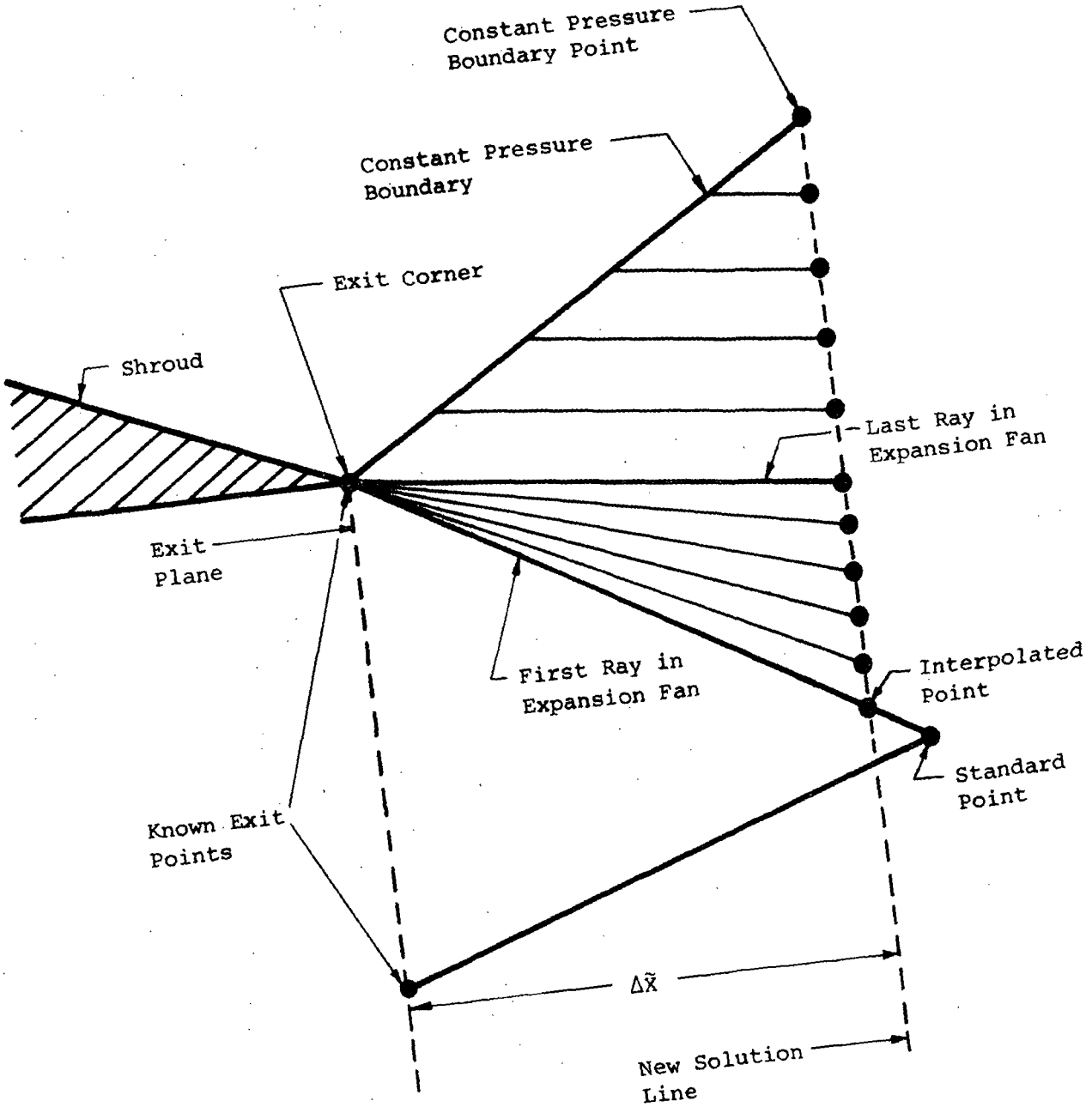

Fig. 31 Corner Expansion Computation Scheme.

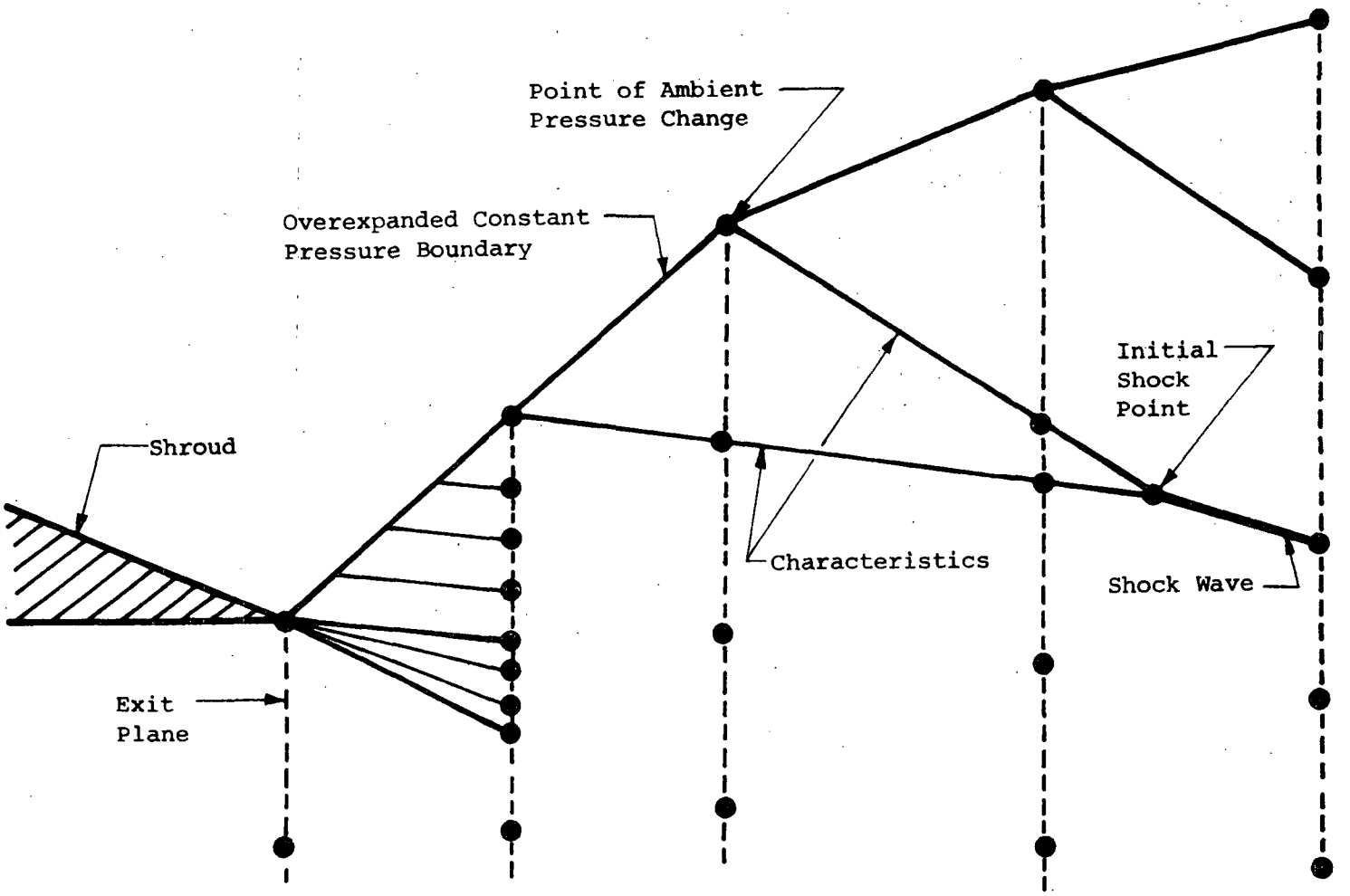

Fig. 32 Computation Scheme for Initial Shock Wave Point.

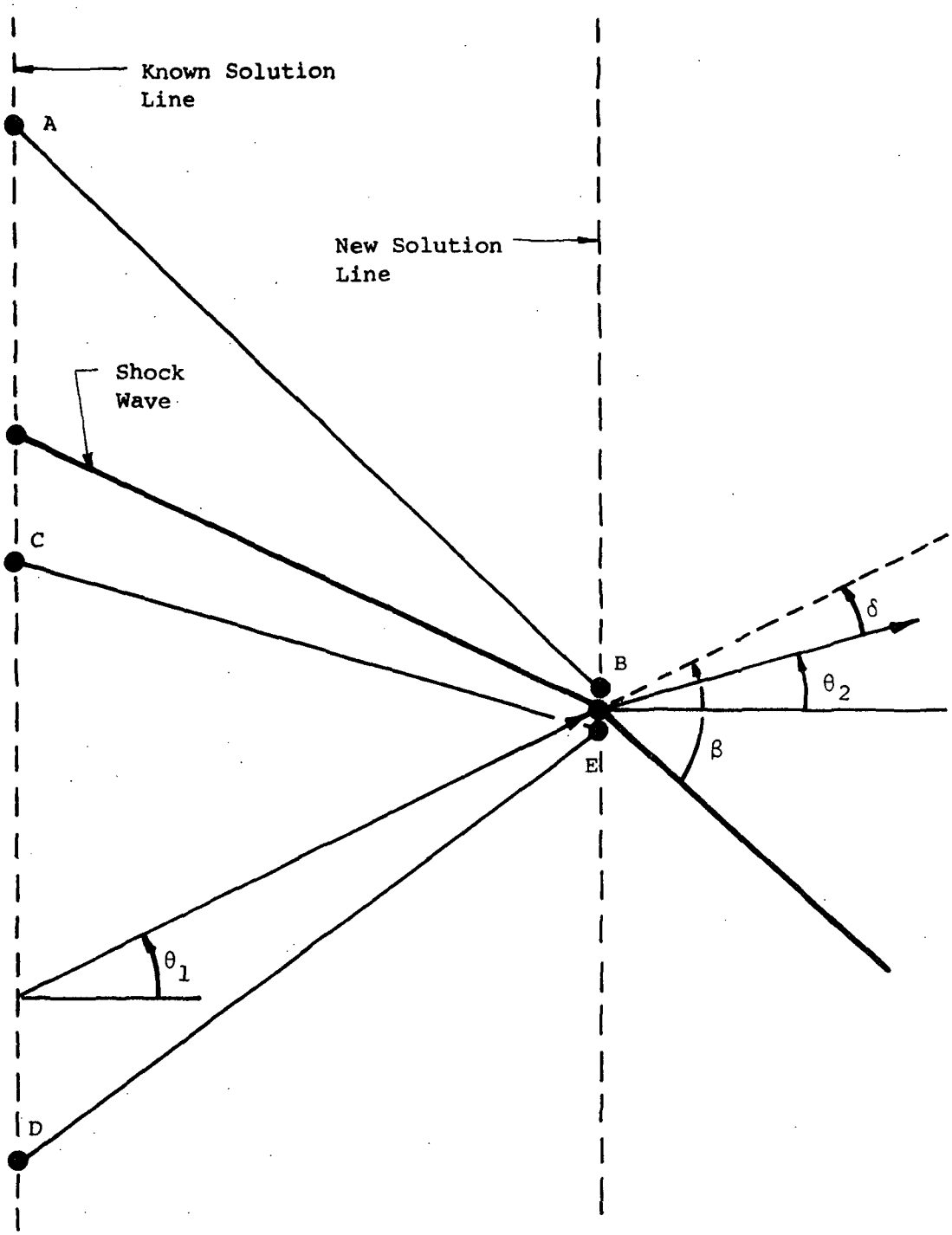

Fig. 33 Computation Scheme for Shock Wave Point.

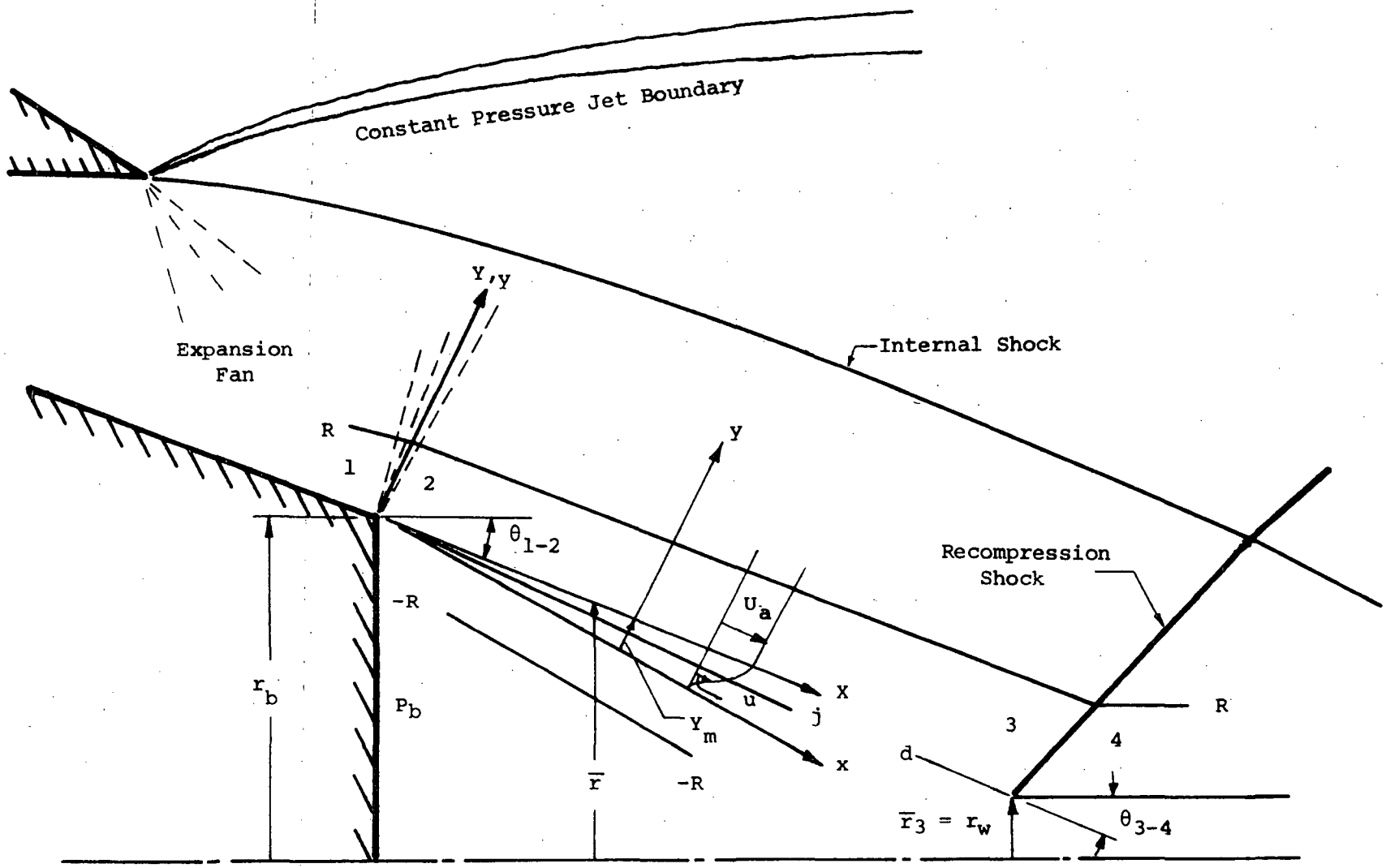

Fig. 34 Flow Model for the Determination of the Turbulent Base Pressure for an Axisymmetric Truncated Plug Nozzle.

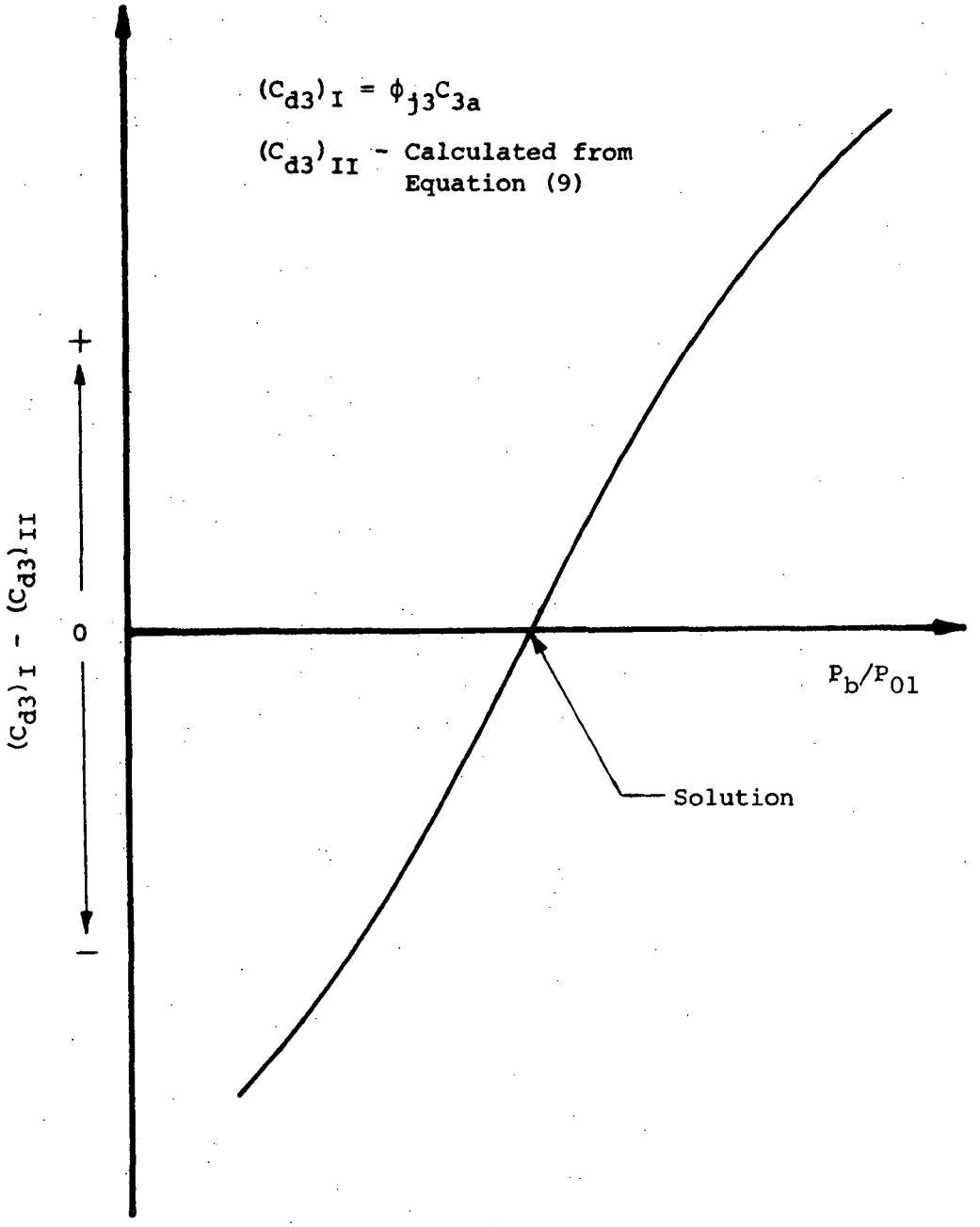

Fig. 35 Base Pressure Solution Curve.

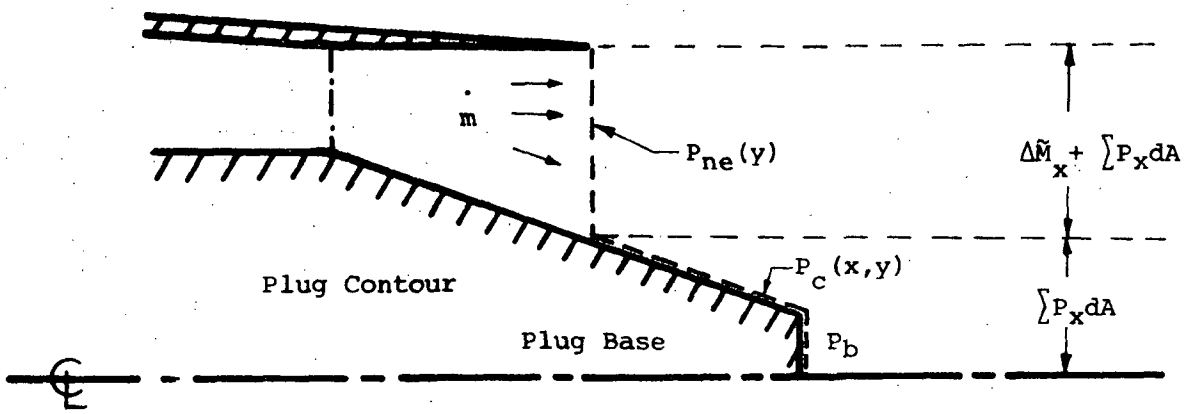

a. Control Volume for Thrust Calculation.

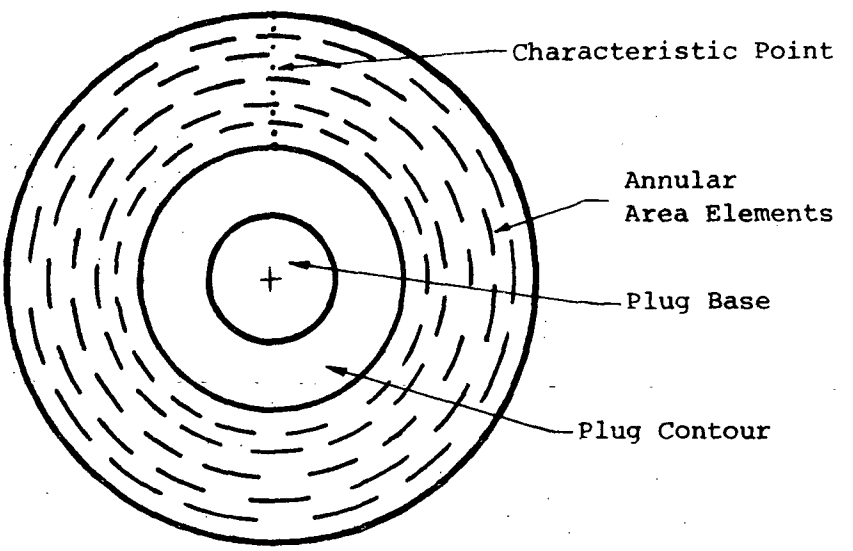

b. End view of T-P Nozzle.

Fig. 36 Static Thrust Determination for Axisymmetric Truncated Plug Nozzle.

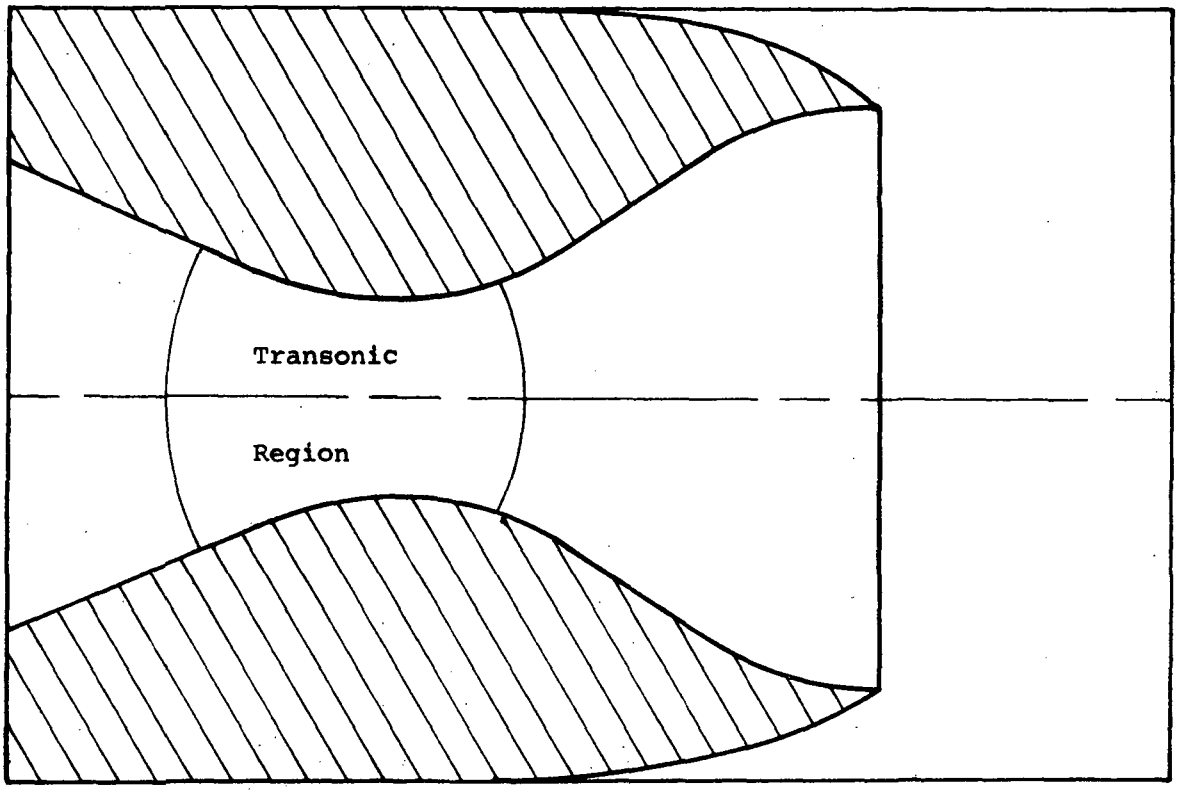

a. Bell Nozzle

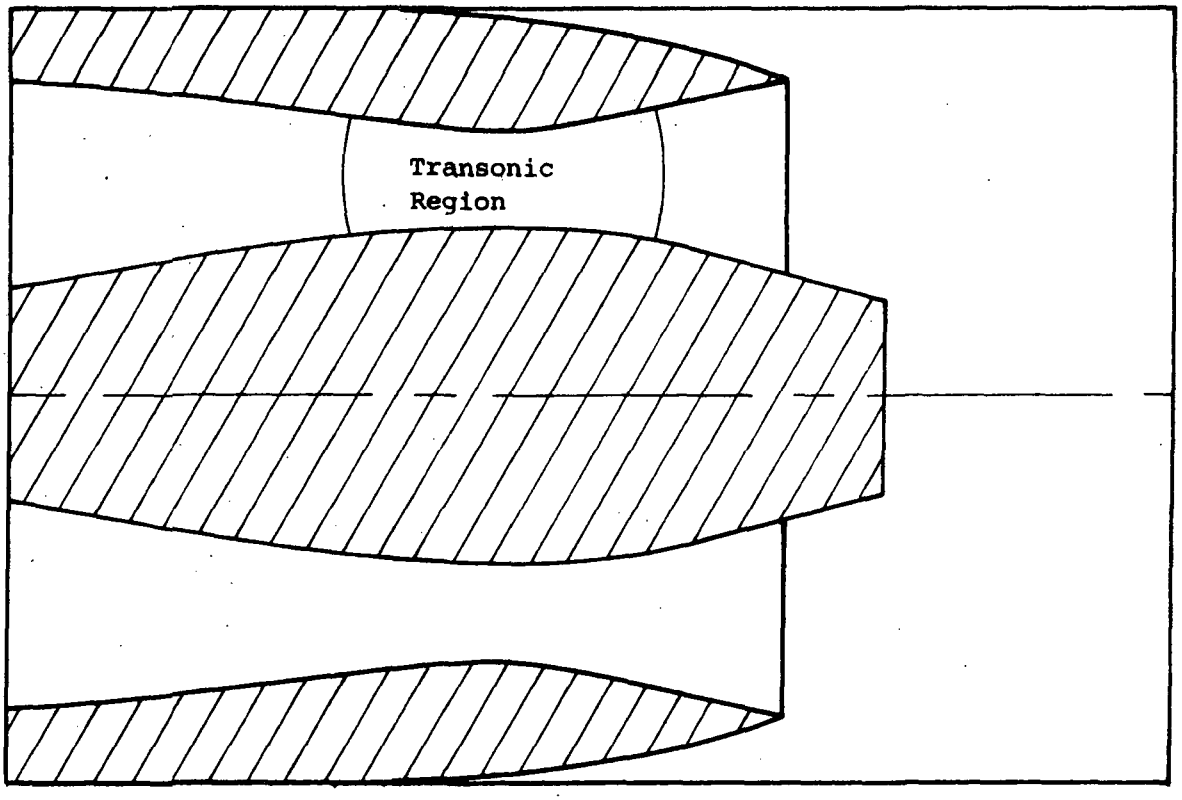

b. Truncated Plug Nozzle

Fig. 37 Transonic Region in Bell Nozzle and Truncated Plug Nozzles.

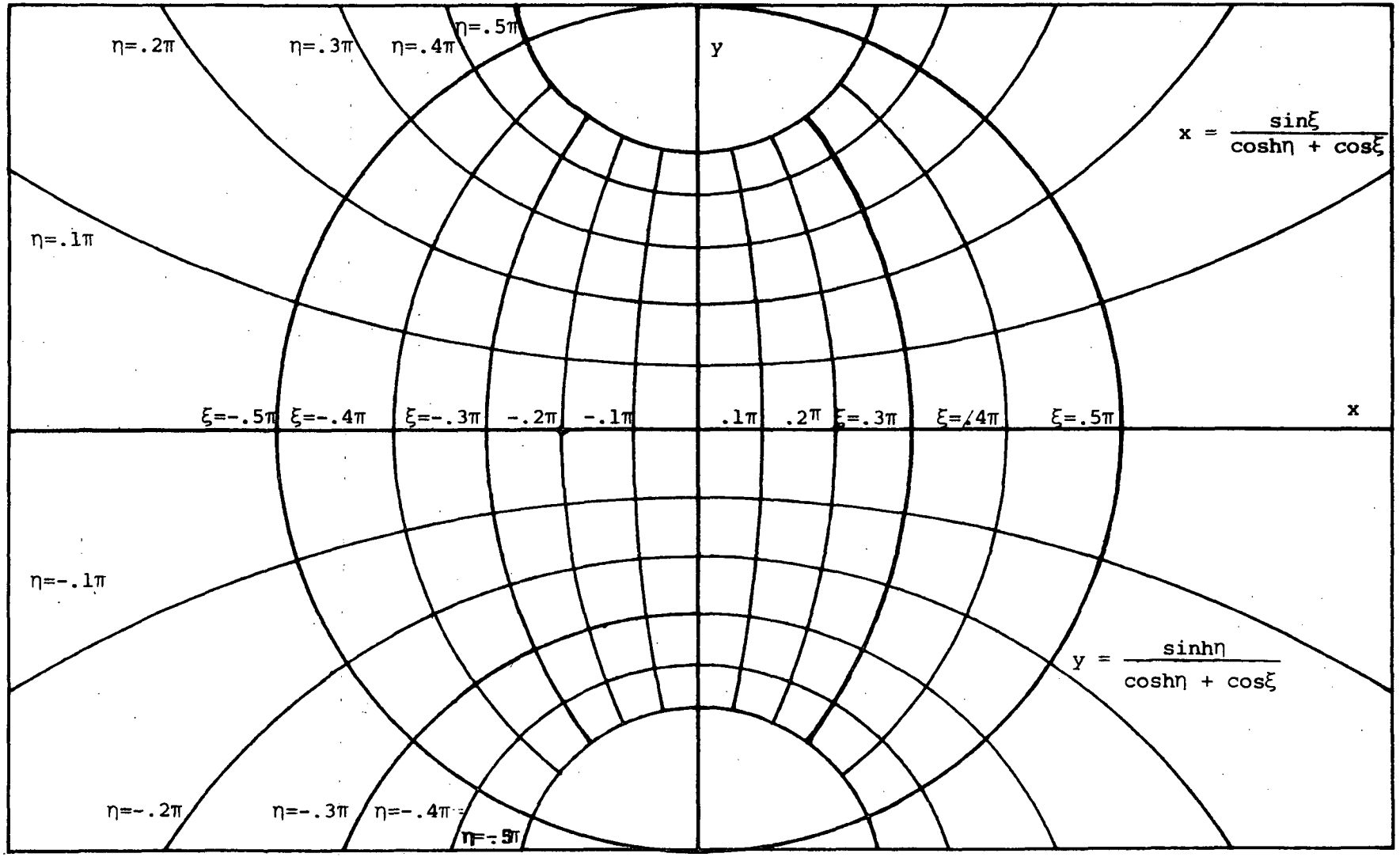

Fig. 38 Bipolar Co-ordinate System for Transonic Region.

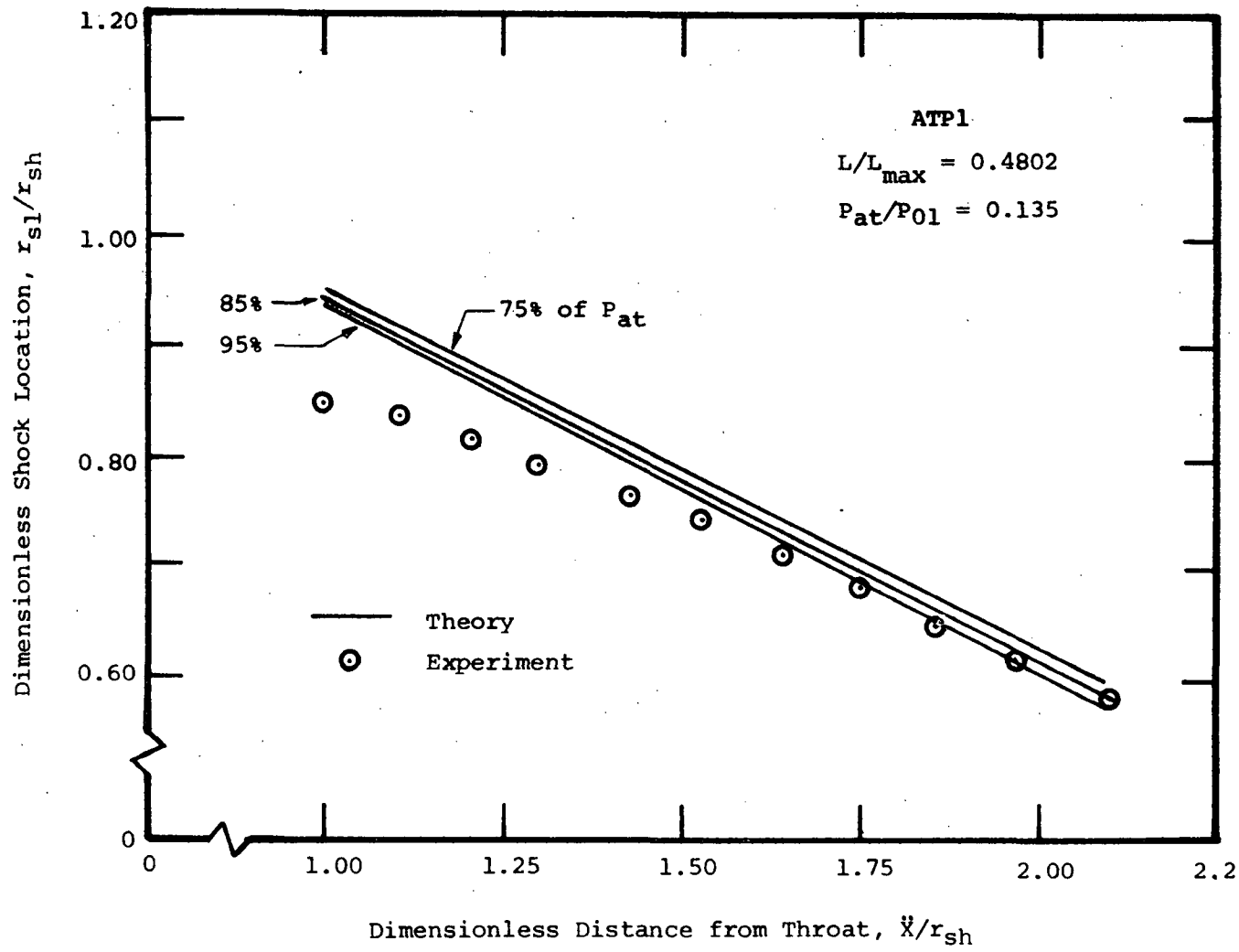

Fig. 39 Effect of Overexpansion on Internal Shock Location, Shroud Exit at $\ddot{X}/r_{sh}$ = 0.742.

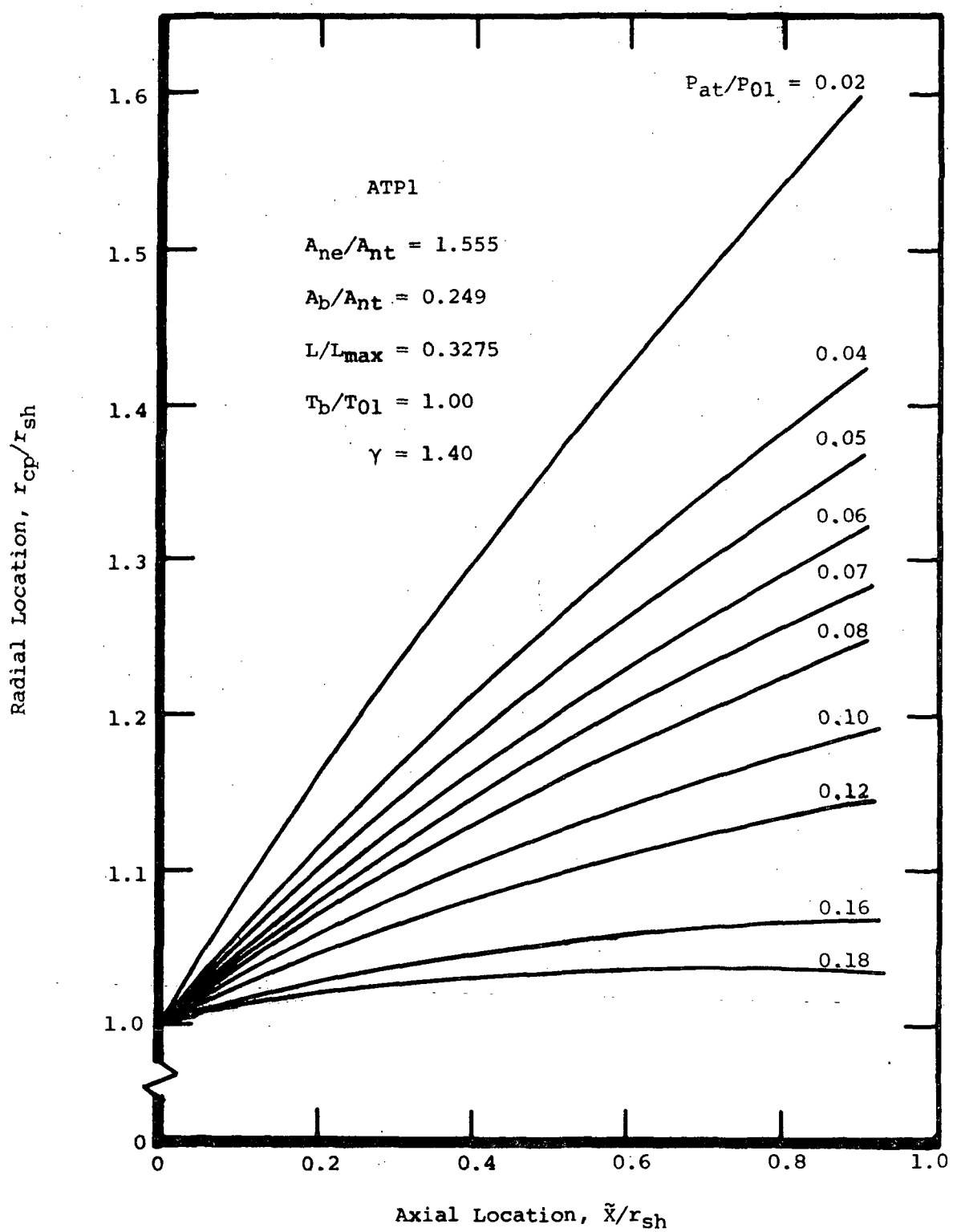

Fig. 40 Effect of Ambient Pressure Ratio on the Constant Pressure Boundary Location for an Axisymmetric T-P Nozzle with a 10° Conical Plug.

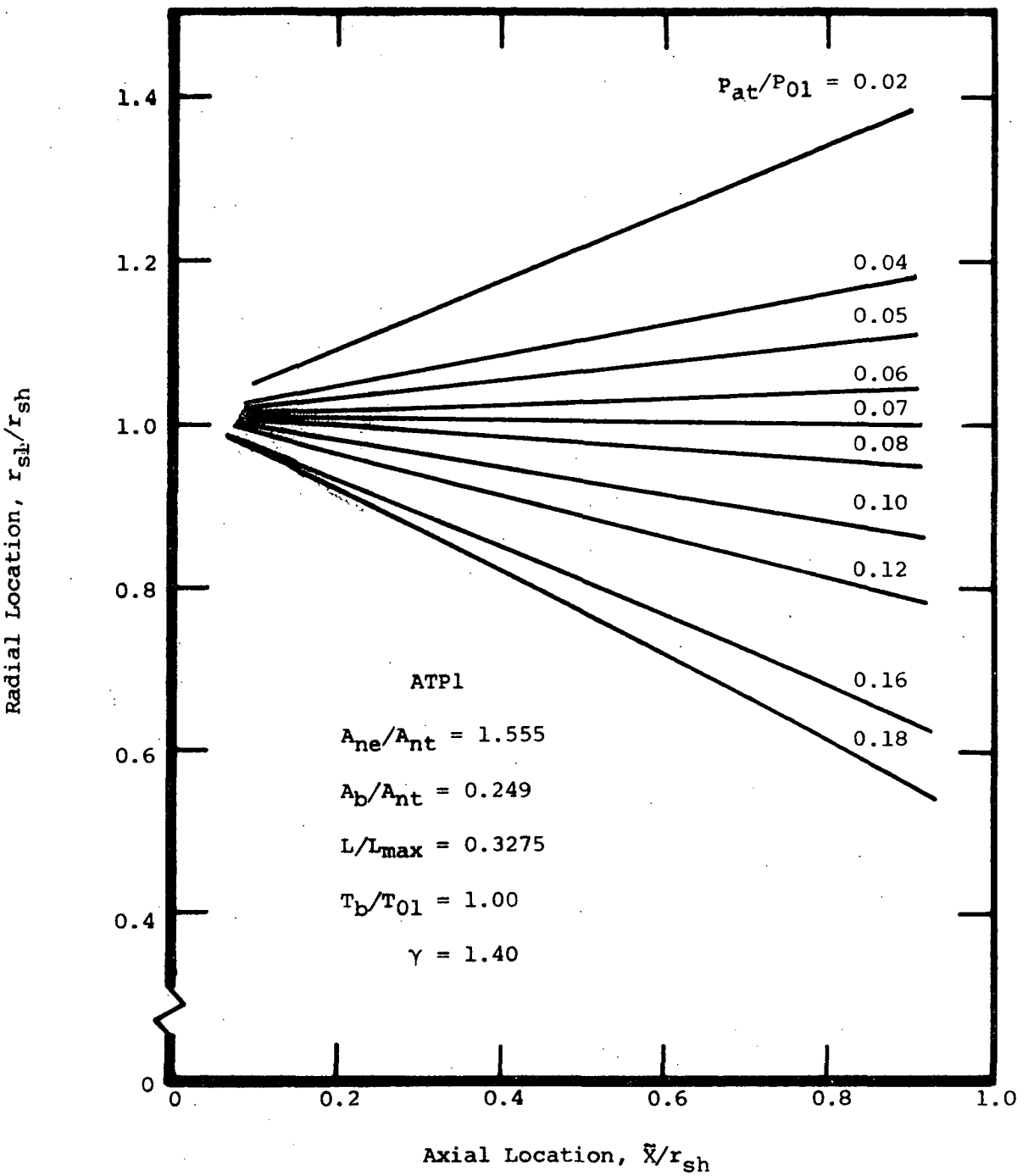

Fig. 41 Effect of Ambient Pressure Ratio on the Internal Shock Wave Location for an Axisymmetric T-P Nozzle with a 10^{o} conical Plug.

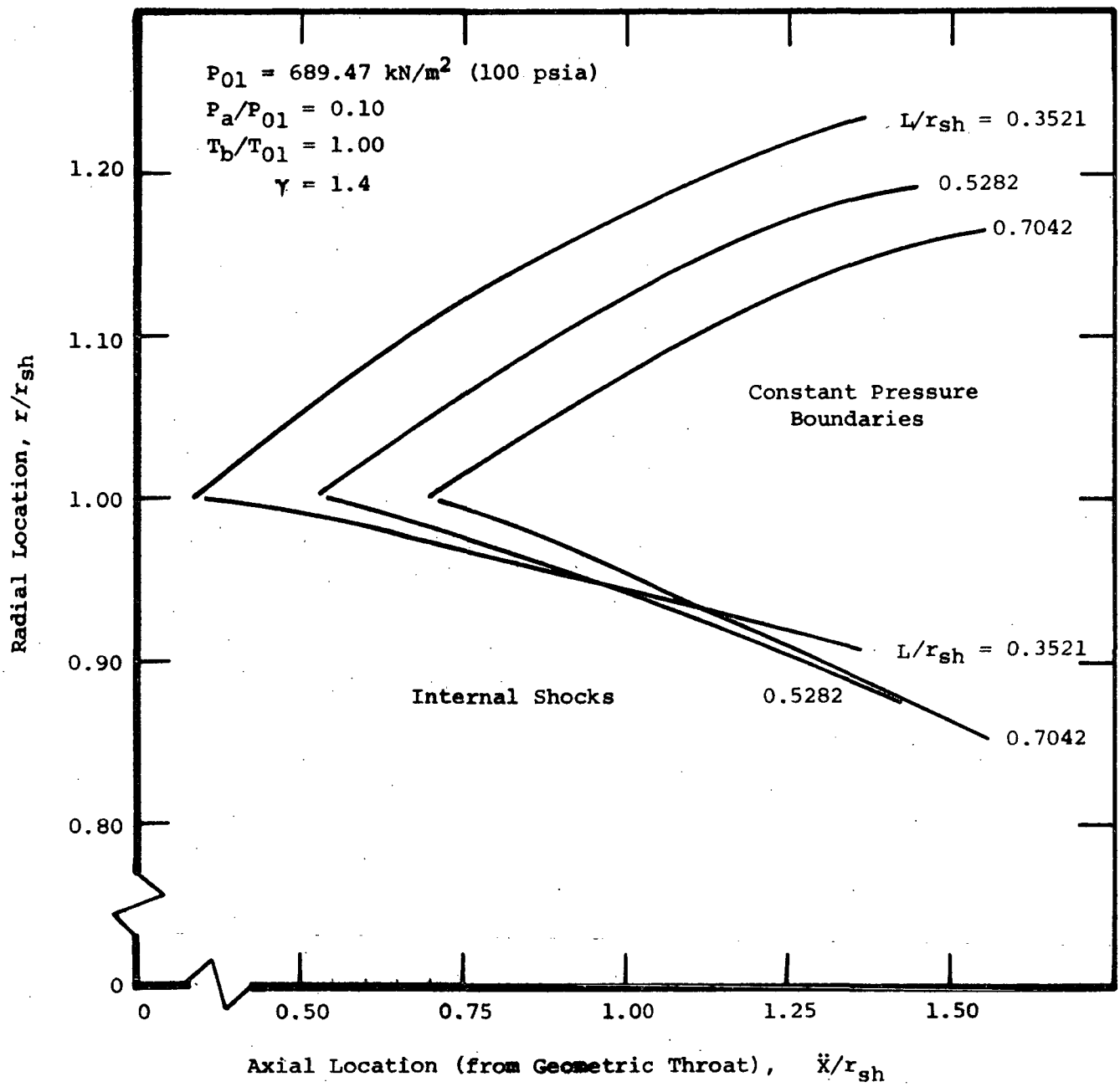

Fig. 42 Effect of Shroud Length on Constant Pressure Boundary and Internal Shock Locations (A_e/A_{nt} = 1.688, L/L_{max} = 0.2512, α = 10.0°).

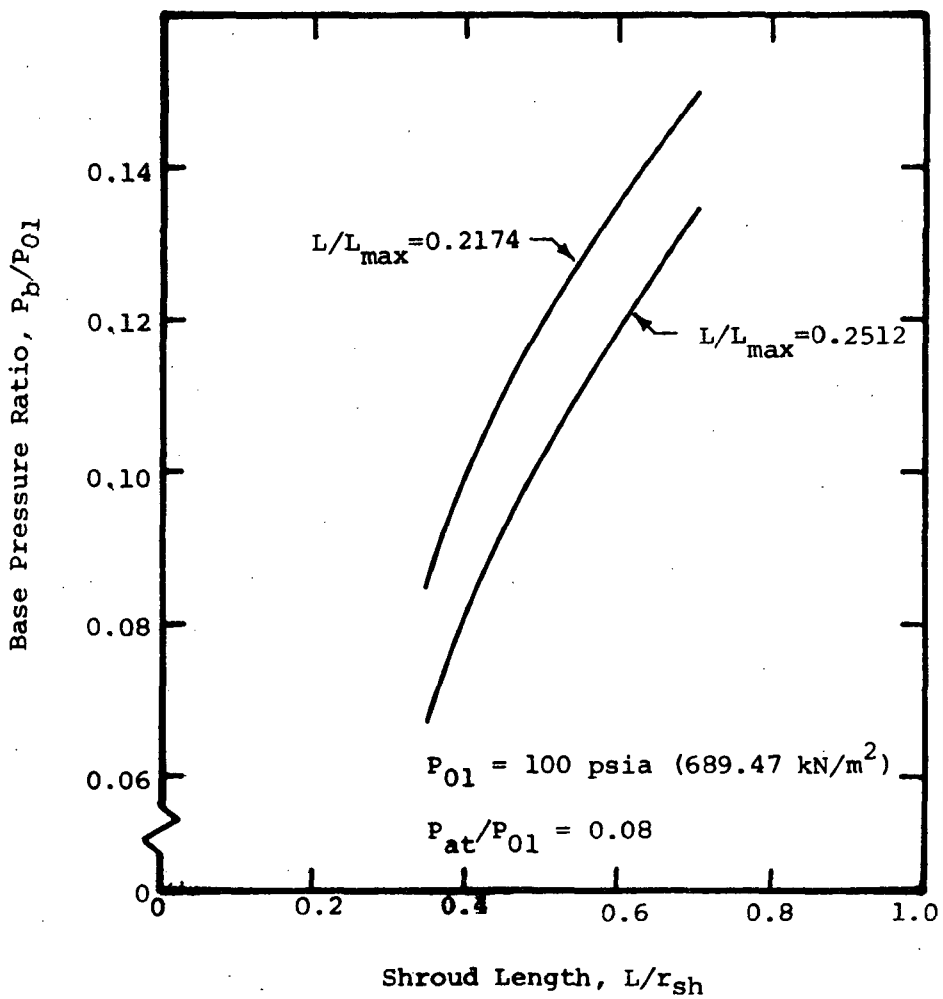

Fig. 43 Effect of Shroud Length on Base Pressure for Axisymmetric T-P Nozzle ATP2 with L/L_{max} = 0.2512.

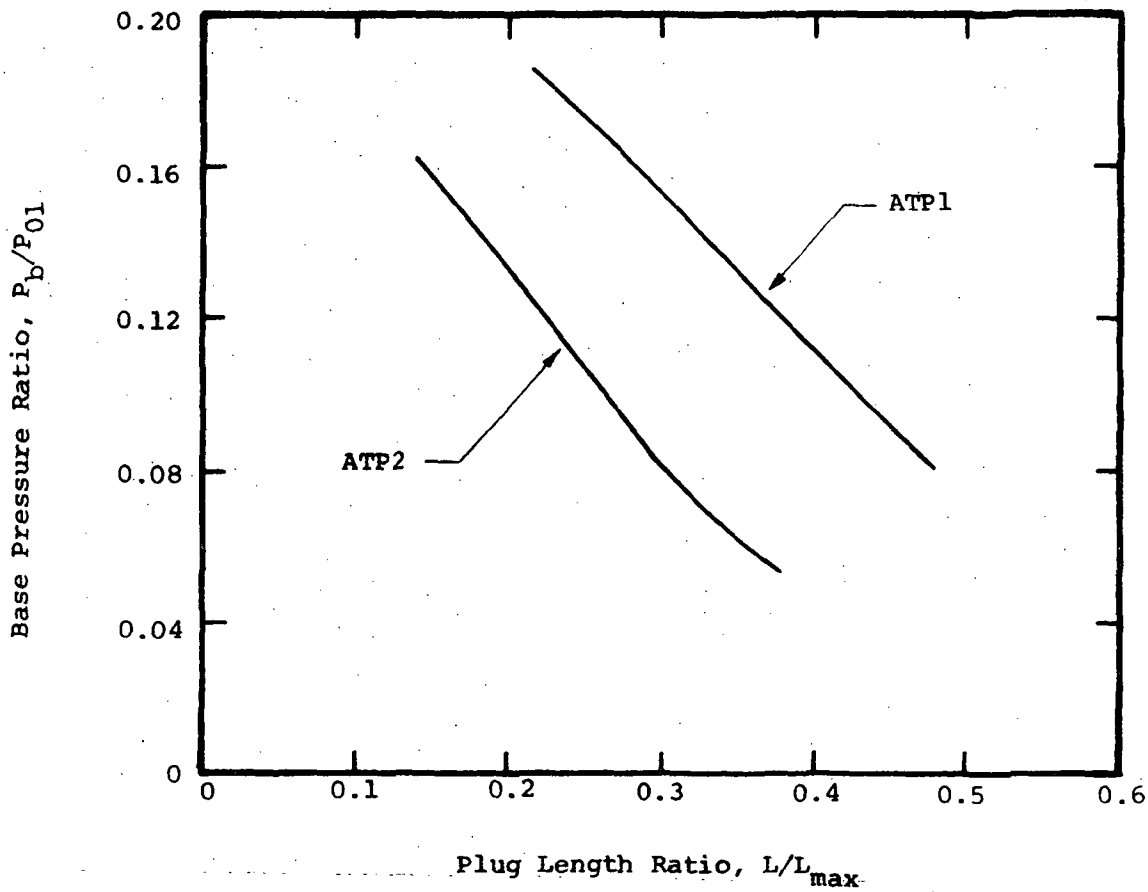

Fig. 44 Analytical Variation of Base Pressure Ratio with Plug Length Ratio.

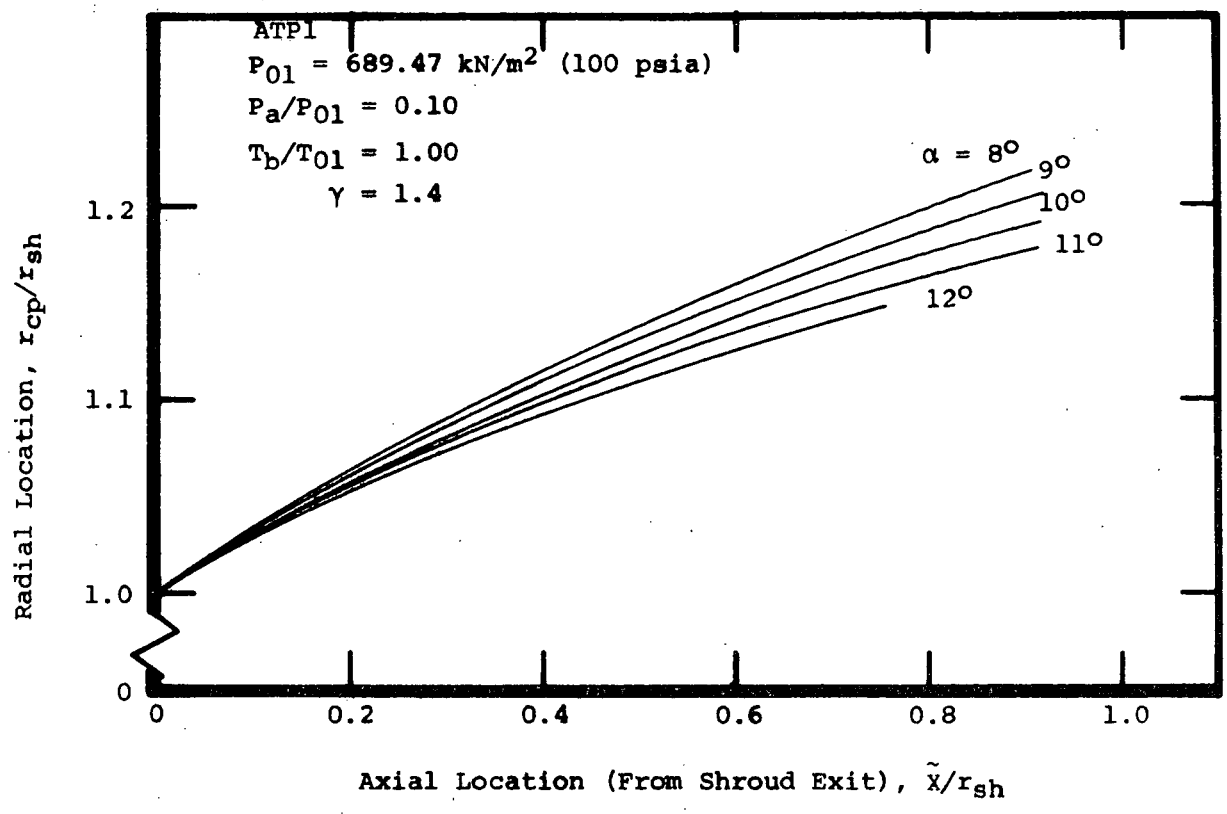

a) Constant Pressure Boundary Location

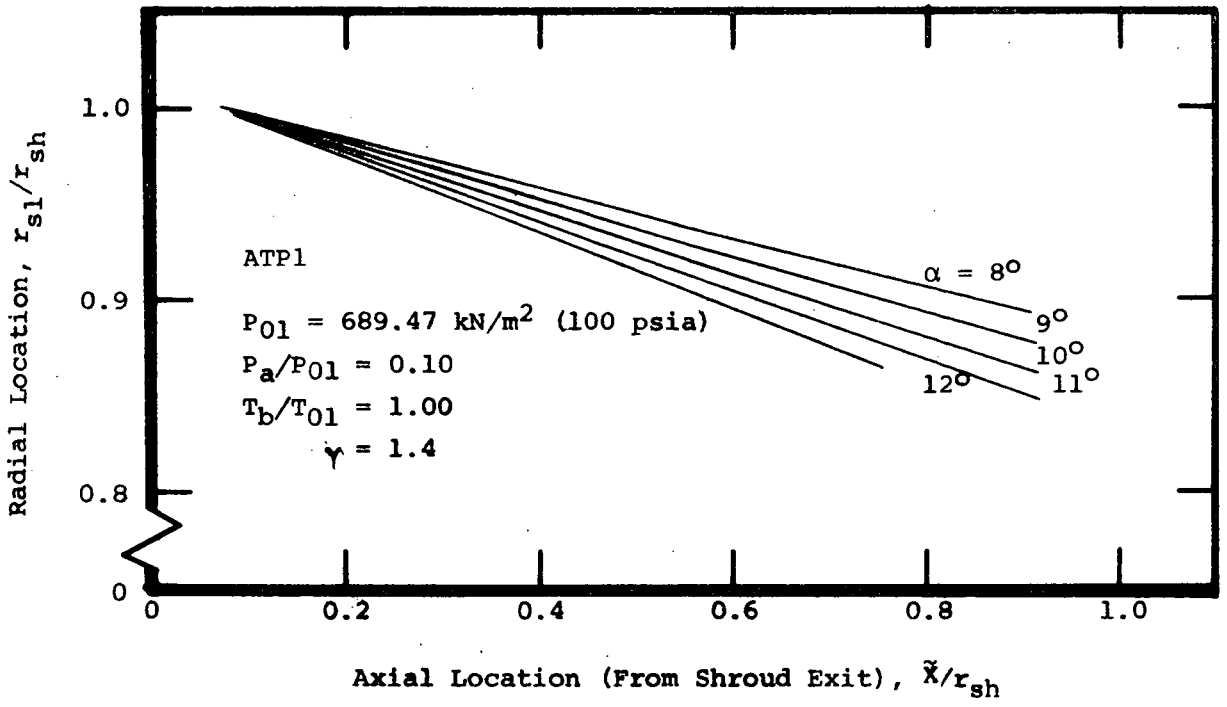

b) Internal Shock Wave Location

Fig. 45 Effect of Plug Angle on Inviscid Flow for Axisymmetric Truncated Plug Nozzle (A_e/A_{nt} = 1.555, L/L_{max} = 0.3275).

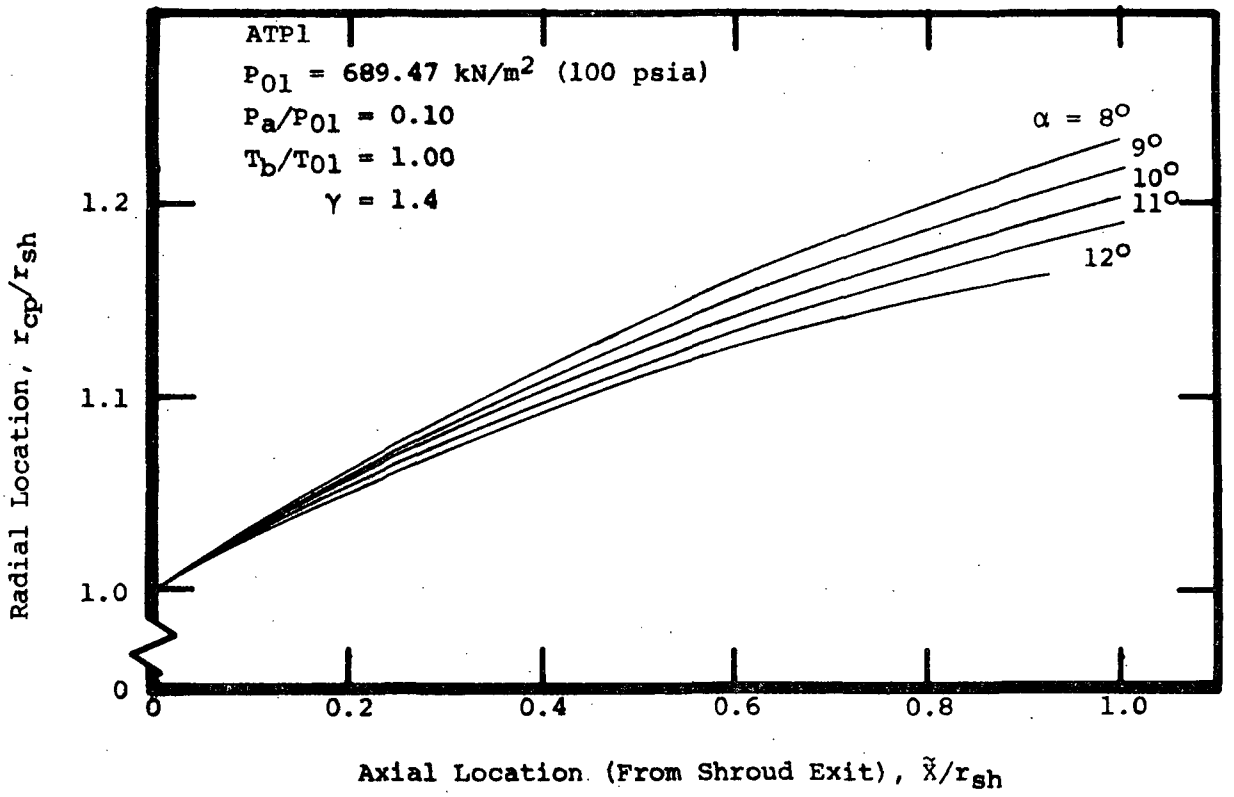

a) Constant Pressure Boundary Location

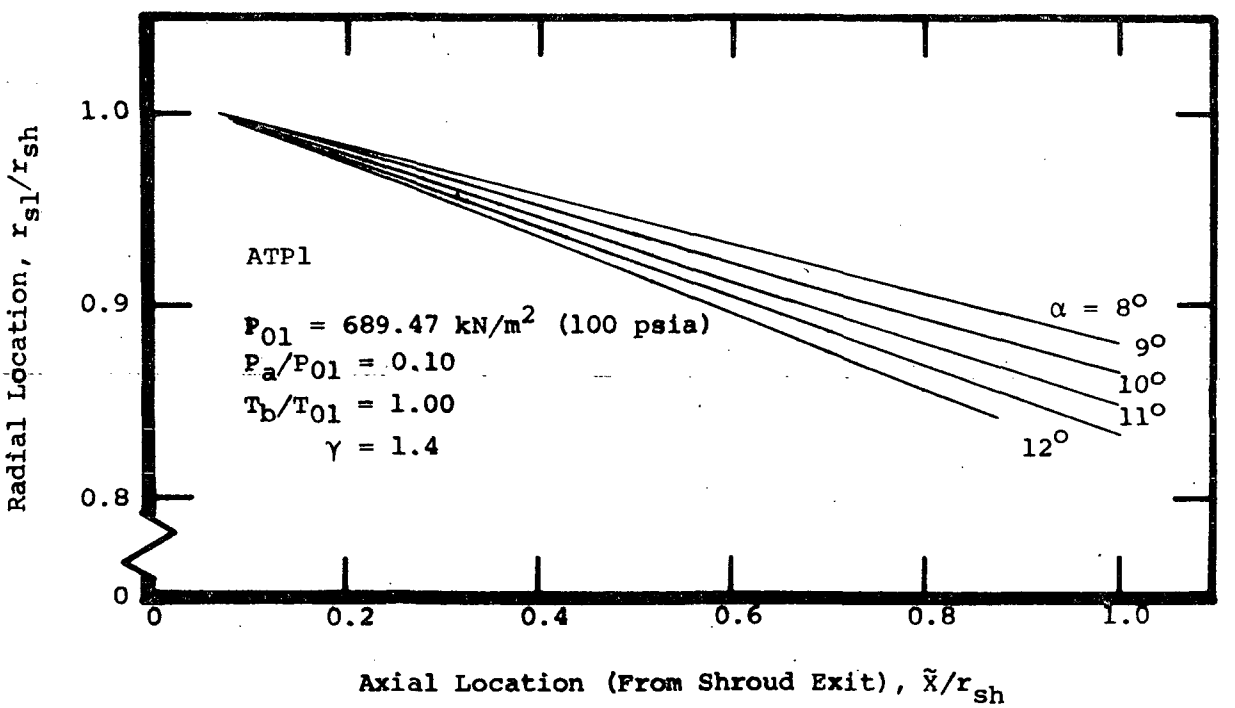

b) Internal Shock Wave Location

Fig. 46 Effect of Plug Angle on Inviscid Flow for Axisymmetric Truncated Plug Nozzle (A_e/A_{nt} = 1.555, L/L_{max} = 0.3785).

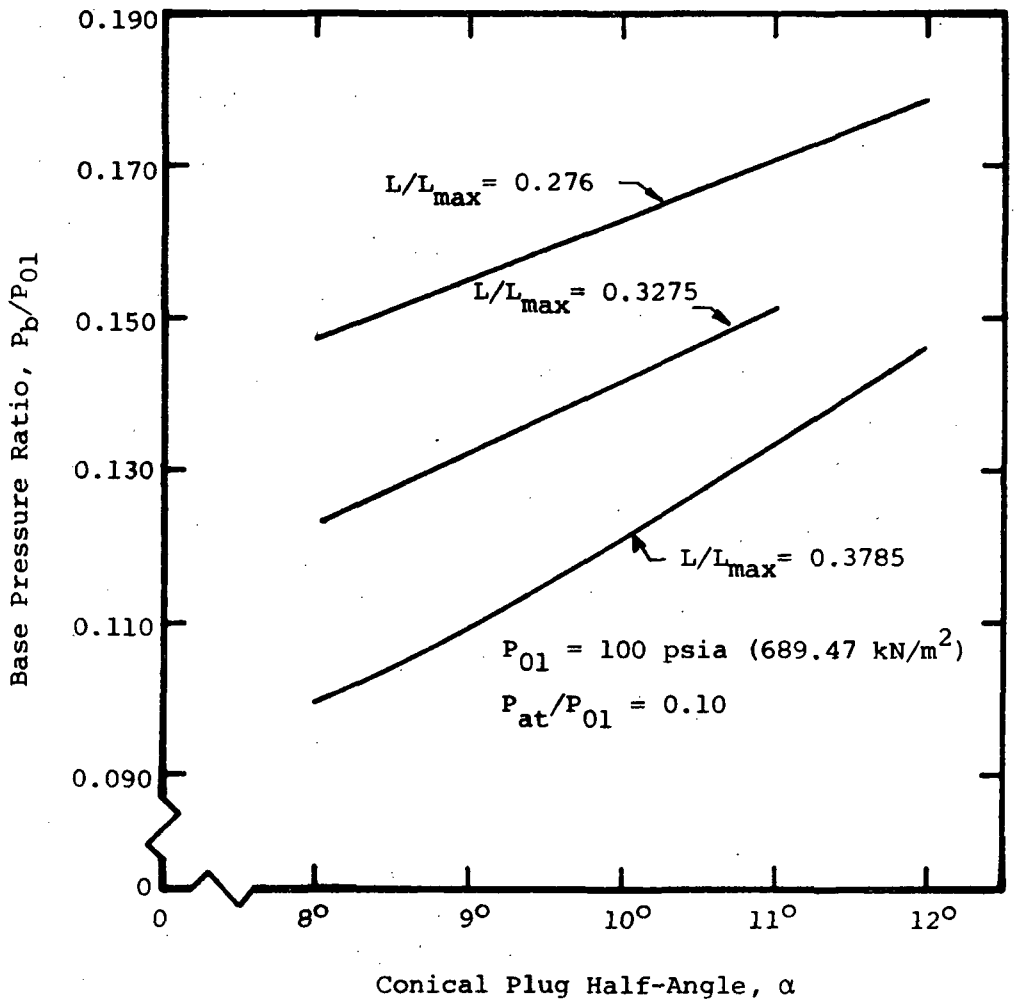

Fig. 47 Effect of Plug Angle on Base Pressure Ratio for Axisymmetric Truncated Plug Nozzle ATP1.

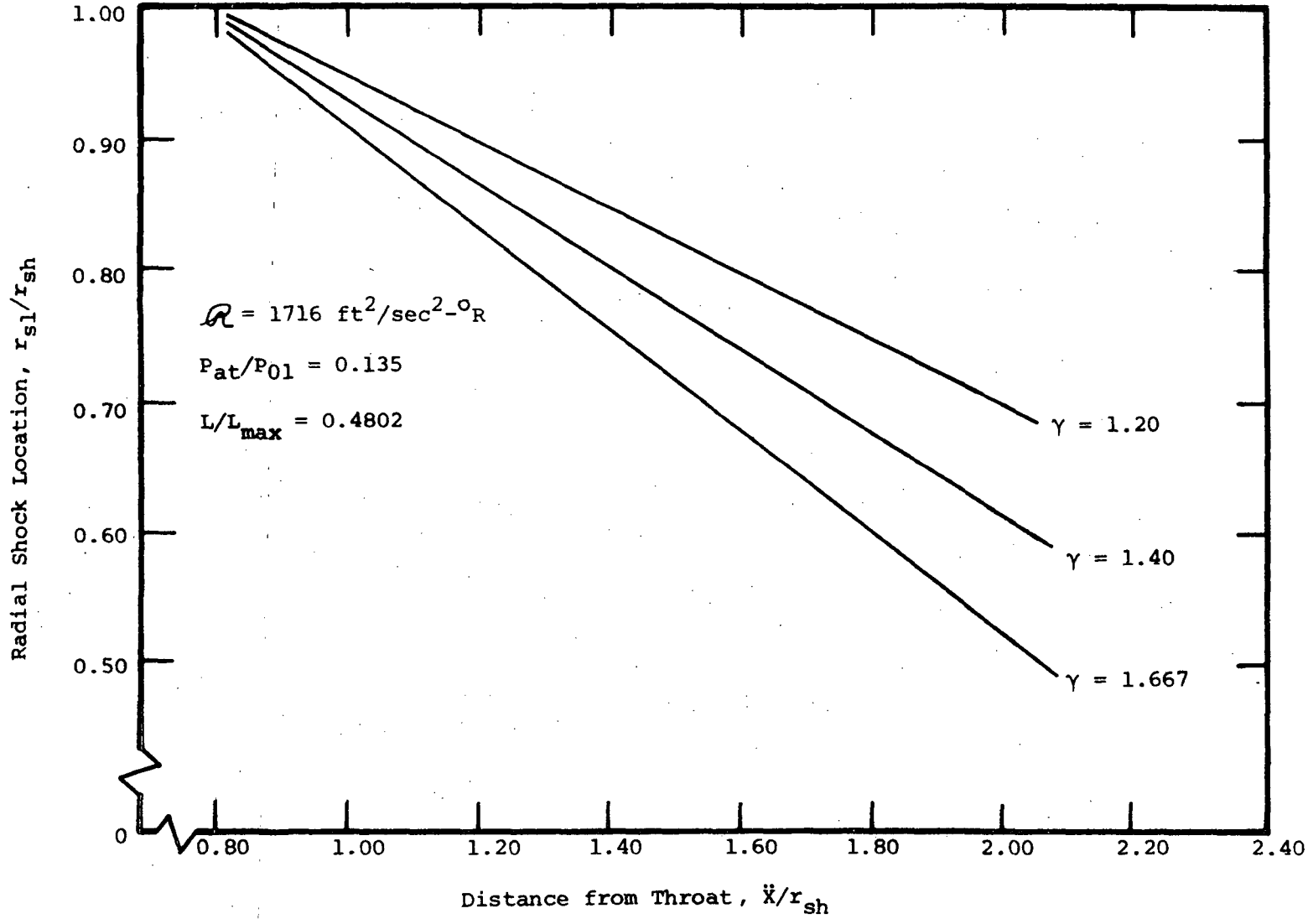

Fig. 48 Effect of Ratio of Specific Heats on the Internal Shock Wave Location for Axisymmetric T-P Nozzle ATP1.

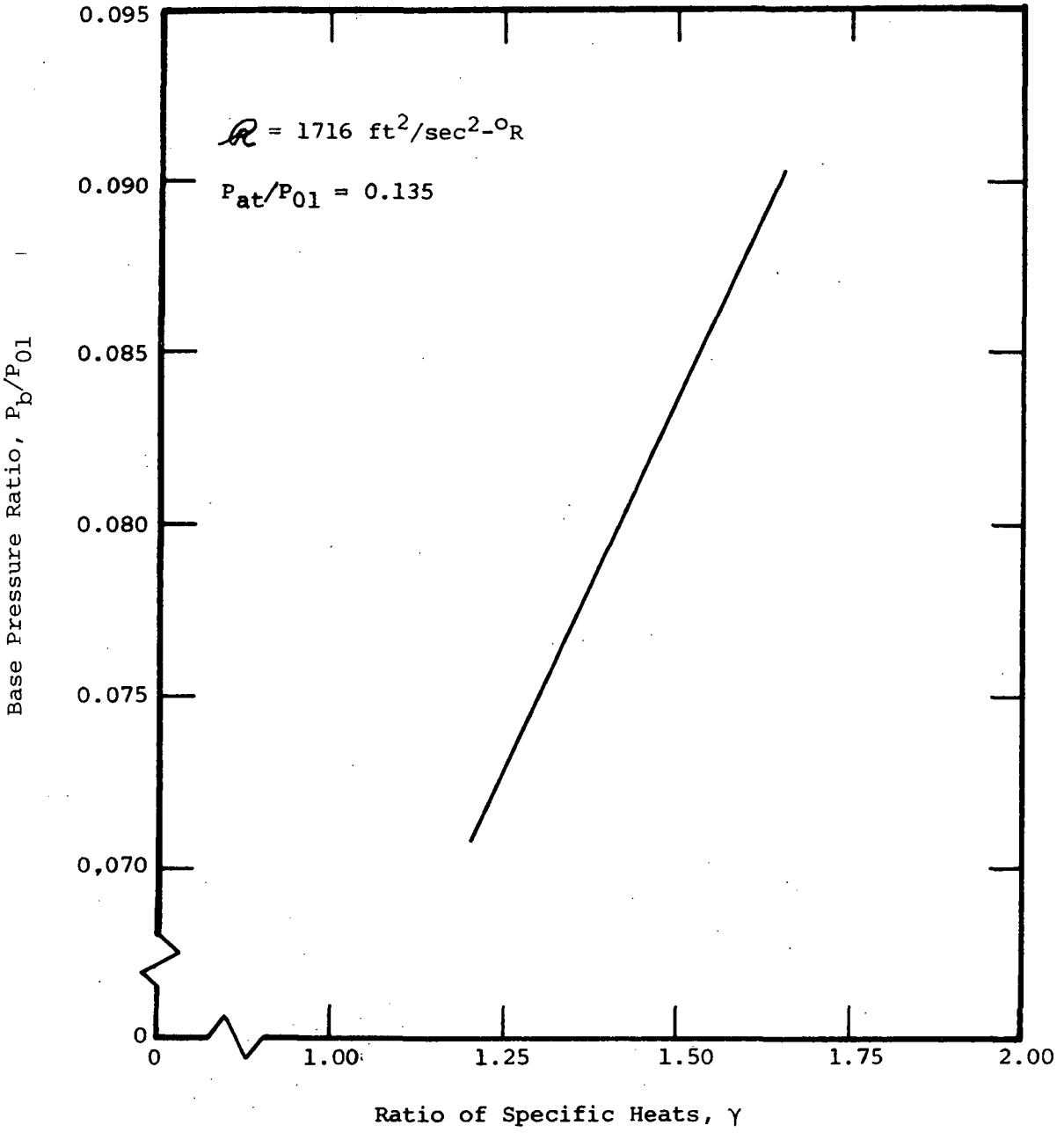

Fig. 49 Effect of Ratio of Specific Heats on the Base Pressure Ratio for Axisymmetric T-P Nozzle ATP1.

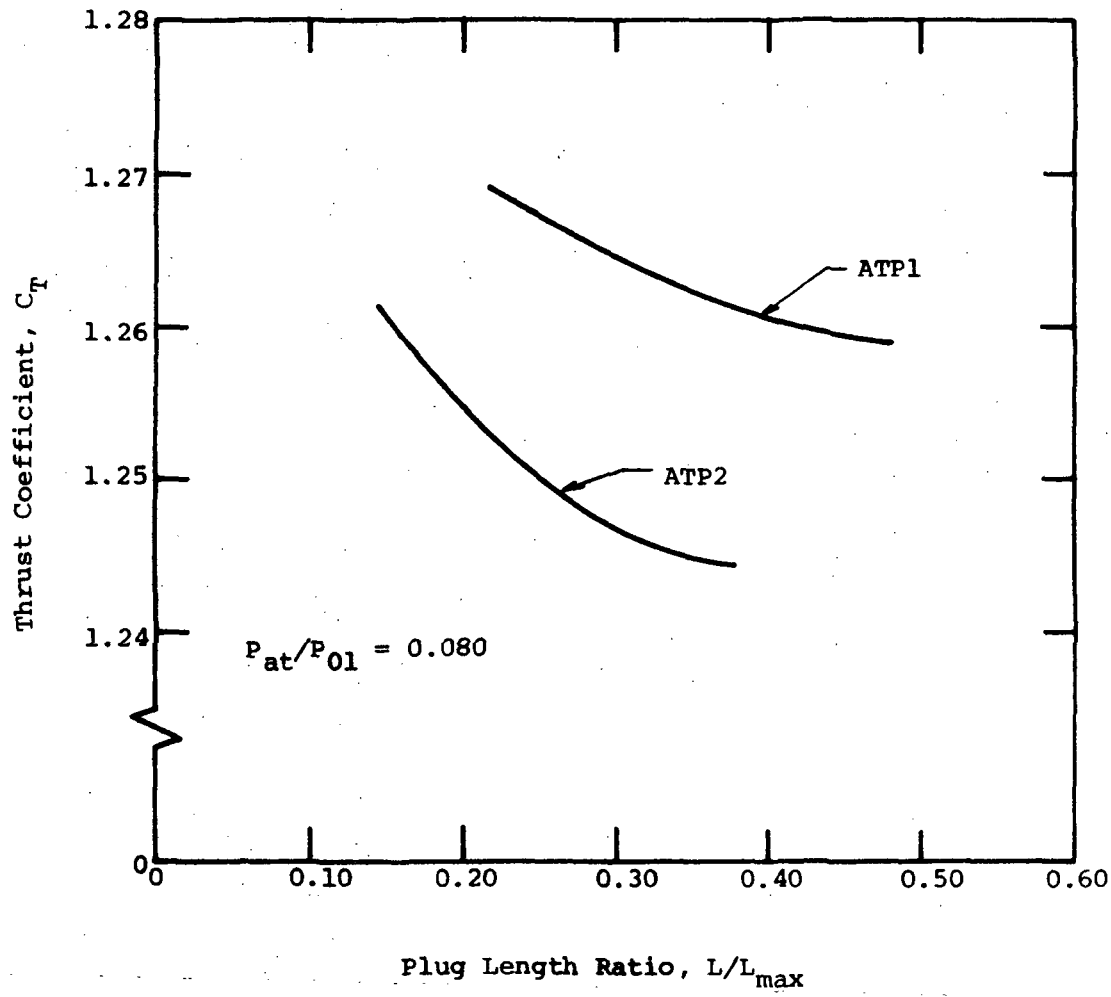

Fig. 50 Static Thrust Performance versus Plug Length Ratio for "Closed Wake" Operation.

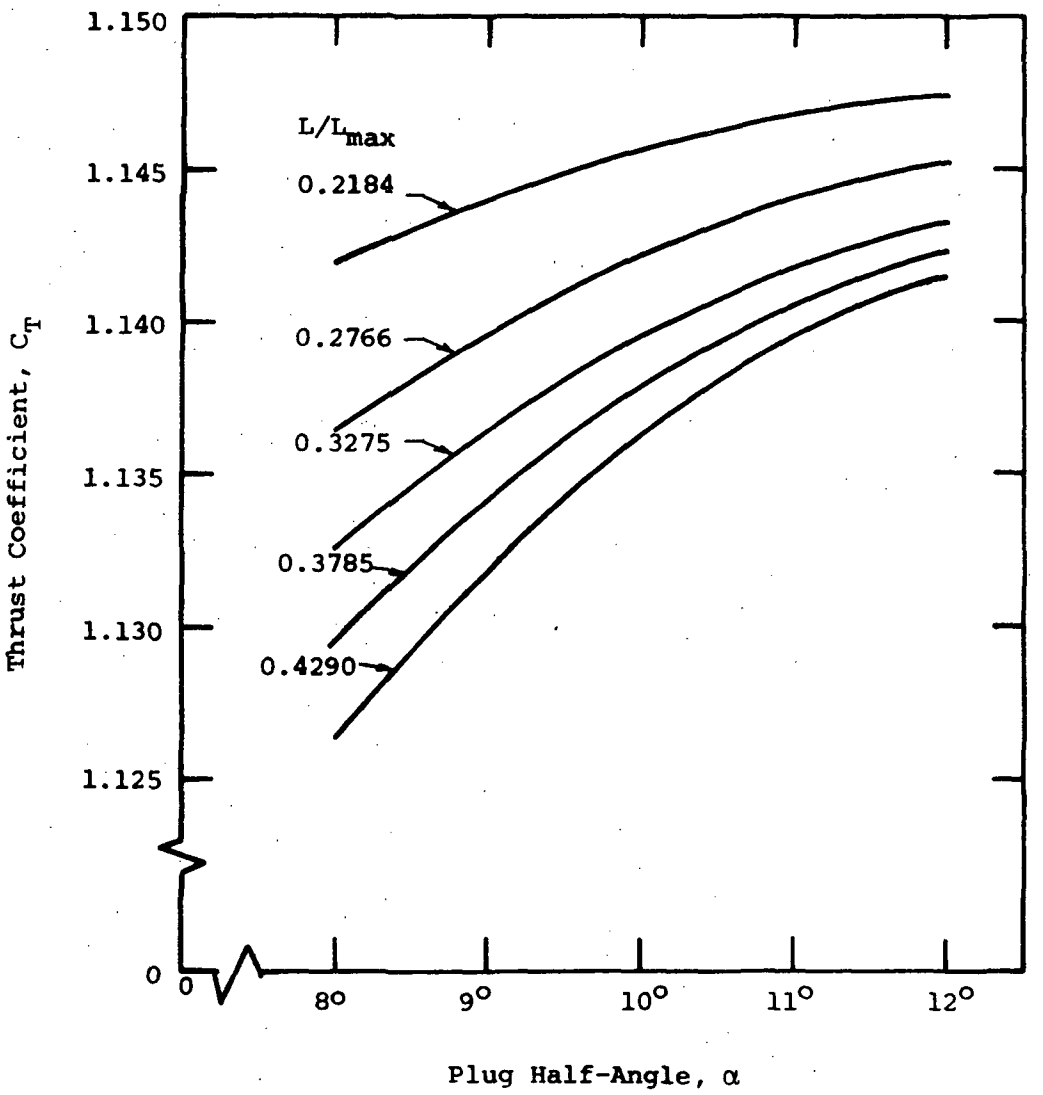

Fig. 51 Static Thrust Performance versus Plug Half-Angle for ATP1 and "Closed Wake" Operation.

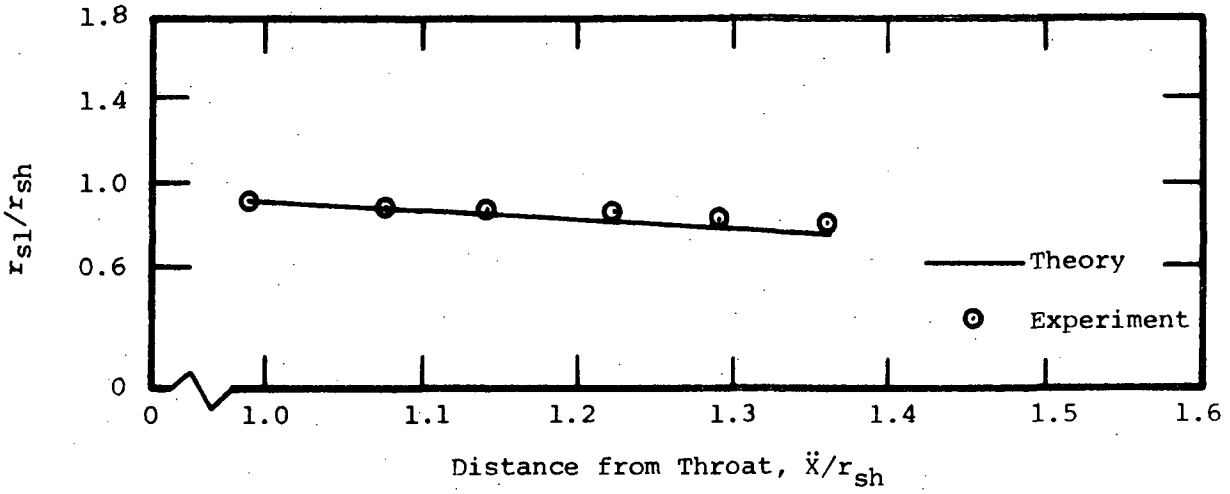

a) $P_{at}/P_{01} = 0.120$

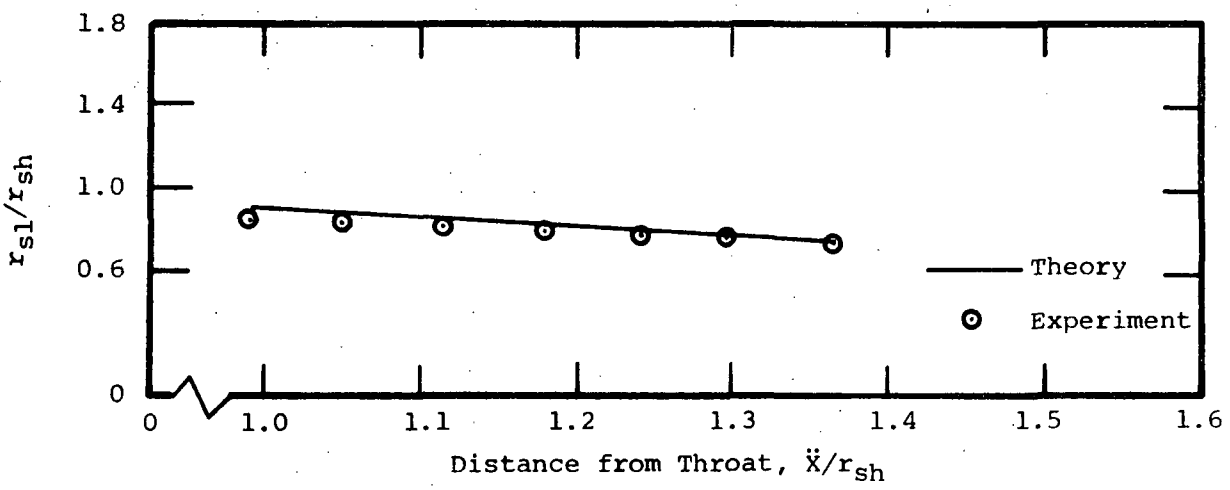

b) $P_{at}/P_{01} = 0.160$

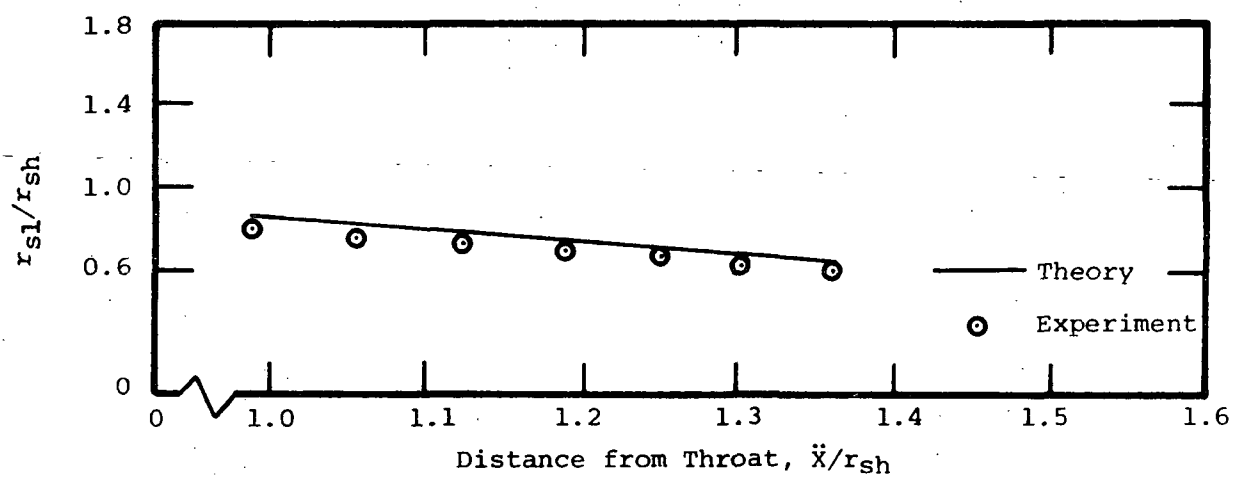

c) $P_{at}/P_{01} = 0.200$

Fig. 52 Comparison between Analytical and Experimental Internal Shock Wave Location for ATP1 (L/L_{max}=0.2327, Shroud Exit at $\ddot{X}/r_{sh}$=0.742).

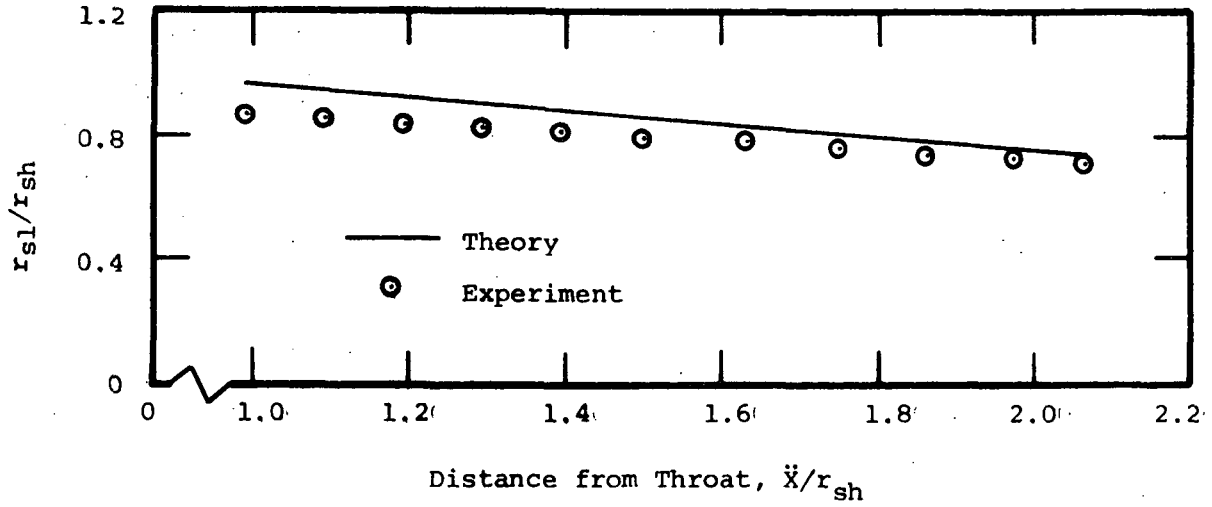

a) $P_{at}/P_{01} = 0.110$

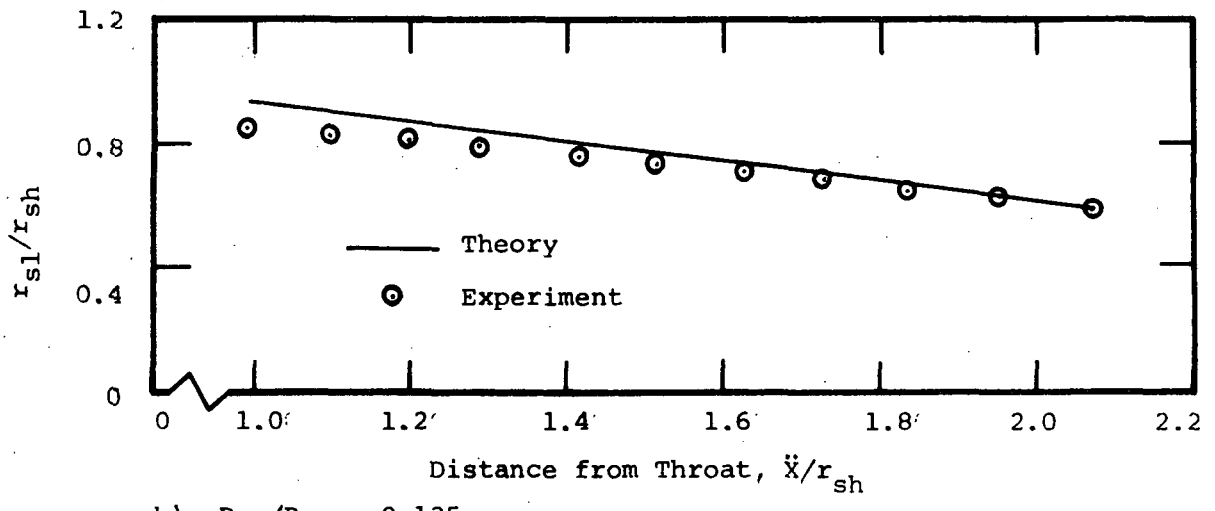

b) $P_{at}/P_{01} = 0.135$

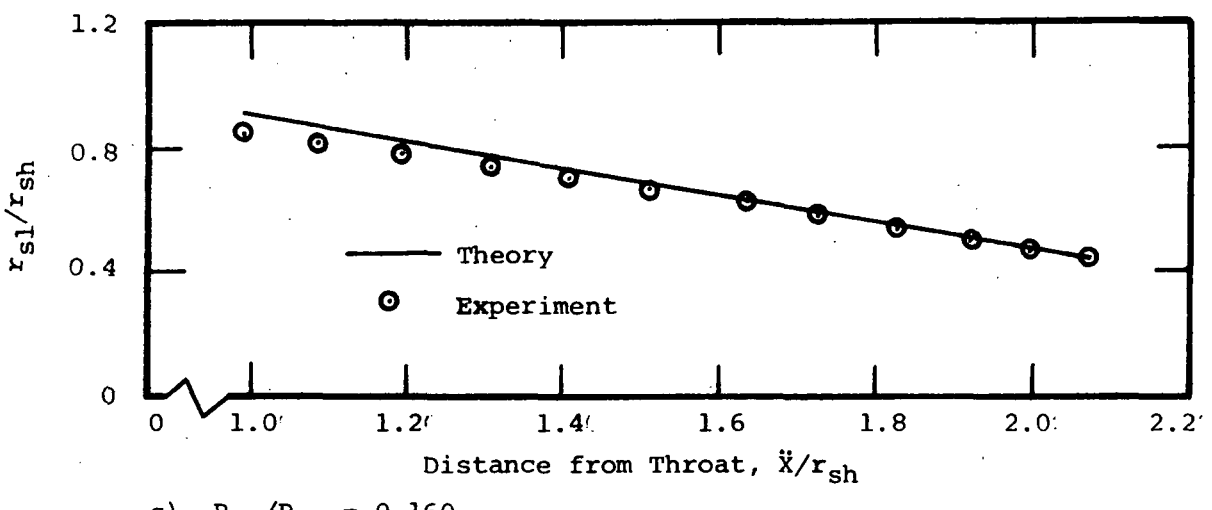

c) $P_{at}/P_{01} = 0.160$

Fig. 53 Comparison between Analytical and Experimental Internal Shock Wave Location for ATP1 (L/L_{max}=0.4802, Shroud Exit at $\ddot{X}/r_{sh}$=0.742).

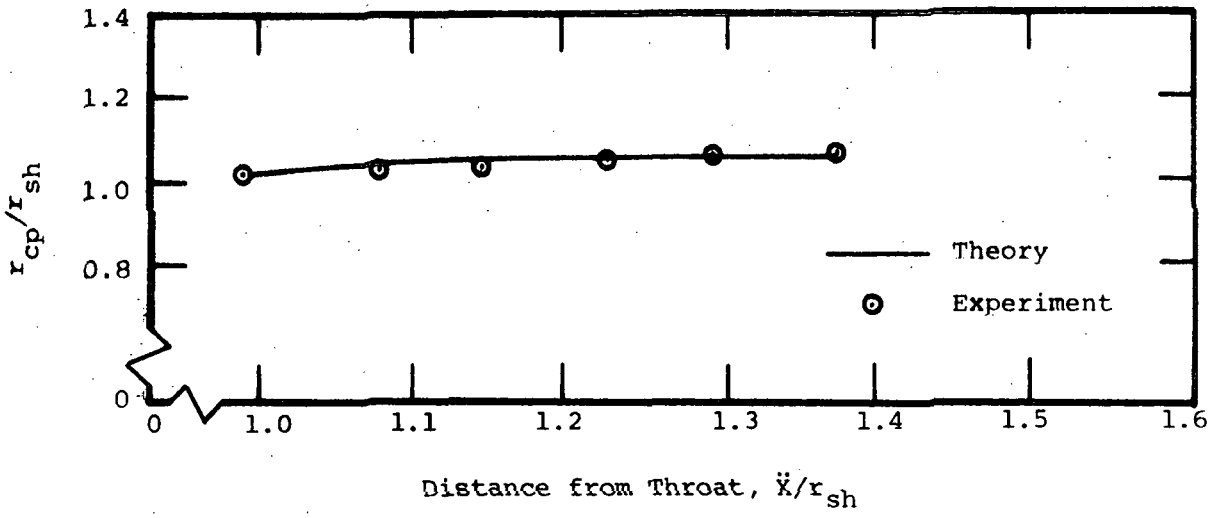

a) $P_{at}/P_{01} = 0.120$

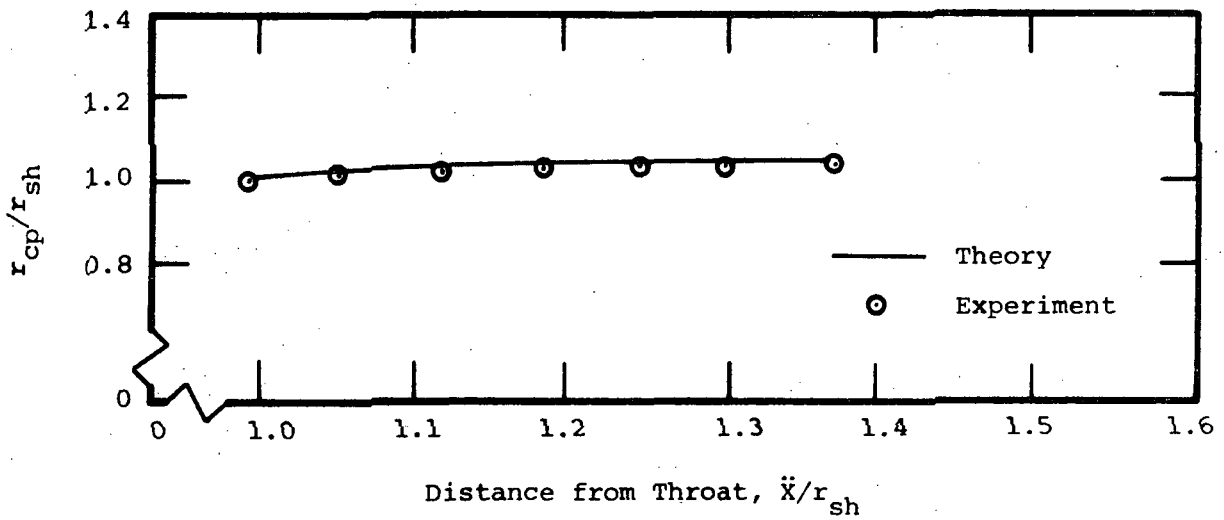

b) $P_{at}/P_{01} = 0.160$

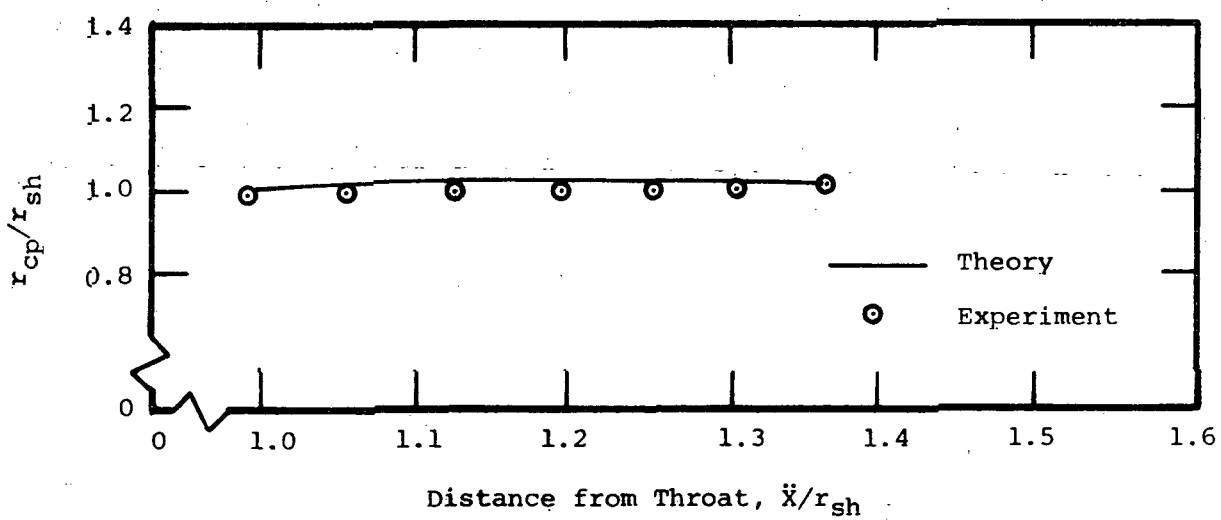

c) $P_{at}/P_{01} = 0.200$

Fig. 54 Comparison between Analytical and Experimental Constant Pressure Boundary Location for ATP1 (L/L_{max}=0.2327, Shroud Exit at $\ddot{X}/r_{sh}$=0.742).

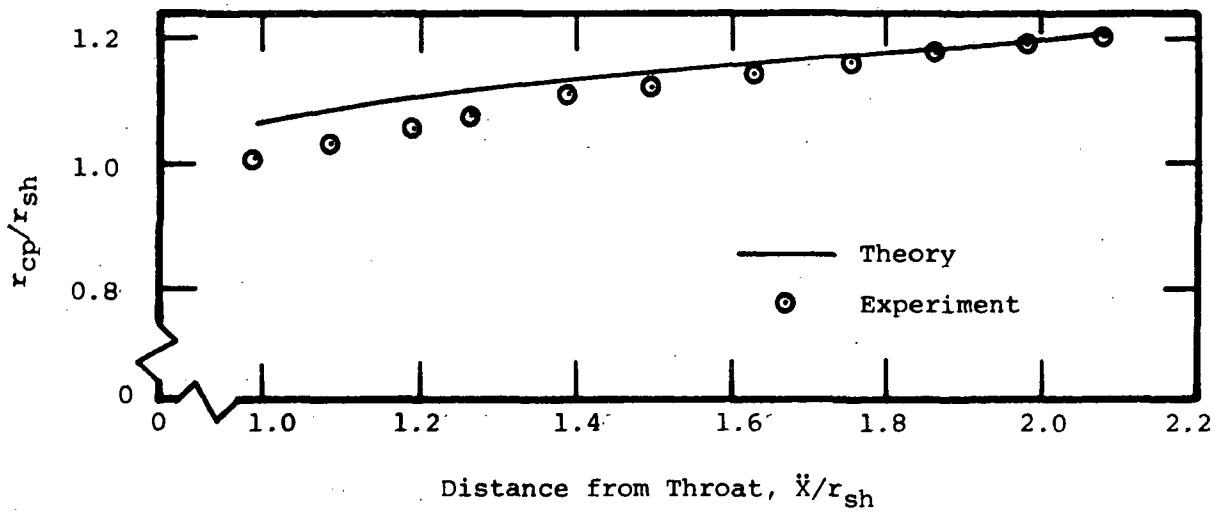

a) $P_{at}/P_{01} = 0.110$

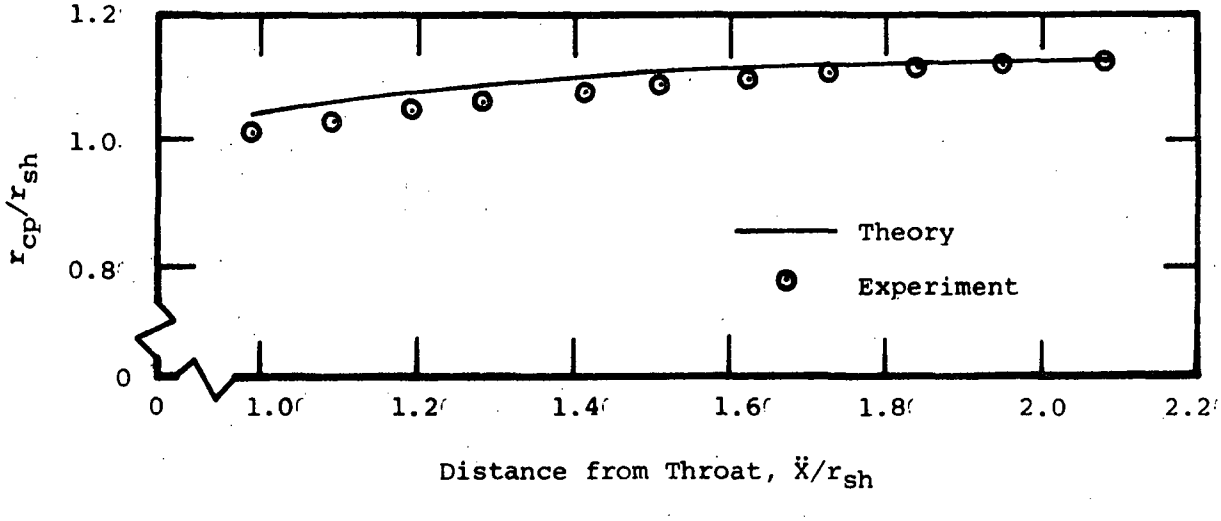

b) $P_{at}/P_{01} = 0.135$

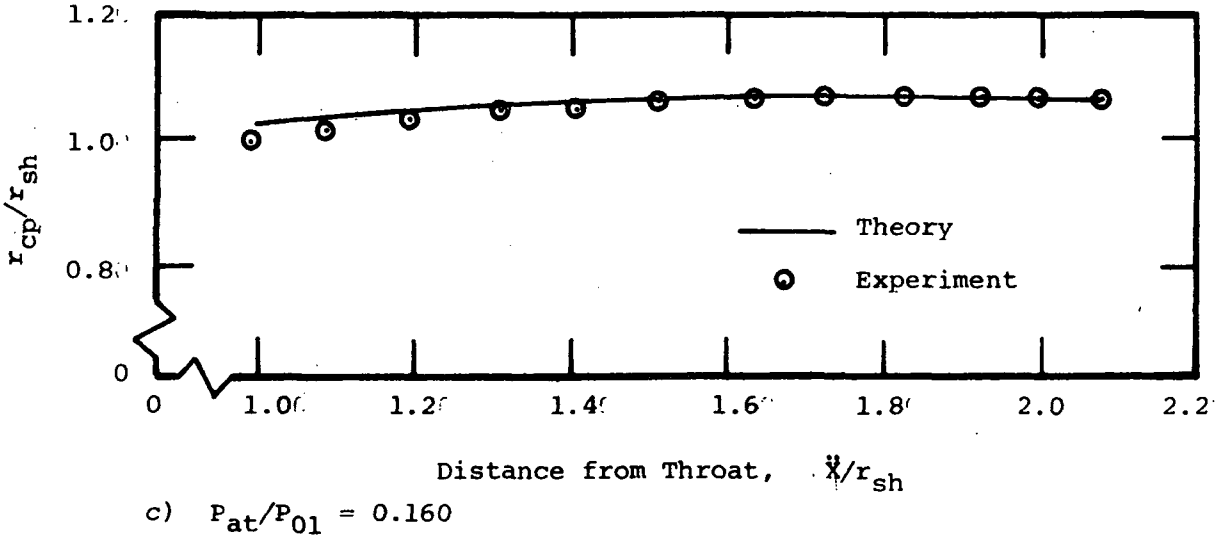

c) $P_{at}/P_{01} = 0.160$

Fig. 55 Comparison between Analytical and Experimental Constant Pressure Boundary Location for ATP1 (L/L_{max} = 0.4802, Shroud Exit at $\ddot{X}/r_{sh}$=0.742).

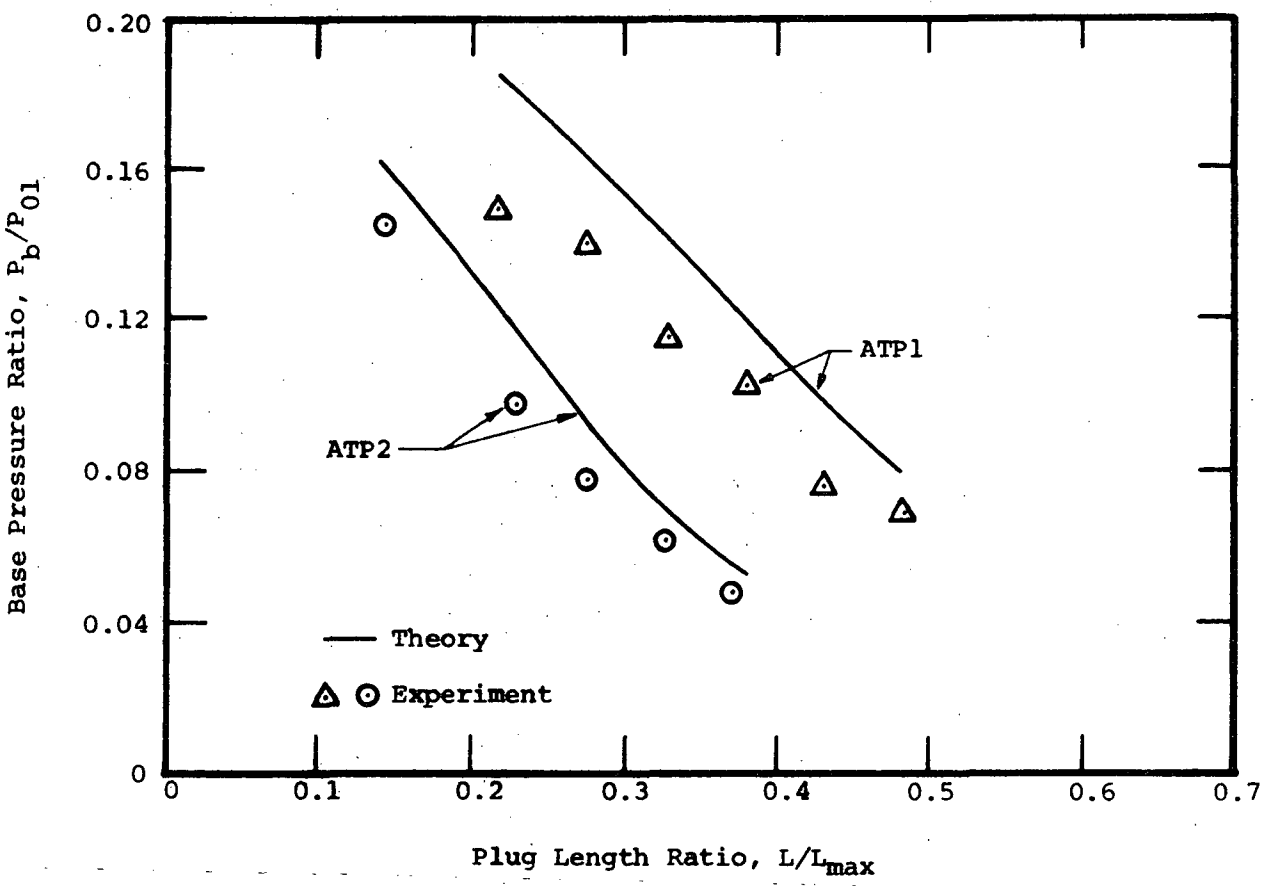

Fig. 56 Comparison of Analytical and Experimental Variations of Base Pressure Ratio with Plug Length Ratio.

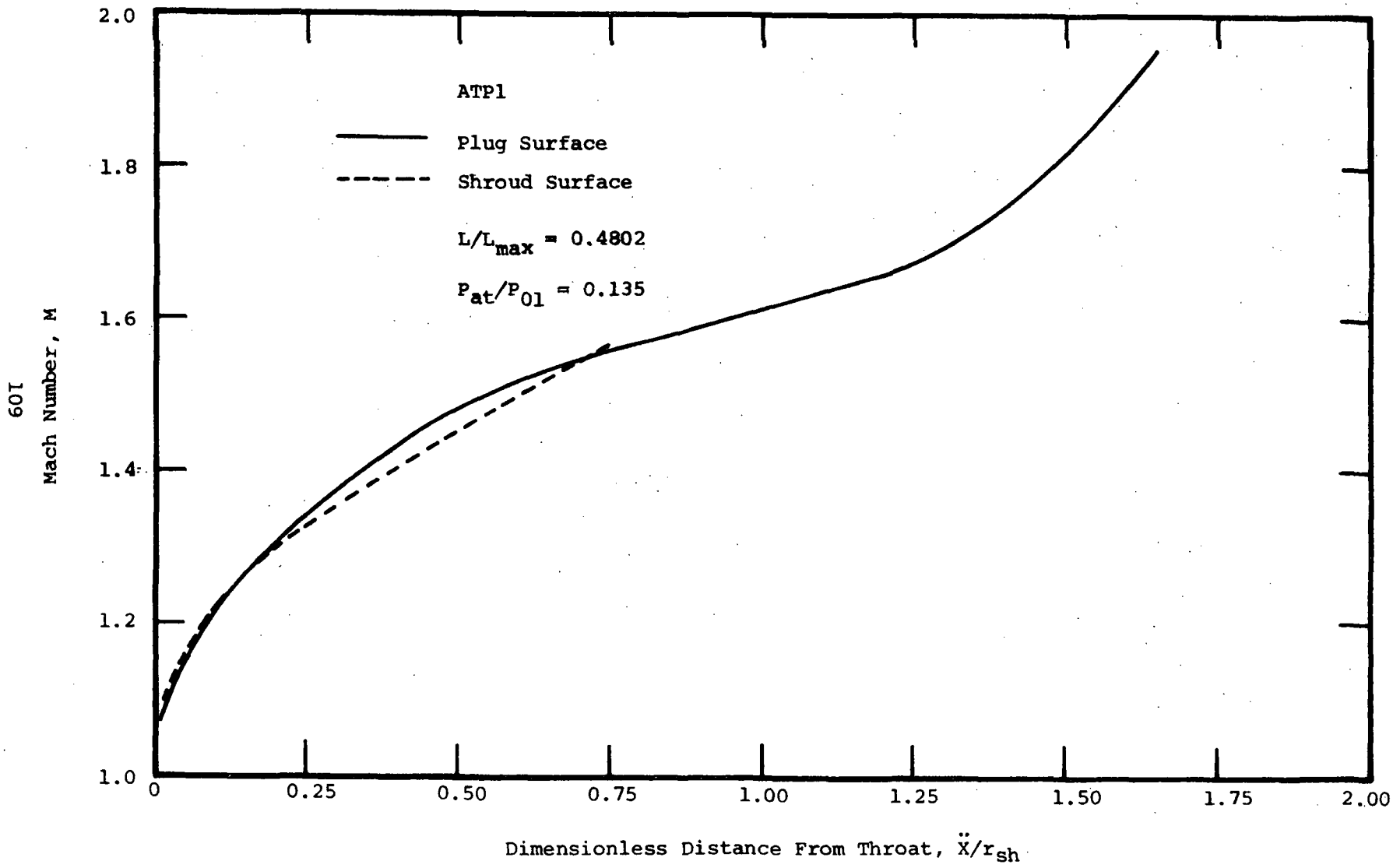

Fig. 57 Analytical Mach Number Distributions for Axisymmetric Truncated Plug Nozzle ATP1.

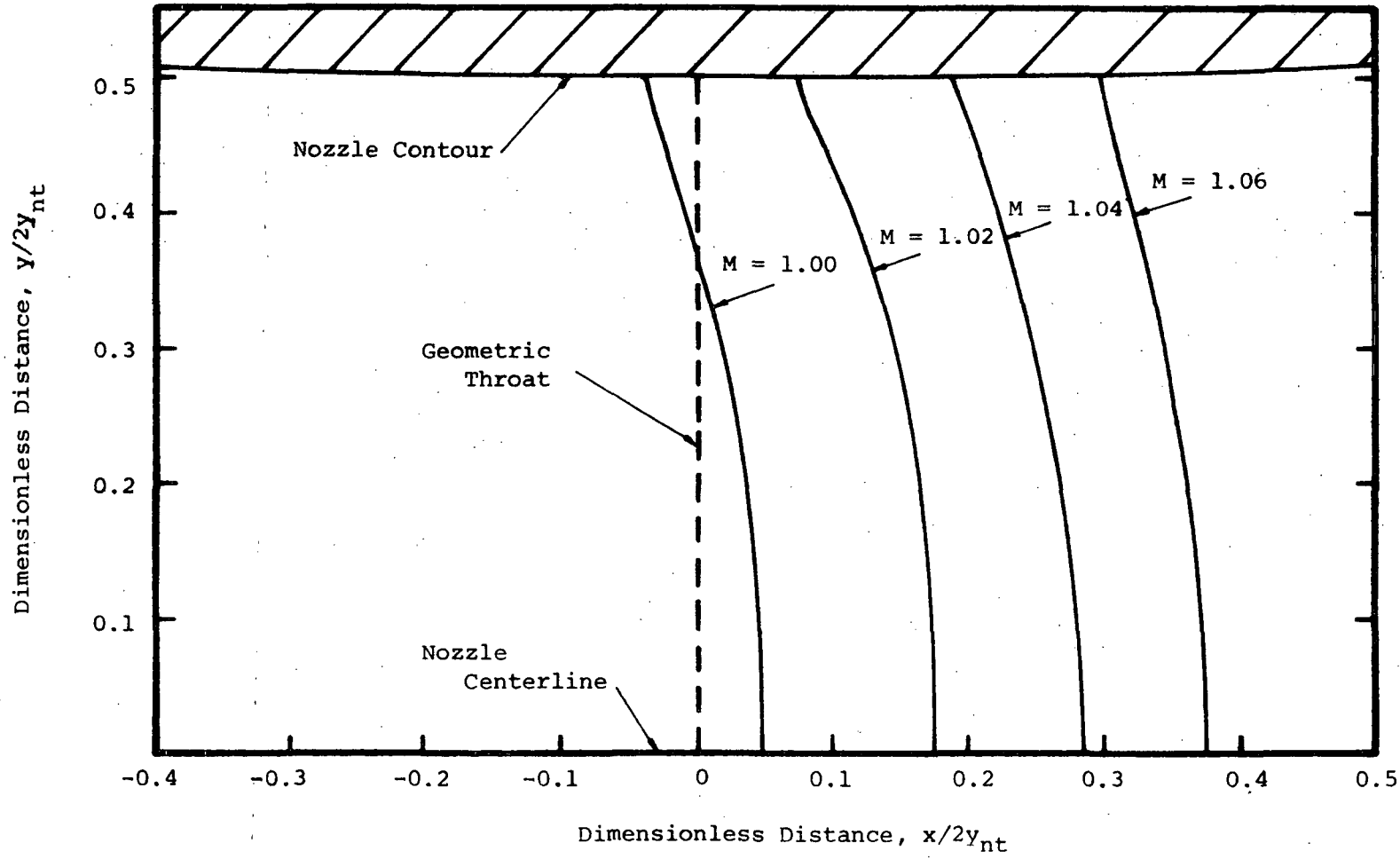

Fig. 58 Calculated Sonic Line for Transonic Nozzle Section PLTR1.

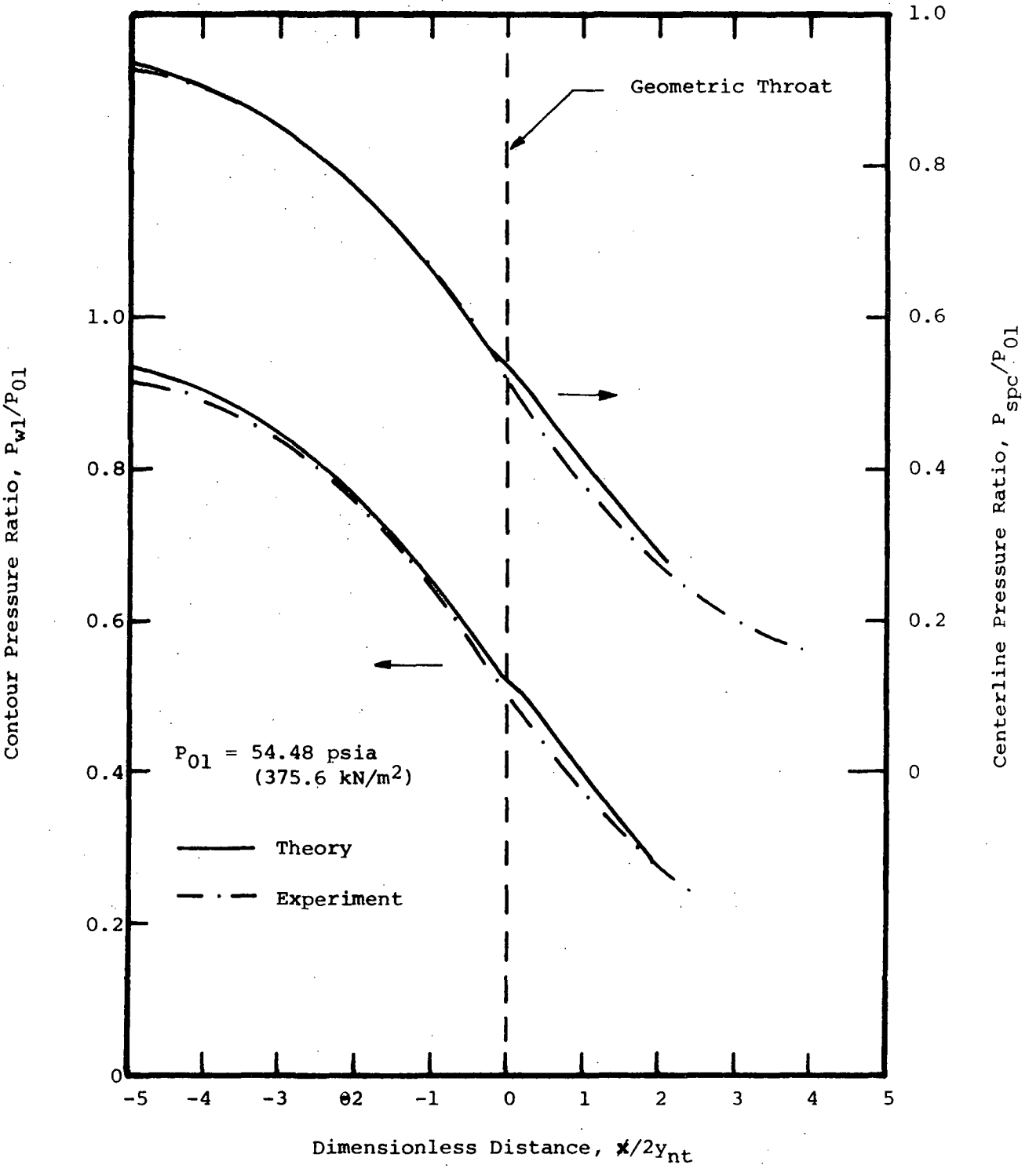

Fig. 59 Comparison of Theoretical and Experimental Static Pressure Ratios along Nozzle Contour and Centerline for PLTR1.

DISTRIBUTION LIST

COPIES	RECIPIENT	DESIGNEE
	Ames Research Center NASA Moffett Field, California 94035	
1	A.S. Hertzon, Director of Procurement	(X)
	Patents and Contracts Management	(X)
	Jet Propulsion Laboratory 4800 Oak Grove Dr. Pasadena, Calif. 91103	
1	Mr. Hartwell R. Long (Technical Manager)	(X)
1	Chief, Liquid Propulsion Technology RPL Office of Advanced Research and Technology NASA Headquarters Washington, D.C., 20546	(X)
1	Director, Technology Utilization Division Office of Technology Utilization NASA Headquarters Washington, D. C. 20546	(X)
20	NASA Scientific and Technical Information Facility P.O. Box 33 College Park, Maryland 20740	(X)
1	Director, Launch Vehicles and Propulsion, SV Office of Space Science and Applications NASA Headquarters Washington, D.C. 20546	(X)
1	Director, Advanced Manned Missions, MT Office of Manned Space Flight NASA Headquarters Washington, D.C. 20546	(X)
1	Mission Analysis Division NASA Ames Research Center Moffett Field, California 24035	(X)

NASA FIELD CENTERS

1	Ames Research Center Moffett Field, California 94035	Hans M. Mark V.D. Reed
1	Goddard Space Flight Center Greenbelt, Maryland 20771	Merland L. Moseson Code 620

NASA FIELD CENTERS

COPIES	RECIPIENT	DESIGNEE
1	Jet Propulsion Laboratory California Institute of Technology 4800 Oak Grove Drive Pasadena, California 91103	Henry Burlage, Jr. Propulsion Div. 38
1	Langley Research Center Langley Station Hampton, Virginia 23365	Ed. Cortwright, Director D.J. Carter P.K. Pierpont
1	Lewis Research Center 21000 Brookpark Road Cleveland, Ohio 44135	B.T. Lundin, Director Dr. H. Mark
1	Marshall Space Flight Center Huntsville, Alabama 35812	Hans G. Paul Code S&E-ASTN-P
1	Manned Spacecraft Center Houston, Texas 77001	J.G. Thibodaux, Jr. Chief, Prop. + Power Div. B. Redd
1	John F. Kennedy Space Center, NASA Cocoa Beach, Florida 32931	Dr. Kurt H. Debus

GOVERNMENT INSTALLATIONS

1	Aeronautical Systems Division Air Force Systems Command Wright-Patterson Air Force Base Dayton, Ohio 45433	D.L. Schmidt Code ASRCNC-2 V. Dahlem Code FDMG
1	Air Force Missile Development Center Holloman Air Force Base New Mexico 88330	
1	Air Force Missile Test Center Patrick Air Force Base, Florida	L.J. Ullian
1	Space and Missile Systems Organization Air Force Unit Post Office Los Angeles, California 90045	Col. Clark Technical Data Center Lt. J.F. Turk
1	Arnold Engineering Development Center Arnold Air Force Station Tullahoma, Tennessee 37388	Dr. H. K. Doetsch

GOVERNMENT INSTALLATIONS

COPIES	RECIPIENT	DESIGNEE
1	Bureau of Naval Weapons Department of the Navy Washington, D.C. 20546	J. Kay RTMS-41
1	Defense Documentation Center Hdqtrs. Cameron Station, Building 5 5010 Duke Street Alexandria, Virginia 22314 Attn: TISIA	
1	Headquarters, U.S. Air Force Washington, D.C. 20546	Col. C.K. Stambaugh AFRST
1	Picatinny Arsenal Dover, New Jersey 07801	I. Forsten, Chief Liquid Propulsion Laboratory
1	Air Force Rocket Propulsion Laboratory Research and Technology Division Air Force Systems Command Edwards, California 93523	RPRPD/Mr. H. Main Dr. L. Quinn C.H. Allen
1	U.S. Army Missile Command Redstone Arsenal Alabama 35809	Mr. Walter Wharton Dr. S.P.D. Smith
1	U.S. Naval Ordnance Test Station China Lake California 93557	Code 4562 Chief, Missile Propulsion Div.

CPIA

5	Chemical Propulsion Information Agency Applied Physics Laboratory 8621 Georgia Avenue Silver Spring, Maryland 20910	Tom Reedy T.M. Gilliland

INDUSTRY CONTRACTORS

1	Aerojet-General Corporation P.O. Box 296 Azusa, California 91703	W.L. Rogers
1	Aerojet-General Corporation P.O. Box 1947 Technical Library, Bldg. 2015, Dept. 2410 Sacramento, California 95809	R. Stiff Dr. V. H. Ransom

INDUSTRY CONTRACTORS

COPIES	RECIPIENT	DESIGNEE
1	Space Division Aerojet-General Corporation 9200 East Flair Dr. El Monte, California 91734	S. Machlawski
1	Aerospace Corporation 2400 East El Segundo Boulevard P.O. Box 95085 Los Angeles, California 90045	John G. Wilder MS-2293
1	Atlantic Research Corporation Edsall Road and Shirley Highway Alexandria, Virginia 22314	Dr. Ray Friedman
1	Avco Systems Division Wilmington, Massachusetts	Howard B. Winkley
1	Beech Aircraft Corporation Boulder Division Box 631 Boulder, Colorado	J.H. Rodgers
1	Bell Aerosystems Company P.O. Box 1 Buffalo, New York 14240	W.M. Smith
1	Bell Comm 955 L'Enfant Plaza, S.W. Washington, D.C.	H.S. London
1	Bendix Systems Division Bendix Corporation 3300 Plymouth Road Ann Arbor, Michigan 48105	John M. Brueger
1	Boeing Company P.O. Box 3707 Seattle, Washington 98124	J.D. Alexander E.D. Simon
1	Boeing Company 1625 K Street, N.W. Washington, D.C. 20006	Library
1	Boeing Company P.O. Box 1680 Huntsville, Alabama 35801	Ted Snow

INDUSTRY CONTRACTORS

COPIES	RECIPIENT	DESIGNEE
1	Missile Division Chrysler Corporation P.O. Box 2628 Detroit, Michigan 48231	Mr. John Gates
1	Chrysler Corporation Space Division P.O. Box 29200 New Orleans, Louisiana	Mr. Ed Rawls
1	Wright Aeronautical Division Curtiss-Wright Corporation Wood-Ridge, New Jersey 07075	G. Kelley
1	Research Center Fairchild Hiller Corporation Germantown, Maryland	Ralph Hall
1	Republic Aviation Corporation Fairchild Hiller Corporation Farmingdale, Long Island, New York	Library
1	General Dynamics, Convair Division Library & Information Services (128-00) P.O. Box 1128 San Diego, Calif. 92112	Frank Dore
1	Missile and Space Systems Center General Electric Company Valley Forge Space Technology Center P.O. Box 8555 Philadelphia, Pa.	F. Mezger F.E. Schultz J.R. Rausch
1	Grumman Aircraft Engineering Corp. Bethpage, Long Island New York 11714	Joseph Gavin R. Haslet
1	Honeywell, Inc. Aerospace Div. 2600 Ridgway Rd. Minneapolis, Minn.	Mr. Gordon Harms
1	Hughes Aircraft Co. Aerospace Group Centinela and Teale Streets Culver City, Calif. 90230	E.H. Meier V.P. and Div. Mgr. Research & Dev. Div.

INDUSTRY CONTRACTORS

COPIES	RECIPIENT	DESIGNEE
1	Walter Kidde and Company, Inc. Aerospace Operations 567 Main Street Belleville, New Jersey	R.J. Hanville Dir. of Research Eng.
1	Ling-Temco-Vought Corporation P.O. Box 5907 Dallas, Texas 75222	
1	Arthur D. Little, Inc. 20 Acorn Park Cambridge, Massachusetts 02140	Library
1	Lockheed Missiles and Space Co. Attn: Technical Information Center P.O. Box 504 Sunnyvale, California 94088	J. Guill C.F. Ehrlich
1	Lockheed Propulsion Company P.O. Box 111 Redlands, California 92374	H.L. Thackwell
1	Lockheed Missile & Space Company Huntsville Research and Engineering Center P.O. Box 1103 Huntsville, Alabama 35807	Mr. A. W. Ratliff
1	The Marquardt Corporation 16555 Saticoy Street Van Nuys, Calif. 91409	Howard McFarland R.C. Stechman
1	Baltimore Division Martin Marietta Corporation Baltimore, Maryland 21203	Mr. John Calathes (3214)
1	Denver Division Martin Marietta Corporation P.O. Box 179 Denver, Colorado 80201	Dr. Morganthaler A.J. Kullas L.E. Fidler
1	Orlando Division Martin Marietta Corp. Box 5837 Orlando, Florida	J. Ferm

INDUSTRY CONTRACTORS

COPIES	RECIPIENT	DESIGNEE
1	Astropower Laboratory McDonnell-Douglas Aircraft Co. 2121 Paularino Newport Beach, California 92663	Dr. George Moc Director, Research
1	McDonnel-Douglas Aircraft Corp. P.O. Box 516 Municipal Airport St. Louis, Missouri 63166	R.A. Herzmark
1	McDonnell-Douglas Astronautics Co. Bolsa Chica Avenue Huntington Beach, California 92640	R.J. Hoffman
1	Missile and Space Systems Division McDonnell-Douglas Aircraft Company 3000 Ocean Park Boulevard Santa Monica, Calif. 90406	Mr. R.W. Hallet Chief Engineer Adv. Space Tech.
1	Space & Information Systems Div. North American Rockwell 12214 Lakewood Boulevard Downey, California 90241	F.G. Etheridge
1	Rocketdyne (Library 586-306) 6633 Canoga Avenue Canoga Park, Calif. 91304	Dr. R.J. Thompson S.F. Iacobellis J.C. Hyde
1	Northrop Space Laboratories 3401 West Broadway Hawthorne, California 90250	Dr. William Howard
1	Aeronutronic Division Philco Corporation Ford Road Newport Beach, California 92663	D.A. Garrison
1	Astro-Electronics Division Radio Corporation of America Princeton, New Jersey 08540	Y. Brill
1	Rocket Research Corporation York Center Redmond, Washington 98052	Foy McCullough, Jr. T.A. Groudle

INDUSTRY CONTRACTORS

COPIES	RECIPIENT	DESIGNEE
1	Sunstrand Aviation 2421 11th Street Rockford, Illinois 61101	R.W. Reynolds
1	Stanford Research Institute 333 Ravenswood Avenue Menlo Park, California 94025	Dr. Gerald Marksman
1	TRW Systems Group TRW Incorporated One Space Park Redondo Beach, Calif. 90278	G.W. Elverum S.S. Cherry
1	Tapco Division TRW, Incorporated 23555 Euclid Avenue Cleveland, Ohio 44117	P.T. Angell
1	Thiokol Chemical Corporation Huntsville Division Huntsville, Alabama 35807	John Goodloe
1	Research Laboratories United Aircraft Corp. 400 Main St. East Hartford, Conn. 06108	Erle Martin
1	Hamilton Standard Division United Aircraft Corp. Windsor Locks, Conn. 06096	Mr. R. Hatch
1	United Technology Center 587 Methilda Avenue P.O. Box 358 Sunnyvale, California 94088	Dr. David Altman
1	Florida Research and Development Pratt and Whitney Aircraft United Aircraft Corporation P.O. Box 2691 West Palm Beach, Florida 33402	R.J. Coar L.E. Ruby
1	Vickers, Inc. Box 302 Troy, Michigan	

INDUSTRY CONTRACTORS

COPIES	RECIPIENT	DESIGNEE
1	Sandia Corporation P.O. Box 5000 Albuquerque, New Mexico	Dr. J.K. Cole
1	Avco Corporation Avco Space Systems Div. Lowell Industrial Park Lowell, Mass. 01851	Dr. R.L. Reeves
1	Consolidated Engineering Technology Corp. 188 Whisman Road Mountain View, Calif. 94040	Dr. R. Anderson
1	G.V.R. Rao and Associates 14827 Ventura Boulevard Sherman Oaks, Calif. 91403	G.V.R. Rao
1	Lockheed Missiles and Space Co. Huntsville Research and Engineering Center 4800 Bradford Drive Huntsville, Alabama	J.W. Benefield R.J. Prozan
1	Cornell Aeronautical Laboratory, Inc. Buffalo, New York 14221	Dr. J.G. Hall K. Hendershot